Superconducting Nanowire Single-Photon Detectors and Sub-10-nm Lithography

by

Joel K. Yang

Submitted to the Department of Electrical Engineering and Computer Science
in partial fulfillment of the requirements for the degree of

Doctor of Philosophy in Electrical Engineering and Computer Science

at the

MASSACHUSETTS INSTITUTE OF TECHNOLOGY

June 2009

Author ....
Department of Electrical Engineering and Computer Science
April, 2009

Certified by..............
Karl K. Berggren
Associate Professor of Electrical Engineering and Computer Science
Thesis Supervisor

Accepted by...............................
Terry P. Orlando
Chair, Department Committee on Graduate Students

Superconducting Nanowire Single-Photon Detectors and Sub-10-nm Lithography

by

Joel K. Yang

Submitted to the Department of Electrical Engineering and Computer Science
on April, 2009, in partial fulfillment of the
requirements for the degree of
Doctor of Philosophy in Electrical Engineering and Computer Science

Abstract

Superconducting nanowire single-photon detectors (SNSPDs) are useful in applications such as free-space optical communications to achieve high-speed data transfer across vast distances with minimum transmission power. In this and other applications, SNSPDs with high detection efficiencies are required. To this end, we designed and fabricated an integrated optical cavity and anti-reflection coating that enhanced the detection efficiency of SNSPDs by almost threefold to current record values of 57% at 1550 nm wavelength. We also improved our understanding of SNSPDs by modeling the electro-thermal response of the detector. This model showed that, beyond the initial formation of a photon-induced resistance across the nanowire, Joule heating results in the growth of the resistive segment. While simple, this model was useful in designing SNSPDs that reset more quickly, and also in explaining an undesirable behavior of the SNSPDs where the devices latch into a resistive state and fail to reset.

Like many other devices, such as transistors, SNSPDs would benefit from device miniaturization: SNSPDs with narrower nanowires have higher detection efficiencies and increased sensitivity to low-energy photons. In this thesis, we investigated the resolution performance of electron-beam lithography (EBL) by first improving the contrast performance of hydrogen silsesquioxane (HSQ) negative-tone resist. The contrast of HSQ was improved by adding NaCl salt to an aqueous NaOH developer solution. With this improvement, we achieved a high-resolution electron-beam lithography process capable of patterning structures at 9-nm-pitch dimensions. The ability to pattern sub-10-nm structures is useful for fabricating future high-performance SNSPDs, nanoimprint lithography molds, prototypes of next generation transistors and storage media, and templates for controlling the self-assembly of block copolymers (BCPs).

While this EBL process affords high-resolution, it is inherently a low-throughput process due to the serial nature of the pattern exposure. As a result, EBL is not cost effective in fabricating densely-patterned devices in large volumes. However, combining this top-down EBL process with bottom-up BCP self-assembly techniques, we can simultaneously achieve high resolution without sacrificing throughput or pattern registration. We demonstrated that high-throughput fabrication of a hexagonally-ordered array of posts could be achieved by patterning only a sparse array of posts with EBL and using block copolymers to complete the missing structures.

Thesis Supervisor: Karl K. Berggren
Title: Associate Professor of Electrical Engineering and Computer Science

Acknowledgments

I'm fortunate to have had the opportunity to work with so many talented people who have contributed in different ways to this thesis. I am truly indebted to

Professor Karl Berggren, for giving me useful advice, defining clear research directions, and providing many opportunities for collaborations,

Professor Caroline Ross, Professor Rajeev Ram and Dr. Andrew (Jamie) Kerman for kindly agreeing to be on my thesis committee. I would also like to separately thank Caroline for our fruitful collaboration on the templated block-copolymer self-assembly work, Rajeev for teaching me solid-state physics, and Jamie for another fruitful collaboration on the photodetector experiments,

Yeon Sik Jung for teaching me all about block copolymers, patiently doing all the block copolymer processing on the templates I provided, and for his magical ability to make things work,

Dr. Vikas Anant for his insightful simulations on the optical properties of the photodetector, and for his brotherly support throughout my time at MIT,

Bryan Cord for very helpful discussions about lithography and fab processing, and for being a great friend,

Dr. Eric Dauler for sharing his keen intuition and extensive experience in research, which inspired the experimentalist in me,

Professor Edwin Thomas and Dr. Ion Bita for sparking collaborations on the block-copolymer project,

Dr. Joseph Klingfus for help with the Raith 150$^{\text{TWO}}$ electron-beam system,

Professor Kristine Rosfjord, Dr. Debbie Morecroft, for useful discussions and their help in the lab,

Dr. Michael Rooks, and Sung-Wook Nam for helpful discussions on HSQ development, Jim Daley and Mark Mondol for their useful advice and for minimizing delays in my experiments by keeping the lab running,

Sidney Tsai for graciously agreeing to read part of my thesis and providing useful comments,

Tiffany Kuhn for her administrative assistance,

My many colleagues, groupmates, labmates, and suitemates, for making my graduate-school experience a tolerable if not enjoyable one.

I would also like to thank my Dad, whose questioning and ridiculing of my research have prodded me to greater heights, my Mom for her patience and untiring love for the family, and my brother Joshua Yang for helping me find artistic beauty in science.

Finally, this thesis would not have been possible without the constant love and support from my family; my wife Ari who's my emotional anchor, my 3-year-old son Michael for his ebullient personality and good humor, and my unborn son for reminding me of the preciousness and joys of life.

Contents

List of Figures

Chapter 1

Introduction

The chapters in this thesis can be unified under the theme of nanotechnology, i.e. the study of nanoscale devices and fabrication. Nanotechnology deals with structures of the size $\sim 100\,\mathrm{nm}$ or smaller and is interesting due to its potential for creating new, better and/or smaller devices by controlling materials at the nanoscale. Advances in nanotechnology can be seen in the semiconductor industry where efforts are focused on device miniaturization for packing more functionality into microprocessors and more bits into storage media, for example.

This thesis is organized into two parts. Keeping true to the trend of miniaturization in nanotechnology, the dimensions of the devices and structures in this thesis are presented in decreasing order. In the first part of the thesis, we focus on a nanoscale device called superconducting nanowire single photon detectors (SNSPDs) with wire widths of $\sim 90\,\mathrm{nm}$. In the second part, we present fabrication methods to achieve sub-10-nm-pitch dimensions. We will give a brief introduction to each part in the following:

The SNSPD was first demonstrated to work as single photon detectors at $1.55\,\mu\mathrm{m}$ wavelength by Gol'tsman *et. al.* [1, 2]. In this demonstration, it was shown that a superconducting nanowire biased close to its current carrying capacity, i.e. its critical current, was sensitive to single particles of light. Briefly, the SNSPD worked as follows: the energy of a single absorbed photon was sufficient to form, in the superconducting nanowire, a local resistive region [3] which disrupted the flow of current that lead eventually to a measurable voltage pulse.

In comparison with semiconductor-based single-photon-detector technologies, such as avalanche photodiodes (APDs) [4] and photomultiplier tubes (PMTs) [5], superconducting detectors, such as SNSPDs, transition-edge sensors (TES) [6, 7] and kinetic-inductance detectors (KID) [8], have the advantage of sensitivity to low-energy mid-wavelength infrared photons (1 - 3 μm wavelengths). This advantage is due to the smaller bandgap in superconductors (several meV) as compared to the bandgap in semiconductors (several eV). Thus, lower-energy photons can cause inter-band excitations in superconductors. However, this sensitivity to lower-energy photons comes at the price of expensive and bulky cryogenic equipment.

The SNSPD is useful in a number of different applications due also to several of its other chacarteristics. For instance, the SNSPD distinguishes itself as the detector with the lowest timing jitter. With timing jitter of only ~30 ps, the SNSPD can very accurately time the arrival of photons. Furthermore, the SNSPD is one of the fastest detectors and is capable of count rates as high as several hundred MHz. These characteristics make SNSPDs useful applications where timing and speed are important. For instance SNSPDs have been implemented in integrated-circuit testing and diagnostics for detecting and timing infrared photons emitted by switching transistors [9, 10, 11]. Other examples where SNSPDs have been implemented are in quantum-optics research experiments such as quantum cryptography [12, 13] and intensity correlation measurements [14]. Finally, SNSPDs are also promising for use in ultra-long range optical communications [15, 16] at 1.55 μm wavelength due to their high-speed and low jitter performance.

The early days in the SNSPD field lacked a robust fabrication process with good device yield. The early fabrication process [1, 17] involved a metal lift-off process to define an etch mask for the nanowires and a subsequent wet-etch process to remove the metal after pattern transfer. While this process worked, it was not robust as it required an unreliable lift-off process, which also introduced unnecessary line-edge roughness in features, and a wet etch process, which may have caused damage to the underlying superconducting material. Instead, we developed a fabrication process [18,

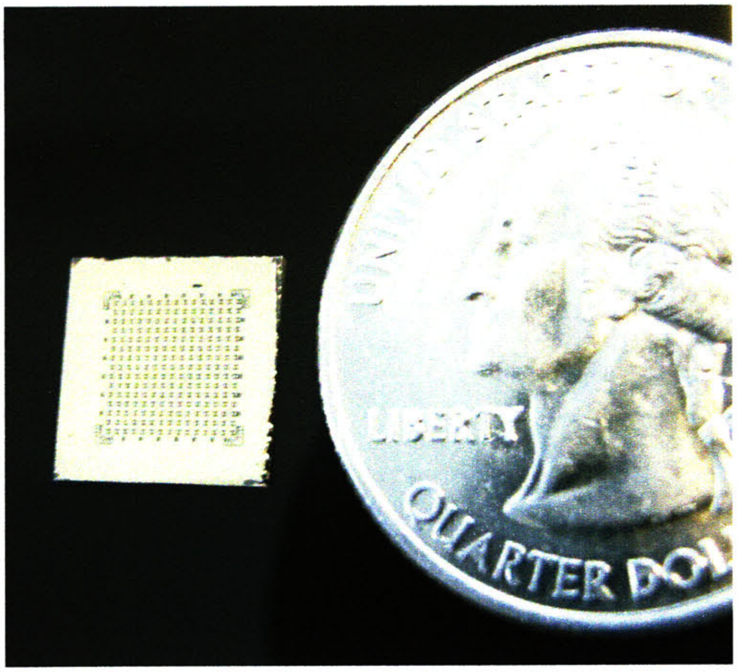

Figure 1-1: Photograph of a completed SNSPD chip that contains 250 devices in a size comparison with a United States quarter. The chip was covered mostly in gold which was used as electrical contacts to the devices.

19] that used electron-beam lithography (EBL) exposure of a negative-tone resist hydrogen silsesquioxane (HSQ) followed by pattern transfer into a superconducting NbN film. This process enabled the fabrication of smoother and more uniform-width nanowires (by using electron-beam proximity effect correction) and avoided the lift-off process. Furthermore, we did not need to remove the HSQ etch mask after pattern transfer as HSQ was a dielectric material that would not electrically short out the underlying superconducting material. Our fabrication strategy was to make hundreds of devices on a single chip, which allowed us to assess the yield of our process and to also systematically investigate and improve the performance of SNSPDs. An example of a completed chip is shown in Fig. 1-1. As this fabrication process has already been discussed in my S.M. Thesis, we will only provide an update on the process flow here in Appendix A.

The first part of the current thesis will instead focus on addressing (1) the poor detection efficiency, and (2) the lack of a device model for the SNSPD. Compared to other superconducting single-photon detectors such as the transition-edge sensor

(TES), which were also sensitive to near-infrared-wavelength photons but had detection efficiencies greater than 90 %, the detection efficiency of SNSPDs at 17 % [20] was unacceptably low. Furthermore, the lack of a device model meant that we did not have a clear understanding of the SNSPD device operation, which was prerequisite for designing better SNSPDs. Addressing both problems would widen the adoption of SNSPDs in more applications.

Our work on improving the detection efficiency of SNSPDs is presented in Chapter 2. The central result in this part is the design and fabrication of an optical cavity that enhanced the detection efficiency of SNSPDs from a previous value of 17 % to a current record value of 57 % at 1550 nm wavelength [21][1]. This fabrication process for enhancing the detection efficiency is also used in multi-element SNSPDs [22] which are being pursued as the primary receiver for the Lunar Laser Commnucation Demonstration program at MIT Lincoln Laboratory. In Chapter 3 we provide an electro-thermal model of the detector, which was useful in clarifying doubts in the field that thermal effects played an important role in the operation of SNSPDs. This model also predicted a new detector behavior where the detector fails to reset into the superconducting state after detecting a photon and, instead, stays latched in a self-sustained resistive state. The model also provided insights into ways to avoid this problem.

While the typical SNSPD has nanowire widths of 90 nm, some experiments on SNSPDs with narrower 50-nm-wide wires [23] showed an increase in detection efficiency for a given photon wavelength, and also the potential for increasing the SNSPD sensitivity at longer 10 μm wavelength photons. This improvement in detector performance led us to investigate the resolution limit of our EBL patterning tool and other high-resolution fabrication methods, which we discuss the second part of the thesis.

In this second part of the thesis, we focus on high-resolution lithography and showcase some of the highest-resolution structures made by resist-based EBL. The main enabling result in this part is the contrast enhancement of HSQ which drastically

---

[1] To date, detection efficiencies as high as 70 % has also been measured though not yet published.

improved its resolution. By adding salt into an aqueous base developer, we were able to convert HSQ from a notoriously low-contrast resist to one with sufficiently high contrast. With this new development process, resolution as high as 4.5-nm-half-pitch can be achieved. This work is presented in Chapter 4.

Although the resolution achieved by EBL is extremely good, using EBL to pattern dense and high-resolution structures over large areas proves to be a slow and expensive process. Therefore, EBL on its own cannot be used to replace optical projection lithography as the next generation lithography tool. Other modifications have to be made to increase the speed and throughput of EBLs for it to become economical for large-volume manufacturing purposes. Examples of such modifications are in the use of multiple-beam EBL [24] and high-sensitivity resists [25]. In Chapter 5, we instead present an alternative approach where we use sparse structures made by EBL to guide the molecular self-assembly of block copolymers. In this approach, throughput is improved as the EBL only exposes a fraction of the pattern area and block copolymers are used to fill in the missing structures.

Block copolymers (BCPs) are fascinating polymer molecules that can self-assemble into nanostuctures with feature dimensions that are smaller (typically less than 20 nm half pitch) than can be achieved by current optical lithography. This self-assembling or self-organizing nature of BCPs is a powerful means to fabricate structures in a scalable and economical fashion. Interestingly, self-organization is also the means by which biological systems develop and grow.

BCP polymer molecules consist of two or more chemically distinct polymer chains (or blocks) that are covalently bonded at their ends. Due to the tendency of each polymer type to stay together (but being inhibited by the covalent bonds), BCPs will micro-phase separate (instead of macro-phase separate) when annealed. For instance, due to this phenomenon of micro-phase separation, a thin film of BCP can self-assemble into spheres or lines on a surface, depending on the composition of the individual molecules.

One of the main challenges in using BCPs in lithography are their lack of long-range order and registration to a common frame of reference. As a result, although the resulting nanostructures appear periodic in the short range, they are randomly oriented in the long range. Previous efforts to order thin films of BCPs have used a range of different techniques to achieve ordering. Such techniques include the application of an external electric [26] or thermal fields [27], the use of lithographically defined steps or trenches [28, 29], and chemically functionalized surfaces [30]. Of these methods, true long range order and registration on the 2D substrate surface was achieved only in the case of chemically functionalized surfaces. However, this approach lacks any improvement in throughput as the patterns on the substrate were patterned by EBL at the same density as the resultant BCP structures.

Our approach addresses the problem of registration by utilizing a 2D array of well-registered posts and does so at a higher throughput by exposing only a fraction of the final structure with EBL and using the much more economical BCP processing to form the missing structures. Furthermore, the lithographically defined posts substituted individual BCP microdomains and did not take up precious substrate area. Hence, this nanostructured template allowed for a truly dense array of nanostructures that completely covered the substrate surface. The ability to form densely packed, well-ordered dot structures economically has major implications in the patterning of high-density magnetic storage media.

Part I

Superconducting Nanowire Single-Photon Detectors

Chapter 2

Increasing the detection efficiency of superconducting nanowire single-photon detectors (SNSPDs)

In our previous work [18, 19], we described the process for fabricating superconducting nanowire single-photon detectors. This previous work focused on developing a fabrication process that (1) ensures uniform nanowire width with minimal line-edge roughness, and (2) does not damage the NbN superconducting material. The fabrication process involved electron-beam lithography (EBL) exposure of hydrogen silsesquioxane (HSQ) resist. Extending on this fabrication process, we describe in this chapter our work on enhancing the detection efficiency of SNSPDs by adding an integrated optical cavity and an anti-reflection coating (ARC). Most of the work presented in this chapter has been published in Optics Express [21].

Increasing the detection efficiency of SNSPDs was necessary as it was too low for SNSPDs to be competitive with other types of single photon detectors. For instance, other admittedly slower detectors such as transition-edge sensors [6], with detection efficiencies $> 95\,\%$, would outperform SNSPDs with detection efficiencies of only $17\,\%$. Hence, although SNSPDs excel in applications that require high speed, low jitter and low dark-count rates, they were not suitable where high detection efficiency was also an advantage. Examples of such applications are quantum cryptography [12], integrated-circuit testing [9, 10], and ultra-long range optical communications [15].

The addition of an optical cavity and ARC on the detectors increased the detection efficiency of the SNSPD by increasing the probability of photon absorption at the detector. Because a photon has to be absorbed for it to be detected, making the detector more efficient at absorbing photons directly increased its detection efficiency.

In addition to enhancing the detection efficiency of SNSPDs, we also systematically tested over 132 devices before and after the addition of the cavity and ARC. By testing a large number of devices on a single chip, we obtained information of the device yield. We saw that the best device demonstrated detection efficiencies of 57 % at 1550-nm wavelength and 67 % at 1064 nm with the added cavity and ARC. This was the highest reported detection efficiency for SNSPDs and was a factor of ~ 2.7 improvement over devices without the cavity and ARC. In addition to this peak detection efficiency, a median detection efficiency for the 132 measured devices was 47.7 % at 1550 nm.

2.1 Introduction

Increasing the detection efficiency (DE) of SNSPDs is a key factor in enabling the adoption of SNSPDs as the single-photon-detector of choice for future high-performance single-photon optical systems. Past work on SNSPDs have demonstrated impressive detector performances, such as sub-50-ps jitter [31], sub-5-ns reset times [16, 32], and near-zero dark-count rates [33]. However, the detection efficiency of SNSPDs was poor with the best performance of only 17 % at 1550-nm wavelength [20]. This detection efficiency performance is no better than those of other (admittedly slower and higher-jitter) detectors such as InGaAs geiger-mode APDs (20 % DE) [4] and transition-edge sensors ($> 95\,\%$ DE) [6].

Before we explain the cause of this low detection efficiency, we will first describe the physical structure of the SNSPD for clarity. Figure 2-1 shows side- and top-view schematics of the SNSPD. The nanowire bridges two Au contact pads that connect the device electrically to the outside world. A top-view SEM of the device is shown in

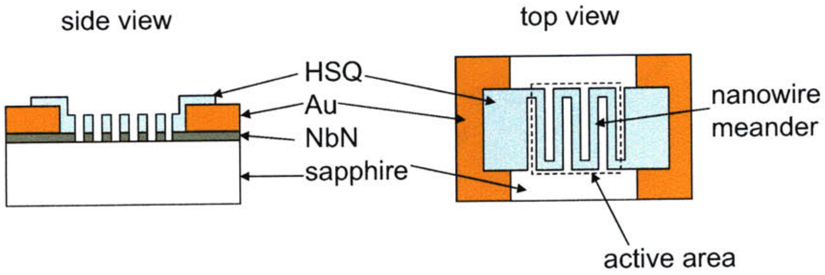

Figure 2-1: Schematic showing the side and top view of the NbN nanowire single-photon detector before adding an optical cavity and anti-reflection coating. The active area of the detector is shown in the top view schematic as the area enclosed by the dashed line. Instead of having just a single straight nanowire, the nanowire was patterned into a meander (boustrophedonic) structure within this active area to increase the coupling of light into the detector. HSQ was used as an EBL resist and etch mask for pattern transfer into NbN and was left on the detector after device fabrication.

Fig. 2-2. The device consists of a 4-nm-thick NbN film that has been patterned into a meander structure consisting of 90-nm-wide nanowires on a 200-nm pitch. Having the nanowire wound in a tight meander pattern maximized its area of overlap with the optical beam.

SNSPDs had poor detection efficiency primarily due to optical loss. This loss occurred as most of the incident photons are either reflected from or transmitted through the 4-nm-thick device plane. Thus, only a small fraction of incident photons are absorbed in the device. Since photons need to be first absorbed before they are detected, this low absorptance results in low detection efficiency.

The device detection efficiency DE of the SNSPD can be defined as a product of the probability of photon absorption P_a, and the probability of a resistive state formation across the nanowire (after a photon has been absorbed) P_r, i.e. $DE = P_\mathrm{a}P_\mathrm{r}$. This definition clearly breaks the photodetection event into two separate processes, i.e. photon absorption and the generation of an electrical signal. Hence, of the number of incident photons on the detector active area, a fraction P_a is absorbed, and of the number of absorbed photons, a fraction P_r results in an electrical signal.

With the definition given above, one can increase DE either by increasing P_a and P_r. If we only consider photons that are incident on the active area of the detector, then P_a is the absorptance of the patterned NbN film. We can increase

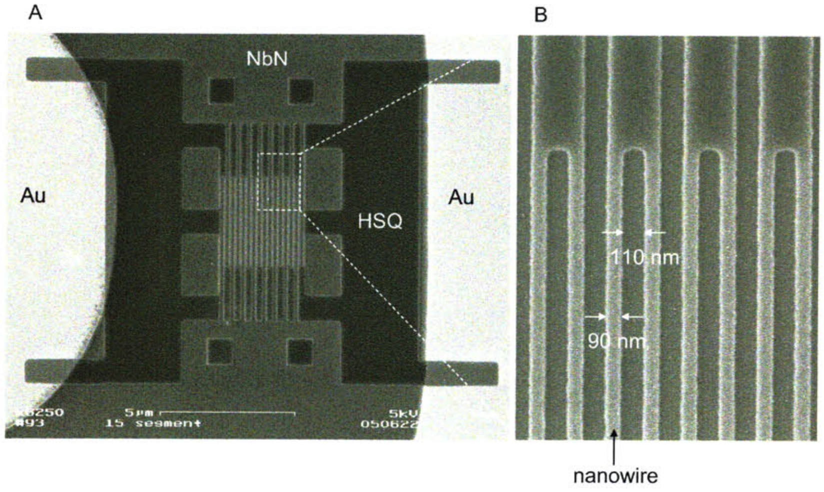

Figure 2-2: (A) Top view scanning-electron micrograph SEM of the device prior to pattern transfer into the underlying NbN. Imaging was done before pattern transfer as the unetched NbN provided a conductive layer to prevent sample charging during inspection. (B) SEM showing a larger view of a portion of the nanowire meander consisting of 90-nm-wide meanders on a 200-nm pitch.

this absorptance by minimizing photon loss due to reflection from and transmission through the device, i.e. by adding the integrated optical cavity and ARC. On the other hand, P_{r} can be increased by biasing the wire close to its critical current [23, 19], or reducing the nanowire width [23].

The approach we took for increasing the detection efficiency of the SNSPDs was to increase the photon absorptance of the detector which increased P_{a}. This increase in absorptance was achieved by placing a mirror spaced at an optimal distance behind the plane of the detector, and adding an anti-reflection coating (ARC) for the sapphire substrate, resulting in a final device structure as shown in Fig. 2-3. The mirror reflected the transmitted photons back to the detector and increased the probability for photon absorption. Furthermore, the mirror, when placed at an optimal distance from the detector plane, reduced reflection from the detector by destructive interference of electromagnetic waves reflected off the mirror and detector planes. The combination of the mirror, spacer and detector plane formed an optical cavity. The ARC, in addition to this optical cavity, reduced the reflection of light off the sapphire substrate and further increased the absorption of photons in the detector. The design

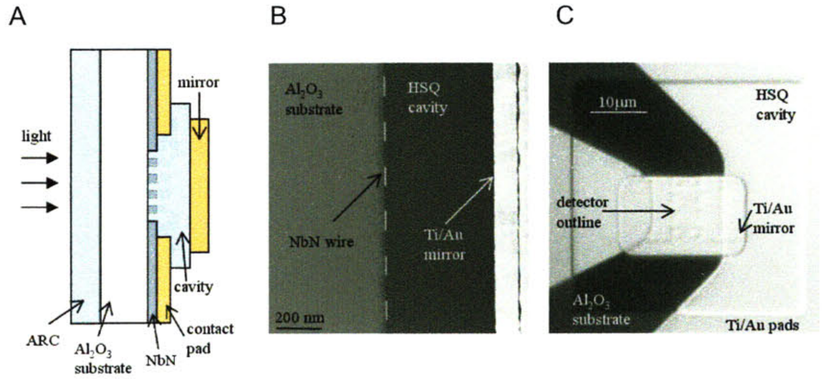

Figure 2-3: (A) Schematic cross-section of photodetector (not to scale) integrated with an optical cavity and anti-reflection coating (ARC) to reduce loss of photons from reflection and transmission. The device was illuminated from the back of the chip through the ARC and sapphire substrate. Photons that were not absorbed in the NbN wire at first pass entered the optical cavity, thereby having many chances to get absorbed by the NbN. The cavity thickness was chosen so that destructive interference reduced the reflectance from the NbN surface. (B) Transmission electron micrograph of cross-section of fabricated device with optical cavity. The cavity shown here was fabricated for calibration purposes and was thicker than those used to increase the detection efficiency. (C) Optical micrograph showing top-down view of optical cavity on photodetector. The outline of the detector is visible underneath the Ti/Au mirror due to a 9-nm-high step where the mirror goes from the substrate to the detector.

of the cavity and ARC and their fabrication is described in section 2.2.

Previous work on increasing the detection efficiency of SNSPDs was done using an optical cavity without an ARC [34]. In this past work, characterization was done only on a single detector that had a low detection efficiency which increased to $\sim 1\,\%$ after adding the cavity. Unlike this previous work, we characterized the detection efficiency of 132 devices before and after the integration of both the cavity and the ARC, and measured detection efficiencies as high as 57 % at 1550 nm wavelength. The experimental setup for testing and measuring the *DE* of these devices will be discussed in section 2.3

2.2 Cavity and ARC design and fabrication

In this section, we will describe the choice of materials, calculations, and fabrication process for the optical cavity and ARC. The final result of this effort is shown schematically in Fig. 2-3A. Here, we show a schematic cross-section of the device designed to optimize photon absorption in the NbN nanowire. Photons are incident onto the ARC, propagate through the sapphire substrate, and reach the niobium nitride (NbN) layer where they are either reflected, absorbed, or transmitted. The NbN/hydrogen silsesquioxane (HSQ)/mirror structure forms a cavity, which is engineered so that the light reflected from the mirror interferes destructively with the reflection from the NbN/sapphire interface.

2.2.1 Cavity and ARC design

Here we describe the choice of materials for the cavity and ARC, and the calculations of the optimal cavity dielectric and ARC thicknesses.

The dielectric material used in the cavity and ARC was hydrogen silsesquioxane HSQ formulated as FOx-14 from Dow Corning. We chose HSQ as the cavity dielectric material for four reasons: (1) HSQ is a spin-on-glass and thus easy to deposit; (2) at infrared wavelengths the optical absorptance in HSQ is negligible [14]; (3) incorporating HSQ allowed us to simplify the cavity fabrication as we did not have to remove the remaining layer of HSQ from the previous process; and (4) HSQ was already used in the detector fabrication process, therefore, we knew it could not damage the device.

HSQ was also a suitable material for the ARC as it has an index value that is close to the optimum index for matching vaccum and sapphire. For perfect index matching between sapphire, which has an index $n_{\text{sapp}} = 1.77$, and vacuum with index $n_{\text{vac}} = 1$, we needed a material with index $n_{\text{ARC}} = \sqrt{n_{\text{sapphire}} n_{\text{vac}}} = 1.33$ and thickness of $\lambda/4n_{\text{ARC}}$. HSQ was a suitable material for the ARC due to its low index of refraction of 1.4 at 1550 nm wavelength which was close enough to the ideal index value 0f 1.33. For light at 1550 nm wavelength, 277 nm of HSQ was required for a $\lambda/4$ ARC. We calculated that this ARC made of HSQ would reduce reflection off the front surface of sapphire from 7.7 % to 0.26 %.

In our calculations, we solved electromagnetic wave propagation through a multilayered media of the detector consisting of the materials HSQ/sapphire/NbN/HSQ/Au. For simplicity we assumed an incident propagating plane wave of 1.55 μm wave-

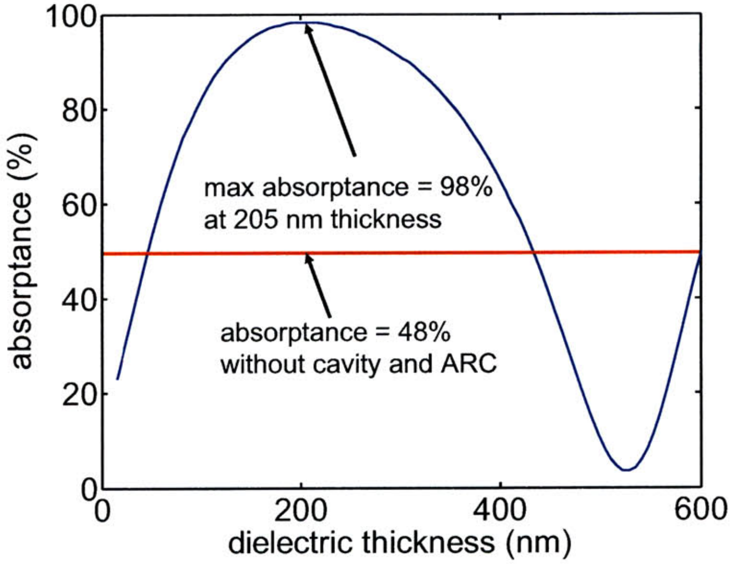

Figure 2-4: Plot of percentage absorptance as a function of HSQ dielectric thickness. This calculation was done for an unpatterned NbN film of 4 nm thickness and HSQ ARC of 277 nm thickness. The gold mirror thickness was 120 nm. The maximum absorptance of 98 % can be achieved at a HSQ dielectric thickness of 205 nm.

length in this calculation. We used the following indices of refraction for the materials:

1. $n_{\text{HSQ}} = 1.4$
2. $n_{\text{sapphire}} = 1.77$
3. $n_{\text{NbN}} = 7.1 - 5.1i$
4. $n_{\text{Au}} = 0.559 - 9.81i$

This index of refraction for NbN was measured by E.A. Dauler at Lincoln Laboratory. In more recent measurement by J.A. Woolam Inc. the NbN index value was found to be $n_{\text{NbN}} = 5.23 - 5.82i$ [35]. This new index was more accurate and agrees well with experimental results [35]. However, the cavity described in this chapter was designed based on the older index value.

Figure 2-4 show the calculation results for a multi-layer stack consisting of HSQ/sapphire/NbN/HSQ/Au. The calculation shows that the optimal cavity thickness was 205 nm, which resulted in a maximum absorptance for an unpatterned NbN film of 98 %. In contrast, the absorptance for an unpatterned NbN film without ARC

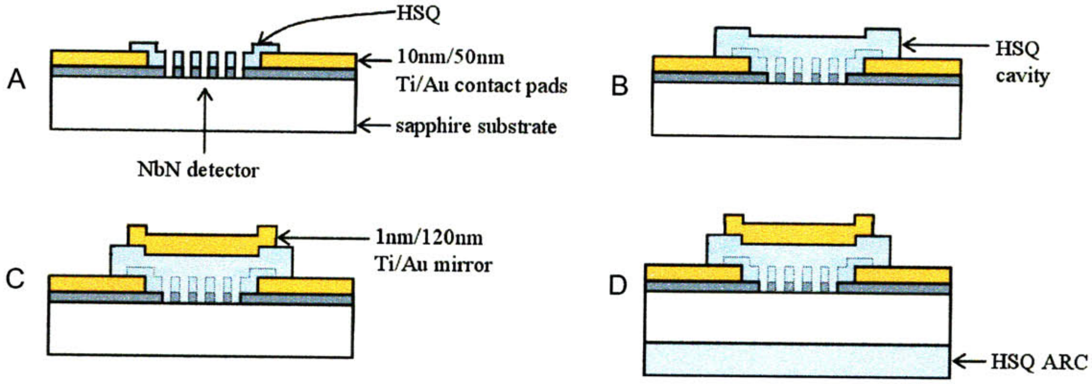

Figure 2-5: Process flow for integration of optical cavity and anti-reflection coating (ARC) onto photodetector. (A) The process began with a fabricated photodetector [19]. Note the residual HSQ etch mask left on the NbN wires from the photodetector fabrication process. (B) HSQ was spin-coated to achieve an optical cavity thickness of 195 nm and then electron-beam patterned. (C) 1 nm of Ti and 120 nm of Au were evaporated onto patterned photoresist followed by lift-off, leaving the mirror for the optical cavity. (D) Finally, 277 nm of HSQ was spin-coated on the back side of the wafer and hardened in an O2 plasma to form the ARC.

or optical cavity was 48 %. Hence an increase in absorptance by a factor of ~2.1 could be expected by the addition of the ARC and cavity based on this simple calculation.

A more elaborate calculation for NbN films patterned into gratings of different fill factors has been done by Vikas Anant [35] using numerical methods. This calculation showed that the maximum absorptance for a NbN film patterned into a 50 % fill-factor grating was 68 %. With this numerical calculation, the expected enhancement factor from the addition of the cavity was also ~2.1, which agreed with our simple calculation above.

2.2.2 Cavity and ARC fabrication

The process flow for fabricating an optical cavity on top of the detector is shown in Fig. 2-5. A recipe for fabricating the cavity is detailed in Appendix A. The process began with a fabricated photodetector [19] composed of a tightly wound meander structure with a 90-nm-wide wire and 210-nm spaces. This detector had an active area of 3.3 μm × 3.0 μm as shown in Fig. 2-2. First, HSQ was spin-coated on to the front of the detector and patterned to form the dielectric material of the cavity. Then titanium and gold were added to create a mirror for the optical cavity. Finally, HSQ was spin-coated onto the back of the device to act as an ARC. In this subsection, we detail this fabrication process.

Figure 2-5B shows the device with the cavity dielectric. First, the thickness of the HSQ remaining from the detector fabrication process was measured using atomic-force microscopy (AFM) and determined to be 45 nm. We then spin-coated HSQ onto the sample at 8.6 krpm resulting in a total dielectric thickness of 195 nm on top of the detector active area[1].

The samples were then soft-baked at 90°C for 5 min to drive excess solvents out of the HSQ. Next, a layer of a conductive polymer (aquaSAVE by Mitsubishi Rayon America Inc.) was spin-coated onto the sample at 3.5 krpm to minimize charging during the subsequent electron-beam exposure. We used electron-beam lithography with 10 kV acceleration voltage and 600 $\mu C/cm^2$ exposure dose to expose the resist in a 40×40 μm^2 area centered at the detector. The sample was developed in 0.26 N tetramethyl ammonium hydroxide TMAH for 8 min to remove unexposed HSQ. AFM imaging of the dielectric surface before mirror deposition revealed a peak-to-peak surface roughness of only 1 nm over the active area of the detector despite the underlying topography.

Figure 2-5C shows the device after the addition of the cavity mirror. A metal liftoff process was used to deposit this mirror. This liftoff process was similar to the one used for depositing gold contact pads in the detector fabrication [19] except that 1 nm of Ti, rather than 10 nm of Ti, was deposited to promote adhesion of the reflector to the dielectric. The Ti thickness was minimized to optimize cavity performance: at IR wavelengths, gold has a greater perpendicular reflectivity than titanium [36]. Calculations revealed that the thin layer of titanium reduced the absorptance of the cavity by less than 0.1 % relative to a gold-only mirror that was 120 nm thick. The

---

[1] The original HSQ thickness target, chosen based on preliminary simulations of the cavity's optical properties as mentioned in the previous subsection, was 205 nm. Repeatable, systematic variation caused by spin-coating over micron-scale topography led to a 10-nm reduction in the local thickness over the active area of the detector (determined by AFM inspection of the HSQ crosssection over the detector area). If desired, future experiments could pre-compensate for this bias by targeting a thicker HSQ layer. Such a correction was unnecessary in our case because of the insensitivity of the cavity to small inaccuracies in dielectric thickness.

resultant mirror size was 14 μm×22 μm.

A transmission electron micrograph of the cross section of an optical cavity on top of a device is shown in Fig. 2-3B. An optical micrograph of the completed cavity structure is shown in Fig. 2-3. We used a single-layer ARC on the bottom surface of the sample to reduce optical loss due to reflections at the vacuum-sapphire interface. Figure 2-5D shows the devices after the addition of an ARC. The ARC was applied to the back of the device by mounting the sample top-side down onto a silicon handle wafer with two drops of Shipley S1813 photoresist. The handle-wafer-and-sample pair were then soft-baked at 90°C for 15 min. This mounting method prevented physical damage to the devices on the top surface of the chip during the addition of the ARC. Then, 277 nm of FOx-14 was added to the pair by spin-coating at 2.8 krpm and then baking for 20 min at 90°C. Next, the HSQ ARC was oxygen plasma treated for 10 min to form a hardened surface using a Technics PlanarEtch II oxygen asher. The plasma treatment conditions were 100 W power and 2.8 kPa pressure of 80 % He/ 20 % O_2. Lastly, the sample was released from the handle wafer with a 2-min acetone soak, leaving a robust ARC.

2.3 Detection efficiency measurements

As we were measuring the detection efficiency of a large number of devices over several experimental runs, we needed our measurements to be accurate and reproducible. In the following subsections, we will describe how the detection efficiency of SNSPDs was accurately measured. We also explain the care taken in measuring the laser beam power, spot size and polarization to minimize run-to-run variations.

The detection efficiency measurements were done at Lincoln Laboratory using a cryogenic probing station by Lakeshore Cryotronics, Inc. which allowed us to test multiple devices on a chip in a single cool-down. The ability to do so allowed us to obtain statistical information of the device yield and performance. This testing strategy was an improvement over previous approaches [37, 38] where each device that was fabricated separately on individual chips was tested one at a time either in

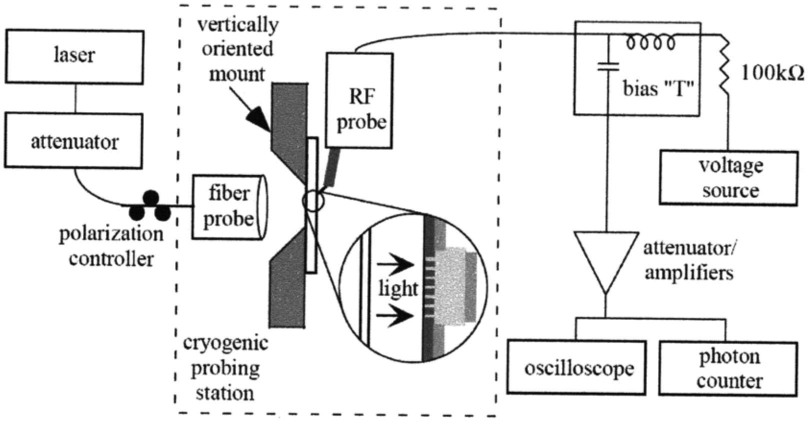

Figure 2-6: Schematic of the experimental setup with the optical components on the left connected by optical fiber and the electrical components on the right connected by coaxial cable. The fiber probe illuminated the sample through the back side of the sapphire substrate while the RF probe contacted the gold contact pads on top of the NbN.

a liquid Helium dewar or in a cryostat.

2.3.1 Experimental setup

The setup used to measure the electrical and optical response of the photon-counting devices is shown in Fig. 2-6. This setup included three major subsystems: (1) the cryogenic probing station; (2) the room-temperature electronics; and (3) the pulsed optical source. In this subsection, we describe each of these subsystems.

First the sample was placed in the cryogenic probing station. Our sample consisted of an 8-mm-square chip, containing 154 individual devices. The cold head of the probing station was cooled to as low as 1.8 K. The sample was attached using silver paint to a gold-plated copper sample mount that allowed optical access to the devices through the back of the substrate and electrical access from the front.

Electrical contact with the devices was established using a 65-GHz RF probe connected to a coaxial cable and mounted on a micromanipulator arm, so that it could be touched down to any individual device on the sample. The probe was cooled to < 30 K using copper braids connected to the 4.2 K stage of the probing station.

An optical fiber and lens assembly was mounted to a second cooled micromanipulator, whose position was controlled using an automated, closed-loop three-axis positioning stage with submicron resolution (MICOS GmbH). This stage allowed the optical spot produced by the lens to be aligned automatically with any device using that device's photon count rate as feedback.

Our room-temperature readout-electronics subsystem was connected to the cold RF probe through coaxial cable and a vacuum feedthrough. First, a 0.5 m length of coaxial cable was used to provide a delay that temporally separated any spurious electrical reflections from the output pulses of our devices. This cable was connected to a bias tee. Current bias was supplied to the devices through the DC port of the bias tee using a battery-powered voltage source in series with a 100 kΩ resistor. The AC port of the bias tee was connected to two cascaded wideband, low-noise amplifiers (MITEQ JS2-00100400-10-10A, 27 dB gain, 0.1-4 GHz) through a 3 dB attenuator.

Without the isolation provided by this attenuator, we observed that the critical currents of our devices were suppressed by up to 10 %; this was likely the result of electrical noise associated with reflections at the amplifier input (VSWR 2:1). The amplifier output was sent through a DC block and split using a resistive splitter to be sent into both a photon counter and a 6-GHz, real-time oscilloscope. Without the DC block on the outer conductor, we again observed that the critical currents of our devices were suppressed, this time by up to 20 %, likely due to ground noise.

For the detection-efficiency measurements, the photon counter was used to count the number of electrical output pulses resulting from a fixed number of highly attenuated (< 0.25 incident photons per pulse) optical pulses. The signal-to-noise ratio of the amplified voltage pulses was sufficiently high that the discriminator threshold level at the input of the counter could be varied over a wide range without changing the observed count rate. In order to reject counts not directly associated with the optical excitation, the counter was operated in a gated mode in which only those pulses arriving within a fixed 5-ns-long window were counted. This window was centered on the arrival time of detection events generated by the optical pulses by triggering the gate synchronously with the laser's output pulses, and then adjusting the gate delay. In addition, a dark-count-noise baseline was taken of counts recorded in the gate window with the light blocked mechanically. This baseline was subtracted from each measurement. Within the optical subsystem, the devices were illuminated with light from a laser that generated pulses at a 10 MHz repetition rate. This light was attenuated to the single-photon level using a precision optical attenuator and calibrated using an InGaAs power meter at power levels 30 dB above its noise floor.

Varying the polarization of the light using a fiber polarization controller resulted in a change in the count rate. The polarization was set to maximize the count rate for all detection-efficiency measurements. All of the optical components were fiber-coupled and the measured losses were stable to less than 0.05 dB. The loss between the fiber connector at the input to the probing station and the output of the lens assembly was separately measured (at room temperature) using a free-space InGaAs power meter at a power level of 100 μW.

Finally, the size of the optical spot was measured. Since the position of the lens could change as the probe is cooled, this spot size had to be measured *in situ*, at low temperature. To do this, we translated the optical probe while measuring the device count rate and mapped out the resulting profile, which consists of the convolution of the Gaussian beam profile and the rectangular active area of the detector. By fitting the measured profiles, the Gaussian beam waist could be extracted, and from this, the fraction of the total power incident on the device's active area was determined. Detection efficiencies were measured using several spot sizes ranging from 20 μm to 90 μm, yielding consistent results.

2.3.2 Measurement results

Here we present the results of measurements of 132 of these devices from one of these chips where measurements were made three times on each device: once after the initial device fabrication, once after the optical cavity was added, and finally after the ARC was added. This procedure enabled us to determine the detection efficiency of devices as well as the enhancement due to the cavity and ARC.

These measurements were made at 1550-nm wavelength and a temperature of 1.8K. Additionally, measurements were also made at 1064 nm and 4.2K. Lastly, the

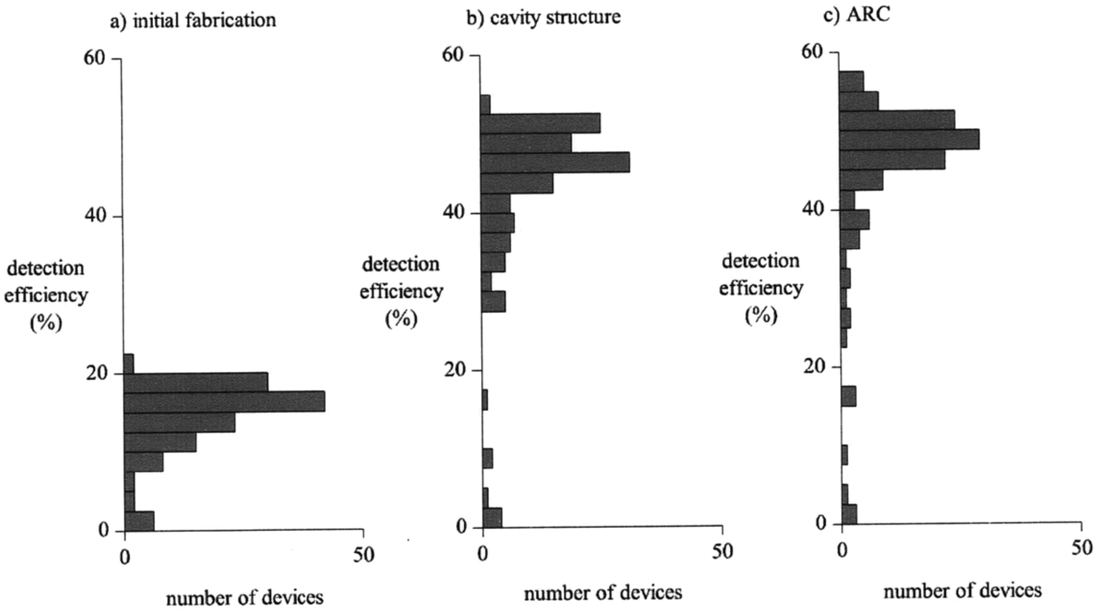

Figure 2-7: Histogram of detection efficiencies for 132 tested devices on a chip measured (a) after initial fabrication of the bare photodetectors, (b) after addition of the cavity structure and mirror on the devices, and (c) after an anti-reflection coating was added to the back side of the sapphire substrate. Each measurement was made at 1.8K and at $I_{\text{bias}} = 0.975\,I_{\text{c}}$.

timing jitter of the devices was also determined. The results of detection-efficiency measurements made at 1550-nm wavelength are shown in Fig. 2-7. These histograms show the distribution of detection efficiencies measured for each device at 97.5 % of its critical current. As shown in Fig. 2-7C, the highest detection efficiency observed was 57 %. After the integration of both an optical cavity and ARC, fewer than 10 of the 132 devices had a detection efficiency below 20 %; the median and mean detection efficiencies were 47.7 % and 44.3 %, respectively. This yield is clearly sufficient to fabricate large numbers of high-efficiency devices and even small ($\sim$4-element) arrays of these devices.

The enhancement due to the addition of a cavity and an ARC was determined with a subset of the total devices tested at 1550 nm. Measurements taken over three days with the same sample under vacuum but cycled (three times) up to room temperature showed virtually no changes in the critical currents (<2 %) or detection efficiencies (<4 %). However, larger changes were observed for some devices over longer time scales (months) and in between processing steps.

In nearly all cases, a strong correlation was observed between changes in critical current and changes in detection efficiency; to distinguish the impact of the added optical elements from any changes in the detection efficiency that were correlated to changes in the critical current, we quantified the effect of adding the resonator and AR coating using only the subset of devices whose critical currents were nearly unchanged between processing steps.

For the addition of the cavity, we obtained an enhancement factor of 2.44±0.005, based on the 21 devices whose I_c changed less than 3 %, and whose initial DE was greater than 13 %. The addition of the ARC provided an additional enhancement factor of 1.050±0.009, based on the 105 devices whose I_c changed less than 3 % in this step of the processing.

To determine the detection efficiency at 1064-nm-wavelength, the five devices with the highest measured detection efficiency at 1550 nm were tested after the addition of the optical cavity and ARC. The highest detection efficiency observed was 67 %. This result demonstrates the utility of our devices at another technologically important wavelength.

The detection efficiencies reported were measured at an operating temperature of 1.8K. Increasing this temperature resulted in a slight degradation of device performance. Specifically, at the easily accessible temperature of 4.2 K the highest observed detection efficiency was 30 % at 1550-nm wavelength and 57 % at 1064-nm wavelength.

Lastly, to verify that previously reported excellent jitter performance [31] for these devices was unaffected by the cavity, the timing jitter of the electrical pulses relative to the optical excitation was determined. This experiment was carried out using 1-ps-wide pulses from a passively mode-locked 1550-nm source by measuring the time interval between optical excitation and electrical pulse response, using the scope to trigger on the sharp leading pulse edge at a fixed voltage threshold, for a large number of pulses and producing a histogram distribution. This distribution was measured to be 41 ps full-width at half maximum FWHM for a device with an optical cavity at 1.8 K. This result suggests that, as expected, the timing jitter of these devices was not degraded by the addition of a very short, low-Q resonant optical structure.

2.4 Conclusion and future work

This chapter reports a 57 % detection efficiency of superconducting nanowire single-photon detector at 1550-nm wavelength and a 67 % detection efficiency at 1064-nm wavelength through the integration of an optical cavity and ARC. In addition to this peak detection efficiency, we have found a median detection efficiency at 1550 nm of 47.7 % over greater than 130 devices.

We note that observed results may be further improved by increasing the thickness of the NbN film while decreasing the width of the nanowires or by increasing the fill-factor of the devices. We have done some recent work on increasing the fill-factor of the devices. In this work, we fabricated devices with fill-factors as high as 88 % while maintaining the nanowire width at 90 nm. Although higher fill-factor devices exhibited higher detection efficiencies compared to lower fill-factor devices when measured at the same bias current, the high fill-factor devices had substantially suppressed critical currents. Future work will focus on understanding the cause of this suppression.

Detection efficiency can also be increased by further optimization of the optical elements of the detector by more accurately controlling the thickness of the cavity dielectric or by increasing the quality-factor of the cavity. We plan to pursue future work along these lines.

Chapter 3

Electro-thermal model of Superconducting Nanowire Single-photon Detectors (SNSPD)

The modeling of SNSPDs requires an understanding of their optical, electrical and thermal properties. In the previous chapter, we showed that by modeling the SNSPD optically as a multi-layered media, we were able to design an optical cavity to enhance the absorptance of light at the detector. However, as the detector is essentially a transducer that converts the absorbed photon into electrical signals, modeling all the processes that occur, from the instance when the photon is absorbed to when a voltage pulse appears across the nanowire, will help us understand how the device works and how we can improve its performance. The modeling of these processes requires us to consider both its electrical and thermal properties.

3.1 Introduction

In this chapter, we report on the first attempts at understanding and modeling the response of the SNSPD as a system, which consists of the nanowire and its thermal and electrical environment. Modeling this system response required coupling the thermal responses and electrical responses of the nanowire. The thermal response involves nanowire heating, cooling and switching between superconducting and normal states during a photodetection event. On the other hand, the electrical response involves current redistribution between the nanowire and the external biasing and measuring circuits. The dynamic interactions that occur between these two responses can be fully captured by combining the electrical and a thermal models of the system in a coupled electro-thermal model.

This electro-thermal model was useful in explaining and predicting the behavior of the SNSPD. For instance, it explains that for a voltage pulse to form at the detector output, a substantial resistance has to develop in the nanowire after a photon has been absorbed. The model also provided insight into parameters that were not directly measurable, such as the temperature profile of the nanowire at every instance in time. This temperature profile was important in determining the dynamics of resistance buildup in the nanowire, and the resetting of the nanowire into the superconducting state. The electrothermal model and calculation results are presented in Sec. 3.3.

The model also predicted that the reset time of the photodetector can be decreased by adding a resistor in series with the nanowire [39]. Since the SNSPD reset time is limited by its L/R time constant, the added series resistance effectively speeds up the device. Motivated by this promise of device speedup, we fabricated on-chip resistors and tested the response of the detectors (discussed in Sec. 3.4). We found that indeed the devices could be made to reset more quickly. However, we were surprised to see that this speedup came at the expense of an apparent suppression in critical currents. This suppression occurred for speedup factors greater than ~ 2.

After further investigation of this unexpected behavior, we found that we were in fact observing the first manifestation of device "latching" in SNSPDs, as there had been no prior report on this. This latching behavior occurred when the devices failed to reset after a detection event due to the stabilization of a resistive segment in the nanowire. Although the electro-thermal model also reproduced the latching behavior, it lacked quantitative agreement. Hence the observed latching started occurring with series resistors that were a factor of ~ 4 smaller than predicted by the model. Latching is discussed in Sec. 3.5. However, obtaining quantitative agreement between model and experiment is beyond the scope of this thesis and is further discussed in our recent work in Ref. [40]

In the following sections, we will describe the electro-thermal model and discuss the its simulation results. A one-dimensional dimensional time-dependent heat equation was used to model the thermal response of the SNSPD while the electrical behavior was modeled using a simple circuit model for the SNSPD and its biasing circuit.

3.2 Background

When our first paper on the electro-thermal model was published [41], Joule heating had not been previously considered to be an important phenomenon in the operation of SNSPDs. Gol'tsman et. al. [2, 38] had described the photodetection process as follows: an absorbed photon creates a local resistive "hotspot" in the nanowire, which forces the superconducting charge carriers (Cooper pairs) to flow around it. As the current density around this hotspot exceeds the critical current density of the nanowire, quantum phase-slips occur [42] causing a resistive barrier to form across the entire cross section of the wire. Semenov et. al. [43] modeled the hotspot formation as the generation of high-energy quasiparticles from photon absorption and the diffusion of these quasiparticles, which eventually recombine into Cooper pairs as the wire becomes superconducting again. In this model, the resistive barrier was thought to collapse immediately after it forms [38] with time constants determined only by the quasiparticle relaxation time.

In our experiments, we realized that during a photodetection event Joule heating causes a large resistance to form in the nanowire. This large resistance had to be greater than the $50\,\Omega$ transmission line resistance to divert a significant amount of current from the nanowire into the transmission line. The diverted current is then amplified and measured as a voltage pulse at the output. Therefore, the small photon-induced resistive barrier that initially forms has to increase rapidly to effectively redistribute this current. The rapid growth of the resistive barrier is caused by Joule heating which increases the temperature of the wire and switches a larger segment of the nanowire into the normal state. As the resistance grows, the device current decreases which allows the nanowire to cool and switch back into the superconducting state. This heating and cooling cycle happens for every photodetection event and is essential to the operation of the SNSPD.

There has been an extensive amount of work on heating effects in superconductors. The interested reader is referred to the review paper of Gurevich and Mints [44] for more information. In superconducting nanowires, the dynamics of heating and cooling in the resistive domains are strongly dependent on how heat is dissipated in the system (e.g. a suspended nanowire would behave differently from a nanowire on a substrate). In addition, the external electrical circuit for biasing and measuring the nanowire will also affect the thermal response of the nanowire. Therefore, the response of a system uniquely depends on its thermal and electrical environment.

3.3 Thermal and electrical model

In the thermal model, the nanowire was approximated as a one-dimensional structure. In this structure, heat generated in a resistive segment of the wire will flow mostly into the sapphire substrate held at 2 K and along the wire. Since heat is generated at the resistive segment, the temperature of this segment will be higher than the temperature of the rest of the wire, which remains superconducting. The temperature profile of the wire was calculated by solving a 1-D heat equation.

Solving a 1-D heat equation is usually trivial for a non-superconducting material at room temperature, but challenging for superconductors. The thermal properties of typical (non-superconducting) materials can be treated as constants, and temperature profiles can be obtained by analytically solving linear differential equations. However, in superconducting materials at cryogenic temperatures, thermal properties are highly dependent on temperature. Also, some thermal properties, such as the specific heat and thermal conductivity, can switch from one value to another depending on the normal or superconducting state of the material. These temperature-and-state dependences of the superconductor's thermal properties result in a nonlinear differential equation that has to be solved numerically.

In the circuit model, the nanowire was modeled as an inductor in series with a variable resistor. The inductor is the kinetic inductance of the nanowire [32] while the resistor is the resistive segment of the nanowire. The value of the resistor changes with time as the resistive segment grows and shrinks. This non-constant resistance was a modification from the fixed resistance used in the circuit model described in our previous work [32]. The circuit model also included the biasing circuit which was modeled as a current source, and a $50\,\Omega$ transmission line, which was modeled as a resistive shunt.

3.3.1 Thermal model

The heat flow that we considered in the thermal model is as shown in Fig. 3-1A. Consider what happens when a small segment of a current-carrying superconducting nanowire suddenly becomes resistive, as depicted as the orange colored region of the nanowire in Fig. 3-1A. The current that continues to flow through this resistor generates heat and raises the temperature of the wire in adjacent superconducting regions. If this new temperature exceeds the critical temperature of the superconductor, the adjacent regions become normal and the resistive segment starts to grow. Otherwise, thermal relaxation occurs and the resistive segment cools by heat escaping into the substrate and along the nanowire, eventually shrinking and possibly disappearing altogether.

Thermally, the NbN nanowire can be modelled using a 1-D heat equation, although physically the nanowire was a 4-nm-thick and 100-nm-wide NbN structure on a sapphire substrate. As the width of the nanowire at 90 nm was smaller than the magnetic penetration depth of NbN, which was $\sim$400 nm [32], the current density in the wire was approximately uniform. For the case where a resistive barrier of uniform length forms across the wire cross section, the heat generated will also be uniform across the wire cross section. Hence the problem can be approximated as being 1-D with no temperature variation across the wire cross section.

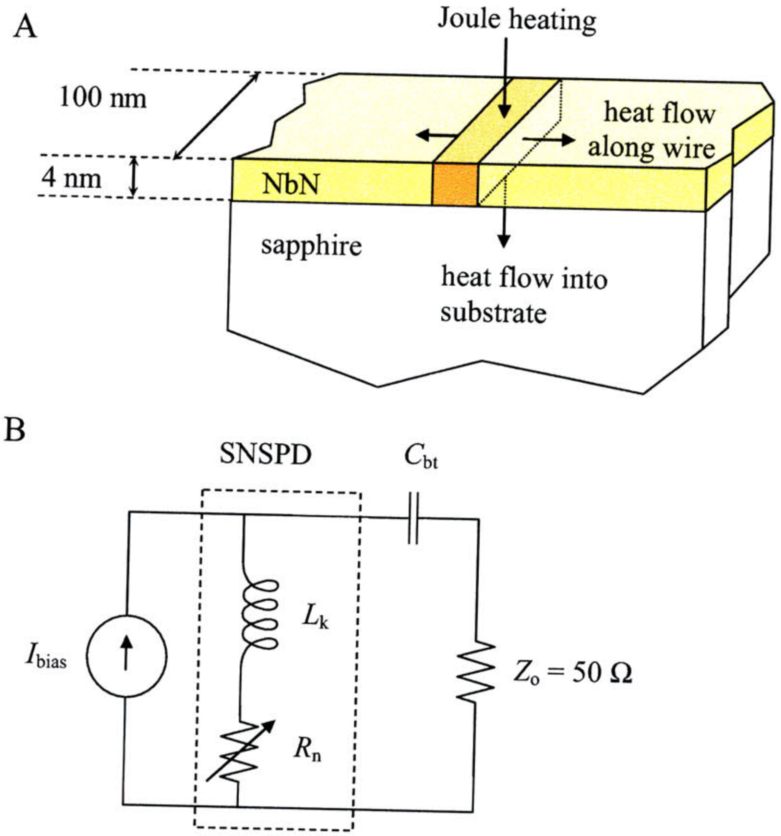

Figure 3-1: (A) Schematic of the thermal model used in our simulation. Using a finite difference numerical method, we treated the nanowire as a quasi-one-dimensional structure with many discrete Δx segments and solved a 1-D time-dependent heat equation for the entire wire. The temperature at each segment and the current flowing through the wire were used to determine if the segment under consideration switches into the normal/resistive state or remains superconducting. (B) A simplified electrical schematic of the SNSPD connected in a typical testing configuration. The SNSPD was modeled as an inductor in series with a resistor, whose value depended on the current through the device and the local wire temperature as determined from the thermal model. The capacitor modeled the AC branch of a bias tee used in our setup, and the transmission line that carried the signal to measurement instruments was modeled as a $50\,\Omega$ impedance.

As shown in Fig. 3-1A, heat generated by Joule heating in the resistive segment of the nanowire flows along the wire and into the substrate while simultaneously changing the local temperature of the nanowire. Therefore a temperature profile forms along the nanowire, with the temperature being highest in the middle of the resistive segment. When a steady state condition occurs (see Sec. 3.5), this temperature profile along the wire stays constant as the generated heat exactly balances the heat dissipation.

Simulation was done using a finite difference numerical method. In this method, we descretized the length of nanowire into segments of length Δx, and solved for the temperature profile of each segment at descretized time steps. The objective of this simulation was to see what would happen after a resitive barrier $\sim 15\,\text{nm}$ in length forms in a current-carrying nanowire. The formation of this resistive barrier is a result of photon absorption and hotspot formation, and its length was chosen to be roughly the thermalization length of the hotspot [2, 43].

The temperature T of each Δx segment was solved using the following time-dependent one-dimensional heat equation,

$$J^2\rho + \kappa\frac{\partial^2 T}{\partial x^2} - \frac{\alpha}{d}\left(T - T_{\text{sub}}\right) = \frac{\partial cT}{\partial t} \tag{3.1}$$

where J is the current density through the wire; ρ is the electrical resistivity, which is non-zero where the wire is normal and zero where the wire is superconducting; κ is the thermal conductivity of NbN; α is the thermal boundary conductivity between NbN and sapphire; d is the wire thickness; T_{sub} is the substrate temperature and c is the specific heat per unit volume of NbN. The first term on the left hand side of equation 3.1 is the heat generated due to Joule heating; the second term is the heat dissipated by thermal conduction along the wire; the third term is the heat dissipated into the substrate; and the term on the right hand side of equation 3.1 is the rate of change in the local energy density of the wire.

We made several assumptions in this model. Firstly, we assumed that the electron and phonon temperatures were the same such that the electronic and phonon subsystems were in thermal equilibrium. These subsystems do not have the same temperature away from equilibrium (as in our case) and a more realistic model should include both temperatures. This model, called the two-temperature or 2T model [45, 46, 47], is typically used for fitting data from pump-probe experiments (see e.g. Ref. [48]) to extract electron-phonon coupling time constants. We chose not to use this model as it would require solving an additional nonlinear heat equation without giving us more insight. We also assumed that the normal regions of the nanowire can switch into the superconducting state instantaneously as long as $I < I_\mathrm{c}(T)$. In reality, the quasiparticle recombination time (typically several picoseconds) will determine how quickly a normal region can become superconducting. If needed, one can include this effect using the method of Rothwarf and Taylor [49]. Instead, we simplified the problem and allowed instantaneous normal-superconducting transitions to occur in our system.

The main difficulty in solving equation 3.1 stems from the dependence of ρ, κ, α and c on temperature and on the normal or superconducting state of the wire. For instance, ρ of a region along the wire at temperature T is zero when the current through that region is less than the critical current at that temperature $I_\mathrm{c}(T)$. In our simulations, we used a phenomenological expression, which we will describe in more detail shortly, to calculate $I_\mathrm{c}(T)$,

$$I_\mathrm{c}(T) = I_\mathrm{c}(0)\left(1 - \left(\frac{T}{T_\mathrm{c}}\right)^2\right)^2 \tag{3.2}$$

where the critical temperature, $T_\mathrm{c} = 10.5\,\mathrm{K}$ for our 4-nm-thick NbN film and $I_\mathrm{c}(0) = 20\,\mu\mathrm{A}$ for a 100-nm-wide wire.

Equation 3.2 was obtained from a fit to experimental measurements over the range of temperatures from 2 K to $T_\mathrm{c} \sim 10\,\mathrm{K}$ as shown in Fig. 3-2. We assumed that this expression, generally true in steady state, can also be extended to the picosecond time scales that we consider. Using this expression, we defined a segment as being resistive when $I > I_\mathrm{c}(T)$ and assigned a constant nonzero value of $\rho = R_\mathrm{sq}d$ to that segment; where $R_\mathrm{sq} = 600\,\Omega/\mathrm{square}$ was the measured sheet resistance of the 4-nm-thick NbN

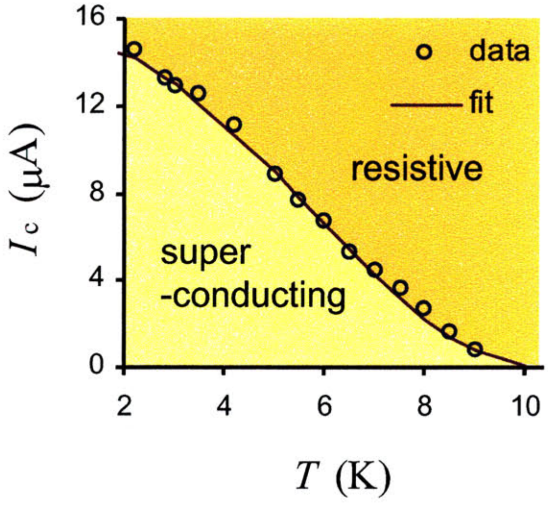

Figure 3-2: Plot of I_c vs T for a typical 90-nm-wide nanowire. Equation (3.2) was used to fit the data points.

film just above T_c. We did this check and assignment in our simulation for each wire segment and at each time step.

We included both the electron and phonon specific heat of NbN in our model. The electron specific heat of NbN c_e was taken to be state and temperature dependent. The expression we used to calculate the normal-state electron specific heat c_{en} of a resistive wire segment is as follows:

$$c_{en} = \gamma T \tag{3.3}$$

where $\gamma \sim 240\,\mathrm{J/m^3K^2}$ is the Sommerfeld constant for thin NbN films [50, 43]. On the other hand, the superconducting electron specific heat c_{es} was calculated using the following expression:

$$c_{es} = Ae^{-\frac{\Delta}{kT}} \tag{3.4}$$

where A is a proportionality constant that is calculated such that
$c_{es}(T_c) = 2.43\ c_{en}(T_c)$ [51], and $\Delta = 3.5\ k\ T_c$ is the superconducting bandgap of NbN [52]. Using $T_c = 10\,\mathrm{K}$, we calculate $A = 2400 \times 2.43 \times e^{3.5} = 1.93 \times 10^5\,\mathrm{J/m^3K^2}$.

The phonon specific heat c_p was taken to be state independent and proportional to T^3. The specific-heat value used in our model was obtained from Ref. [43] and was

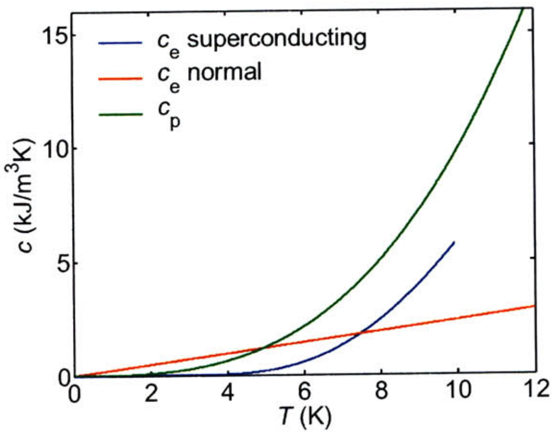

Figure 3-3: Temperature dependence of electron and phonon specific heat of NbN. Electronic specific heat is state dependent and phonon specific heat has a T^3 dependence.

9800 J/m^{3}K at 10 K. Hence $c_\mathrm{p} = 9.8\ T^3$. Putting it all together, $c = c_\mathrm{e} + c_\mathrm{p}$, and $c = 240\ T + 9.8\ T^3$ in the normal state and $c = 1.93 \times 10^5\ e^{-3.5\,T_\mathrm{c}/T} + 9.8\ T^3$ in the superconducting state. The phonon and electronic specific heat of NbN are shown in Fig. 3-3.

The thermal boundary conductivity α between NbN and sapphire determines the rate at which heat is conducted away into the substrate. α determines the phonon escape time from the film. We ignored the state dependence of α and only considered its cubic dependence on temperature (see Ref. [53] for example), i.e. $\alpha = BT^3$, where B is a proportionality constant. However, measurements of thermal boundary resistance (i.e. $1/\alpha$) of Al on sapphire [54] have shown that α was strongly state dependent. We argue that this dependence is not important in our model, as most of the heat escapes into the sapphire substrate from the normal segment of the wire, where the heat was generated.

As we were unable to find any information on α for a NbN-sapphire system in literature, the value of α used in our model was estimated from hysteretic I-V measurements [55]. A rough estimate of α can be found by measuring the retrapping current I_ret in the hysteretic I-V trace. Retrapping occurs when the resistive segment of the nanowire switches into the superconducting state. This switching occurs when the temperature of the resistive segment is less than the critical temperature

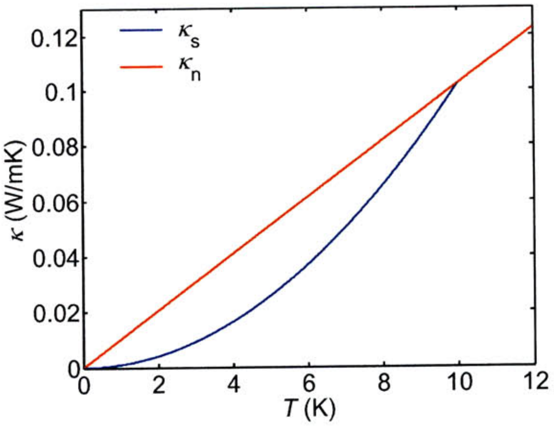

Figure 3-4: Thermal conductivity of NbN vs temperature for superconducting and normal states.

at I_{ret}. This critical temperature T_{ret} can be calculated from equation (3.2) by substituting I for I_{ret} and solving for T to obtain $T_{\mathrm{ret}} \sim 4\,\mathrm{K}$ for typical values of $I_{\mathrm{ret}} \sim 4\,\mu\mathrm{A}$. Since the I-V measurements were steady state measurements, steady state heat balance can be approximated by $\alpha(T_{\mathrm{ret}} - T_{\mathrm{sub}})/d \cong I_{\mathrm{ret}}^2\rho/(Wd)^2$ where $W \sim 90\,\mathrm{nm}$ is the wire width. This rough approximation was obtained by setting the time dependent term in equation (3.1) to zero and taking $\kappa\frac{\partial^2 T}{\partial x^2} \cong 0$. The estimated value of α was $\sim 8 \times 10^5\,\mathrm{W/m^2K}$ at $10\,\mathrm{K}$.

The final parameter used in our model, the thermal conductivity of NbN κ, was both state and temperature dependent as shown in Fig. 3-4. By applying the Wiedemann-Franz law ($\kappa = LT/\rho$, where $L = 2.45 \times 10^{-8}\,\mathrm{W\Omega/K^2}$ is the Lorenz number and $\rho \sim 2.4\ \mu\Omega\mathrm{m}$ is the electrical resistivity), we can calculate the temperature dependence of the normal state thermal conductivity κ_{n} with the knowledge of ρ. The superconducting state thermal conductivity κ_{s} was calculated such that $\kappa_{\mathrm{s}}/\kappa_{\mathrm{n}} = T/T_{\mathrm{c}}$, similar to the treatment in Ref. [55]. We also ignored the phonon contribution to ρ which should be very small for a thin film at the low temperatures under consideration. Since the phonon mean free path is very short in a thin film, the phonon contribution to the thermal conductivity is negligible compared to the electronic contribution [56].

3.3.2 Electrical model

Electrically, the SNSPD was modeled as an inductor in series with a resistor as shown in Fig. 3-1B. The inductor L_k represented the kinetic inductance of the superconducting nanowire as explained in Ref. [32]. The resistance R_n in series with the inductor was the total resistance formed from a contiguous number of segments that switched into the normal state.

Experimentally, we bias our devices using a bias tee and a low-noise current source. The DC port of the bias tee was modeled as a constant-current source and a capacitor $C_\mathrm{bt} = 0.02\,\mu\mathrm{F}$ was included to represent the AC port of the bias tee. The impedance Z_o of the transmission line connecting the probe to RF amplifiers was modeled as a $50\,\Omega$ load. We solved for the current I through the nanowire using the following equation.

$$C_\mathrm{bt}\left(\frac{\mathrm{d}^2 L_\mathrm{k} I}{\mathrm{d}t^2} + \frac{\mathrm{d}(I R_\mathrm{n})}{\mathrm{d}t} + Z_\mathrm{o}\frac{\mathrm{d}I}{\mathrm{d}t}\right) = I_\mathrm{bias} - I \tag{3.5}$$

Note in equation 3.5 that R_n is coupled to the thermal model and is not a constant value. The thermal model determines the length of the normal region which is proportional to R_n. The bias current in our calculation was set to 90% of $I_\mathrm{c}(T_\mathrm{sub})$ (3.2).

The kinetic inductance of the nanowire is a function of the device current [32, 23]. For instance, the kinetic inductance at I_c is 50 % higher than the kinetic inductance at zero current. Due to this varying inductance, the voltage across L_k is $L_\mathrm{k}\,\mathrm{d}I/\mathrm{d}t + I\,\mathrm{d}L_\mathrm{k}/\mathrm{d}t$, instead of just the first term. However, for values of $I < 0.9\,I_\mathrm{c}$, the first term dominates. Hence, for the sake of simplicity, we treated L_k as constant and did not include this effect in our model. For a more detailed analysis, please see Appendix B.

We also noted that regions in the nanowire that became resistive also lost its kinetic inductivity. As the kinetic inductance of the nanowire was a manifestation of the superconducting charge carriers, resistive segments that were devoid of superconducting charge carriers did not have any kinetic inductance. This effect gave rise to an extra $I\,\mathrm{d}L_\mathrm{k}/\mathrm{d}t$ term that depended on the rate of change of the nanowire resistance R_n. Mathematically, this extra term, $I\,\mathrm{d}L_\mathrm{k}/\mathrm{d}t = I\,\mathrm{d}R_\mathrm{n}/\mathrm{d}t \times \mathrm{d}L_\mathrm{k}/\mathrm{d}R_\mathrm{n}$. With the resistance per unit square measured as $R_\mathrm{sq} = 600\,\Omega/\mathrm{square}$ and the kinetic inductance per unit square $L_\mathrm{sq} = 90\,\mathrm{pH/square}$ for our devices, $\mathrm{d}L_\mathrm{k}/\mathrm{d}R_\mathrm{n} = -L_\mathrm{sq}/R_\mathrm{sq} = -150 \times 10^{-15}\,\mathrm{H}/\Omega$. We now compare the magnitude of this extra $I\,\mathrm{d}L_\mathrm{k}/\mathrm{d}t$ term with the $L_\mathrm{k}\,\mathrm{d}I/\mathrm{d}t$ term. Taking the ratio of the two terms resulted in $I/L_\mathrm{k}\Delta R_\mathrm{n}/\Delta I \times 150 \times 10^{-15}$. Using typical values of $I = 16\,\mu\mathrm{A}$, $\Delta I = 12\,\mu\mathrm{A}$, $\Delta R_\mathrm{n} = 1500\,\Omega$, and $L_\mathrm{k} = 60\,\mathrm{nH}$ resulted in a ratio of only 0.005. As this term was negligibly small, we neglected it in our calculations, but also noted that this term might become more important for devices with much smaller kinetic inductances that those calculated in our simulations.

We used the Crank-Nicholson finite difference method in our simulations to solve equations 3.1 and 3.5. The Crank-Nicholson method is a combination of forward and backward Euler methods that ensures numerical stability but requires Gaussian elimination to solve for the temperature profile along the wire at every time step. For each time step, both temperature-and-state dependent parameters were updated and a conditional check was made to determine the new length of the resistive segment. In this check, a segment was resistive if I exceeded the critical current at the temperature of the segment. The electrical model was solved for every time step using the Laplace transform method with initial conditions given by the previous time step.

3.3.3 Results

Thermal effects are typically slow in macroscopic structures. For instance, it takes several minutes for ice to melt on a hot pavement. However, in nanoscopic structures such as the nanowire detectors, thermal effects can be extremely fast. For instance, the heating and cooling of the nanowire occur in less than a nanosecond. This ultrafast thermal response is due to the thinness of the nanowires (4 nm), the low specific heat of materials at cryogenic temperatures, and the low thermal boundary resistance between nanowire and substrate.

Using the electro-thermal model, we were able to simulate the growth of the normal region along the wire, the change in current through the wire and the temperature increase along the wire after the formation of a resistive barrier. The calculation results are shown in Fig. 3-5 for a device with kinetic inductance $L_\mathrm{k} = 807.7\,\mathrm{nH}$. In Fig. 3-5A, we show the device current, which starts to sharply drop at $t = 0$ with an $L/R = L_\mathrm{k}/(Z_\mathrm{o} + R_\mathrm{n})$ time constant. The device then switches back into the superconducting state at $I \sim 4\,\mu\mathrm{A}$ at which point the current slowly increases with an $L/R = L_\mathrm{k}/Z_\mathrm{o}$ time constant. The quick buildup and collapse in nanowire resistance R_n is shown in Fig. 3-5C. As shown, the resistance increases to a maximum value of $\sim 5.5\,\mathrm{k\Omega}$ at $t \sim 0.15\,\mathrm{ns}$ after which it collapses to zero at $t \sim 0.23\,\mathrm{ns}$. This maximum resistance corresponds to ~ 10 squares of the nanowire switching normal, which, in the case of a 90-nm-wide wire, is a total length of ~ 900 nm. This total length of resistive segment can be seen in Fig. 3-5B where we plot the temperature of the nanowire as a color map in space and time. The maximum temperature of the nanowire in this case was $\sim 12\,\mathrm{K}$.

The voltage pulse measured at the output is due to the current redistribution from the nanowire into the transmission line. In the experimental setup, this signal was amplified by a cascaded amplifier with total gain of $\sim 48\,\mathrm{dB}$ and 20 MHz high-pass cutoff. Hence, the output signal can be calculated by multiplying the calculated amount of current dip with the transmission line impedance of $50\,\Omega$, scaling the result by the total voltage amplification of 48 dB, and high-pass filtering the signal. In Fig. 3-5D, this calculated response with no free parameters is compared to a typical voltage pulse (time averaged) obtained for an SNSPD with a measured kinetic inductance of 807.7 nH. The agreement between calculation and experimental data was good.

The voltage pulse was measured using the device as shown in the scanning electron micrograph in Fig. 3-6B. We chose to use a device with a large kinetic inductance so that the rise times of the pulses are long enough to be observable on a 6-GHz real-time oscilloscope as shown in the inset of Fig. 3-5D.

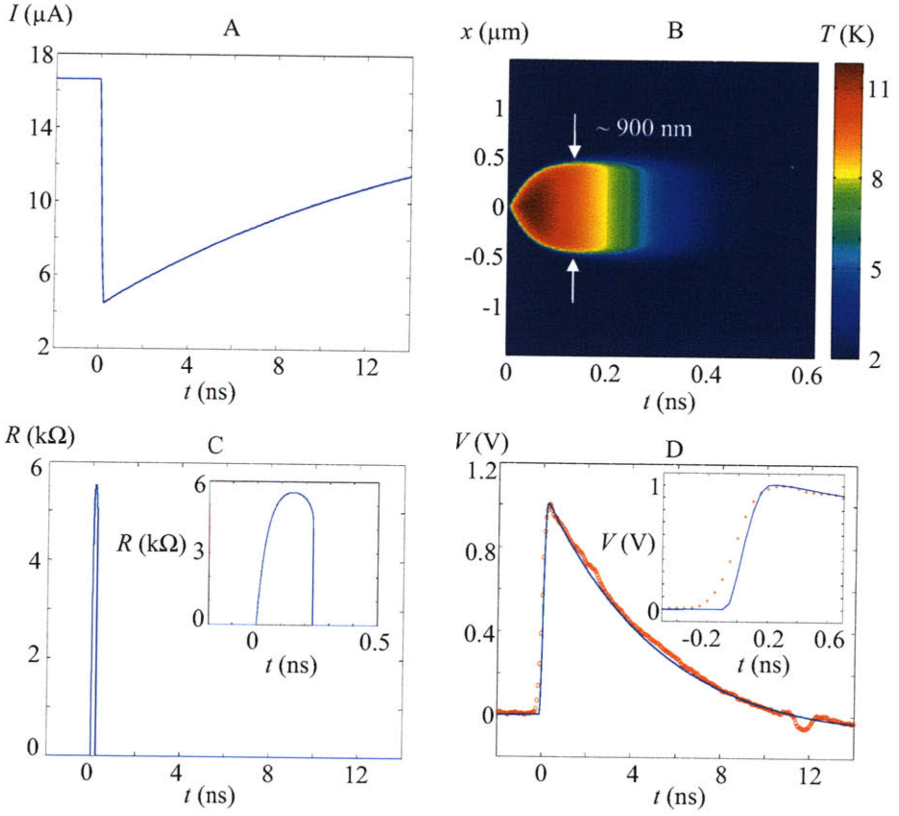

Figure 3-5: (A) Plot of calculated current through an SNSPD with $L_\mathrm{k} = 807.7\,\mathrm{nH}$ vs time. The photon-induced resistive barrier forms at t = 0. (B) Map of calculated temperature (shown using colors) at different positions along the wire and in time. Calculations show that the wire temperature increases to a maximum value of $\sim 12\,\mathrm{K}$. (C) Plot of calculated total normal state resistance vs. time. Inset shows in greater detail the gradual increase of the resistance at t = 0 and a sharper decrease back into the superconducting state at t = 230 ps. (D) Plot of calculated voltage pulse (solid line) in comparison to an experimentally measured time-averaged pulse (red circles). The undershoot in voltage below 0 V was due to the high-pass cutoff of the RF amplifiers while the dip at $\sim 12\,\mathrm{ns}$ was due to reflections along the transmission line. Inset shows the rising edge of the voltage pulse. The rise time of the numerical result was shorter than that of the measured pulse.

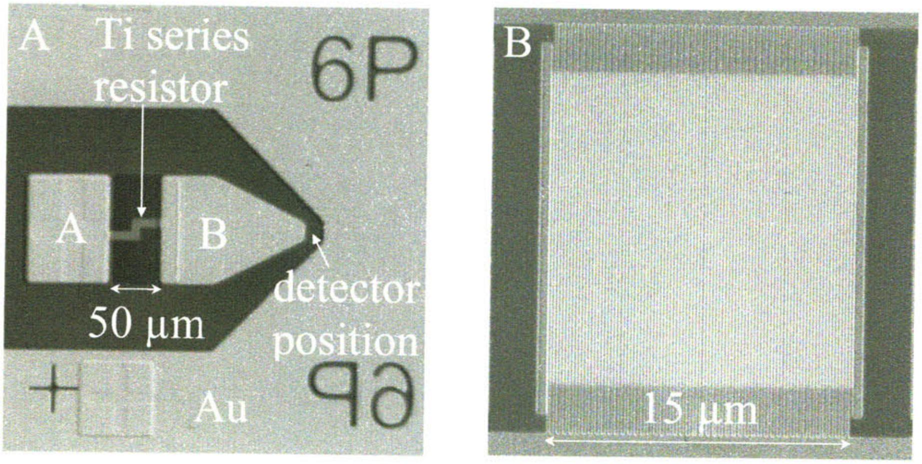

Figure 3-6: (A) Optical micrograph of the Au contact pads used to make electrical connection to the SNSPD. The titanium resistor bridges pads A and B. This configuration permitted us to bias the SNSPD through the resistor by landing the probe at position A or to bypass the resistor by landing the probe at position B. The outer Au pad was at signal ground. (B) Scanning-electron micrograph (SEM) of a 15-by-15-µm meander SNSPD with a 50% fill factor, wire width of 100 nm and total wire length of $\sim 1\,\mathrm{mm}$.

3.4 Increasing the speed of SNSPDs

The time constant for the resetting of SNSPDs [32] is equal to the ratio of its kinetic inductance L_k to the impedance connected across it, i.e. the L/R time constant. One can increase the device speed by reducing this L/R time constant. Reducing L_k would require reducing the total length of the nanowire. This reduction in length would lead to either a smaller active area or a lower fill-factor meander, both of which are detrimental to the detection efficiency of the device. We chose instead to increase the resistance "seen" by the device by adding a resistor in series with the device. The process for fabricating on-chip series resistors is described in Appendix A.

We fabricated an on-chip Ti resistor in series with the detector as shown in the optical micrograph of Fig. 3-6A and the schematic of Fig. 3-7A. Using our model, we calculated the effect that this modification had on device performance. As shown in Fig. 3-7B, our model accurately predicts the speed up in device performance due to the series resistance. The series resistance value was $192\,\Omega$, and the reduction in the L/R time constant by a factor of five resulted in a device speed-up by the same factor. In these calculations the full electro-thermal model was used only to determine the

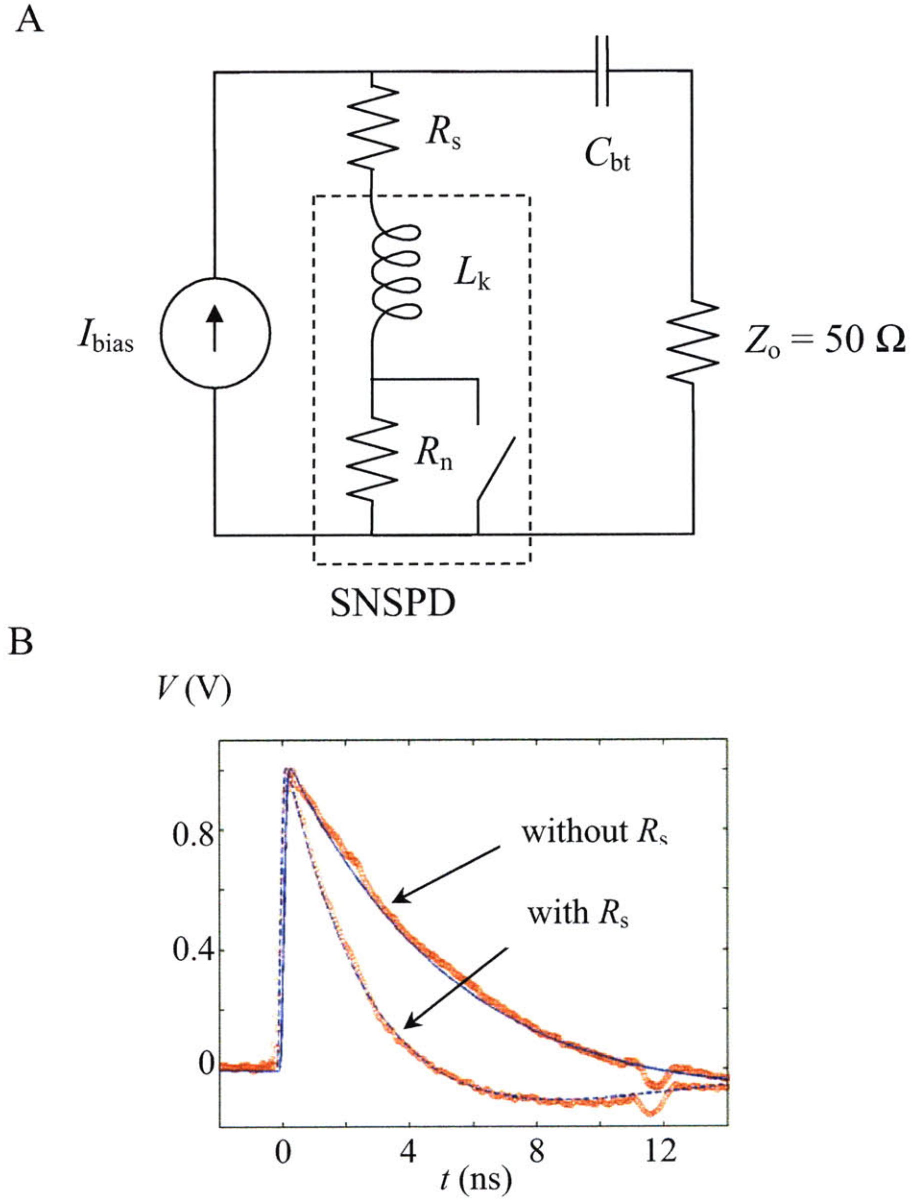

Figure 3-7: (A) Schematic of modified electrical model after adding a resistor Rs in series with the SNSPD. The added series resistance will reduce the reset time of the detectors by lowering the time constant. (B) Comparison of voltage pulses measured with and without $R_s = 192\Omega$, showing a shortening of the reset time when the SNSPD was biased through Rs. The actual speed-up was about a factor of five although this speedup is not clear from the plots here due to the high-pass cutoff at 20 MHz, which makes long pulses look shorter. The dashed and solid lines are the simulation results for SNSPDs biased with and without Rs respectively. We used the same bias currents when measuring both voltage pulses resulting in the same pulse height of $\sim 1\,\mathrm{V}$ after $\sim 48\,\mathrm{dB}$ signal amplification.

rising edge of the voltage pulse (i.e. when the resistor in the electrical model depended on the size of the growing or decaying hotspot). Once the wire switched back into the superconducting state, the electrical model was decoupled from the thermal model and the circuit model alone was sufficient for calculating the current in the SNSPD as it resets.

3.5 Latching

The electro-thermal model and device-speedup experiments showed that we could decrease the reset time by adding a resistor in series with the device. This success motivated us to see how much we could speed up the devices, and led us to add larger series resistors. When we did this, we found that the devices started switching into the normal state even before they were biased to I_c, hence giving the appearance of a suppressed critical current. Further investigation into these unexpected suppression of critical currents showed that the devices were actually latching into a stable resistive state.

Our report in Ref. [41] was the first account of latching in SNSPDs. Our results show that, although we could speed up the devices by adding a series resistor, latching sets a lower limit to the reset time of SNSPDs.

Proper device operation demands that the nanowire switches back into the superconducting state after a photodetection event. However, in some cases (which we will explain later), a segment of the nanowire stays resistive after absorbing a photon, and the nanowire no longer detects photons. In this latched state, the resistive segment is sustained by Joule heating that is exactly balanced by the dissipated heat. This latched state is stabilized by negative feedback provided by the electric circuit, which we will explain shortly.

The electro-thermal model has explained the formation of a measurable voltage pulse during a photodetection event (Sec. 3.3.3) and predicted device speedup (Sec. 3.4). In this section, we show that simulations using the electro-thermal model also predict latching. The qualitative agreement between simulation and experiment adds to the validity of the electro-thermal model.

The device latching behavior has been studied extensively by A.J. Kerman and myself and recently documented in our paper in Ref. [40]. In this paper, we described the electro-thermal model in the perspective of a feedback system in which the electrical system provides negative feedback to the thermal system.

A simplified description of the feedback is as follows: when a photon is absorbed and a resistive segment grows in length, the electric circuit tries to counteract this growth in resistance (i.e. provides negative feedback) by diverting current away from the nanowire and into the transmission line, which then allows the resistive segment to cool and eventually reset into the superconducting state. In this normal operation of the detector, the electrical response is slower than the thermal response, where changes in the current do not occur fast enough to halt the growth of the resistive segment and prevent heating of the nanowire altogether.[1] Once enough current has been diverted away, the resistive segment starts to cool. The negative feedback then works in the opposite direction, by increasing current flow through the nanowire to sustain heating and to maintain the resistive segment. At this point, if the feedback is not fast enough, the resistive segment will completely collapse into the superconducting state and the wire resets. On the other hand, latching could occur if the feedback is fast enough to prevent the resistive segment from collapsing.

In our calculations and experiments, we see that two conditions need to be satisfied in order for a device to latch.

1. For a given bias condition and biasing circuit, the device may latch if we can find a steady-state solution to the electro-thermal model where a resistive segment can be sustained in the nanowire.

2. This steady-state solution needs to be stable. In other words, the electro-thermal feedback needs to be fast enough to stabilize the system in this steady state.

In the final subsection 3.5.3, we will discuss the steady state solutions to the

---

[1] It is by virtue of this slow feedback that the SNSPDs work in the first place.

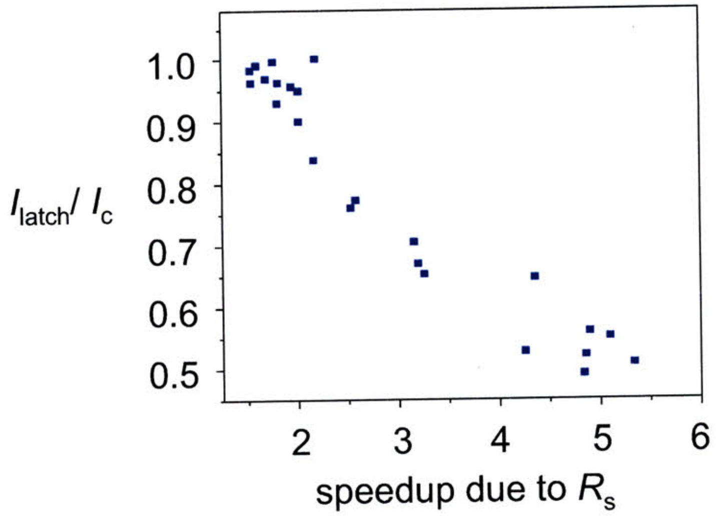

Figure 3-8: Plot of measured switching current (normalized by I_c) as a function of speedup $(R_s + 50\,\Omega)/50\,\Omega$. Switching current decreases with increasing R_s as the device latches before it can be biased close to I_c.

electro-thermal model. The discussion on stability of these states and a more comprehensive description of the latching behavior can be found in Ref. [40] and will not be discussed here.

3.5.1 Experimental observation of latching

In expriments, we observed that a device would latch when we tried to speed it up by adding a series resistor larger than a certain value. We observed that beyond the factor of ~ 2 speedup, the critical currents of the device seemed to be suppressed. This apparent suppression in critical current worsened with larger series resistors $R_{\mathrm{s}} > 50\,\Omega$, as the device switched into the resistive state at bias currents I_{latch} appreciably lower than the true critical current I_{c} of the device. As shown in Fig. 3-8, with increasing speedup $(R_{\mathrm{s}} + 50\,\Omega)/50\,\Omega$ the device switching currents I_{latch} decreased.

This apparent suppression in critical current could be explained as follows: as we biased this latching device (which was in series with a large R_{s}) below I_{latch}, the device would occasionally detect photons and still reset into the superconducting state after each detection event. However, once the bias current is increased above I_{latch}, the device latches into a stable resistive state. The device at this point would need to be actively reset by manually shutting off its bias current, so that it becomes superconducting, and then re-biasing it. In principle, we could have a device biased close to I_c for a short period of time and not have the device latch if no detection events occur within that time frame.

Given the description above, a latching device would therefore generate one last voltage pulse before latching. A snapshot of this last pulse is shown in Fig. 3-9. The device biased to $I_{\text{bias}} \geq I_{\text{latch}} < I_c$ would detect photons normally for a short period of time before it generated one last pulse and latched. To capture this last pulse, the oscilloscope was set to trigger only on a pulse that had a width greater than a set value. This last pulse, which was a step function in voltage, was high-pass filtered by the amplifier in our setup resulting into a pulse as shown in the bottom plot of Fig. 3-9, which is still longer than a typical pulse. We expected a step function in voltage due to the stable resistive segment that formed, which resulted in a constant voltage across the detector.

The latched state, however, was not alway stable and the nanowire would sometimes unlatch (due to ambient perturbations such as photon absorption) and reset back into the superconducting state. The stability of the latched state is only briefly discussed in Sec. 3.5.3 and fully analyzed in Ref. [40].

This latching behavior is very different from the behavior of a device biased above its true I_c. We see in Fig. 3-10 that for the same device biased without the series resistor, the device does not show a last pulse before it becomes completely normal. Instead a burst of so called relaxation oscillation pulses [57] was generated when the bias current exceeded I_c. This behavior was distinct from the latching behavior in Fig. 3-9 and suggested that biasing the devices through the series resistors did not suppress I_c. Instead the device was latching before we could bias it close to its true I_c.

3.5.2 Electro-thermal model simulation of latching

We could simulate device latching in our electro-thermal model by using large values of R_s. Our model calculations show that for a fixed I_{bias} and L_k, a device would

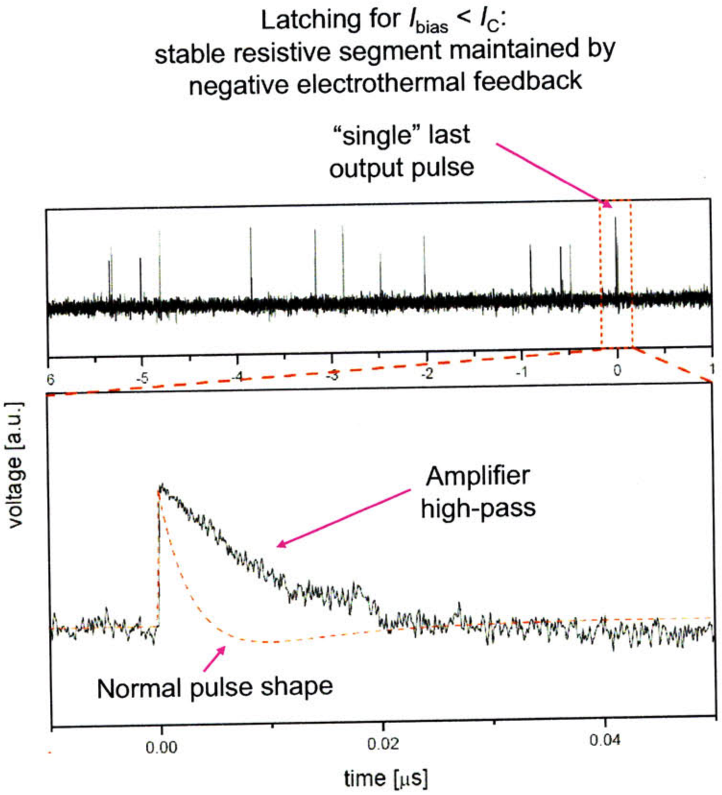

Figure 3-9: Measured voltage pulses for a device right before latching. When the device latched, it generated a single last pulse after which a stable hotspot formed that prevented the device from detecting any more photons. Latching occured at $I_{\text{bias}} < I_{\text{c}}$. In this particular example, the latched state was only marginally stable and the device could unlatch at $\sim 0.02\,\mu\text{s}$, which we see a small, but sharp, drop in voltage.

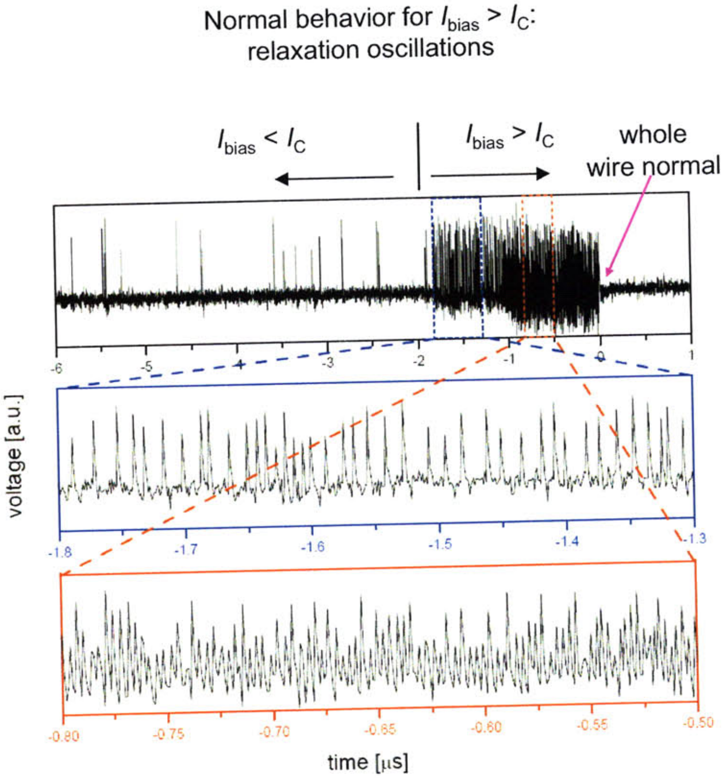

Figure 3-10: Measured voltage pulses for the same device as in Fig. 3-9 but without the series resistor. The device, in this case, did not latch. Instead of a single last pulse that formed when the device latched, here we saw a burst of high-frequency pulses called relaxation oscillations that occurred when $I_{\text{bias}} > I_{\text{c}}$ [57]. The frequency of these relaxation oscillations increases with increasing I_{bias} until the entire nanowire switched normal.

eventually latch as we increased R_s. This behavior is consistent with experimental observations, i.e. we could speed up a device by adding a small R_s but the device would latch if we added too much series resistance.

In our calculations on device latching, we used $L_k = 60\,\text{nH}$ instead of 807.7 nH as we saw experimentally that smaller inductance devices would latch more easily. Fig. 3-11A shows the current through the nanowire at different times for several values of R_s. We saw that for values of $R_s > 200\ \Omega$, latching occured and the device did not reset, i.e. the current did not increase back to its original value but settled to a stable value.

Fig. 3-11B shows numerical results of the trajectories in current-temperature (I-T) space for devices biased through different values of R_s. Here we have plotted the device current and the highest temperature of the normal segment, which occurred at the middle of the length of the segment, for different instances in time. Notice that latching did not occur if the trajectory crossed into the superconducting domain of the I_c vs T plot, at which point the device became superconducting again.

Latching occurred when the negative electro-thermal feedback was fast enough, i.e. the L/R time constant was low enough, to oppose the reduction in nanowire resistance. This electro-thermal feedback was a passive feedback that arose from the inductive nature of the nanowire. The electric circuit opposes this reduction in resistance by increasing the device current to preventing the nanowire from switching into the superconducting state. In Fig. 3-12 we show that for $R_s > 200\,\Omega$, the nanowire resistance could not collapse as the feedback was quick enough to stabilize and sustain the heating.

Within the nanosecond time frame, the trajectories in Fig. 3-11B settled into a stable state in the resistive domain of the I-T plot. In this state, the heat generated due to Joule heating was balanced by the heat dissipated into the substrate and along the wire. In our experimental setup, the capacitive branch of the bias-tee prevented steady state current distribution between the nanowire and the transmission line. Thus a self-heating hotspot was only temporarily sustained. Over a much longer time scale (set by the capacitive time constant of the system, which was several microseconds long) the current through the wire increased to its original value because the bias current had no path to ground other than through the nanowire. A runaway effect would then occur as the increasing current drove the entire nanowire normal.

In simulations, latching occurred only for resistors larger than $200\,\Omega$ which was ~ 4 times higher than what was observed experimentally. This lack of quantitative agreement could be due to inaccuracies in the values for the thermal properties used in the model. It is also unclear if other physical effects, which we have not considered, may be responsible for the poor quantitative agreement.

In the following subsection, we will find the steady-state solutions to a simplified electro-thermal model. A steady-state solution where a resistive segment exists is a prerequisite for device latching, although it does not ensure latching, as the resistive segment may not be stable.

3.5.3 Steady-state solutions to the electro-thermal model

When the nanowire latches, it transitions into a steady-state where a resistive segment can be sustained indefinitely (in the absence of perturbations). It is therefore useful to find these steady-state solutions to the electro-thermal model because the existence of such solutions would indicate the possibility of device latching. On the other hand, the absence of a steady-state solution would mean that the device would never latch. Therefore, finding circuit parameters that result in no steady-state solutions would ensure a device that never latches.

The simulations that we have shown so far were done numerically to obtain the dynamic response of the nanowire. Although the results were qualitatively in agreement with experiment, the model was not well suited for studying steady-state solutions. Due to the temperature and state dependencies of the parameters used, finding steady-state solutions required multiple iterations and was computationally intensive.

Here, we instead seek to solve the steady-state solutions for the electro-thermal model analytically. Analytic solutions can be found when we simplified the problem significantly by removing all temperature and state dependencies of the thermal properties.

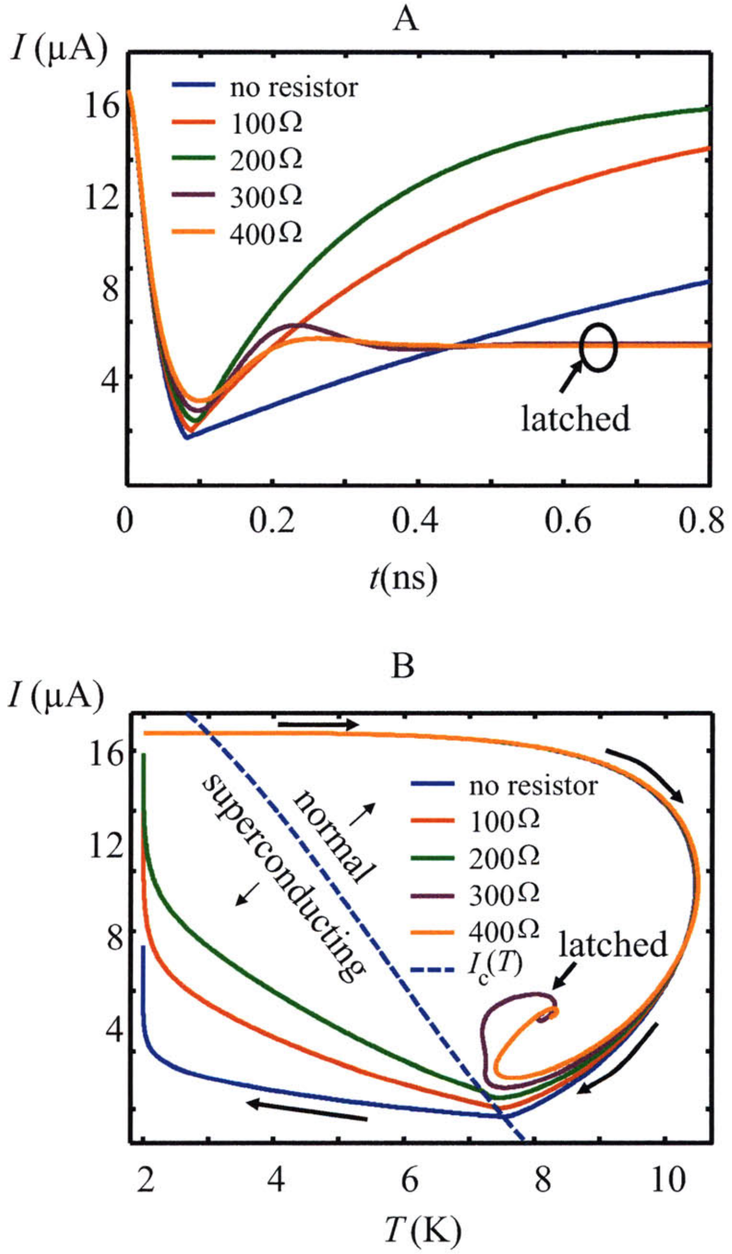

Figure 3-11: (A) Plot of calculated current through the nanowire vs time for a device with $L_{\mathrm{k}} = 60\,\mathrm{nH}$. Legend shows value of R_{s} in ohms. Device latched for $R_{\mathrm{s}} > 200\Omega$ where the device current did not reset to its original value. (B) Plot of hotspot I-T trajectories for different values of R_{s}. The dashed line is the I_{c} vs T plot following equation (3.2). Arrows show the direction of movement of trajectory in I-T space as time progresses. Devices that latch do not cross into the superconducting side of the I_{c} vs T plot.

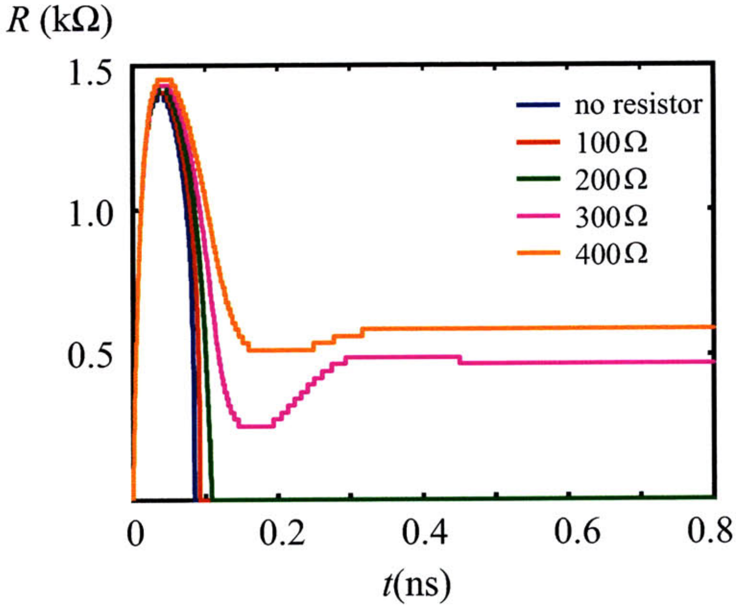

Figure 3-12: Plot of calculated resistance in the nanowire vs time for a device with $L_\mathrm{k} = 60\,\mathrm{nH}$. Legend shows value of R_s in ohms. Device latched for $R_\mathrm{s} > 200\Omega$ where the electro-thermal feedback was fast enough to prevent the nanowire from collapsing into the superconducting state. Instead the feedback quickly sustained heating and stabilized a resistive segment.

The following is the procedure for finding the steady-state solutions: first, we find the steady-state analytic expression for the temperature profile for the nanowire. We then find the steady-state expression for the electric circuit, and add the condition that at steady-state, the temperature at the normal-superconducting N-S boundary of the nanowire is equal to the critical temperature for a given device current.

We start with equation (3.1). From this equation, we can find expressions for the thermal time constant $\tau_\mathrm{th} = c\,d/\alpha$ and the thermal healing length $\eta = \sqrt{\kappa\,d/\alpha}$. We then define a characteristic current density, $J_\mathrm{ss} = \sqrt{\frac{\alpha}{\rho\,d}\,(T_\mathrm{c} - T_\mathrm{sub})}$ and cast equation (3.1) into dimensionless units by defining $\tau = t/\tau_\mathrm{th}$, $\theta = T/T_\mathrm{sub}$, $y = x/\eta$ and $j = J/J_\mathrm{ss}$ to obtain

$$\frac{\mathrm{d}^2\theta}{\mathrm{d}y^2} + j^2(\theta_\mathrm{c} - 1) - (\theta - 1) = \frac{\mathrm{d}\theta}{\mathrm{d}\tau} \tag{3.6}$$

The steady-state solution for the temperature profile can be found by setting $\frac{\mathrm{d}\theta}{\mathrm{d}\tau} = 0$. For a resistive segment of length $y = D$, the solutions were obtained by solving for the homogeneous and specific solutions to equation (3.6) with $\frac{\mathrm{d}\theta}{\mathrm{d}\tau} = 0$. The resultant solutions are:

$$\theta = \begin{cases} -j^2(\theta_\mathrm{c} - 1)e^{-D/2}\cosh(y) + 1 + j^2(\theta_\mathrm{c} - 1) & \text{if } |y| \le D/2 \\ j^2(\theta_\mathrm{c} - 1)e^{-|y|}\sinh(D/2) + 1 & \text{if } |y| > D/2 \end{cases} \tag{3.7}$$

This solution ensures a smooth and continuous temperature function at the N-S boundary and a symmetric temperature profile about the center of the resistive segment at $y = 0$.

To solve the steady-state equation, we need to know j and D. Thus, we need two more constraints. One of these constraints can be found from the circuit model in Sec. 3.3.2, which we can further simplify by removing the capacitor in the circuit. This simplified model will be valid for time scales smaller than the RC time constant of the system which is $\sim 1\,\mu\mathrm{s}$. The resultant equation is thus:

$$L_\mathrm{k}\frac{\mathrm{d}I}{\mathrm{d}t} + IR_\mathrm{n} = I_\mathrm{bias}\,Z_o \tag{3.8}$$

We can also express this equation in dimensionless units by defining $j = I/(A\,J_\mathrm{ss})$ (where A is the wire cross sectional area), $r = R_\mathrm{n}/Z_o$, $\tau_\mathrm{e} = L_\mathrm{k}/(R_\mathrm{n} + Z_o)$, to get:

$$\frac{\tau_\mathrm{e}}{\tau_\mathrm{th}}\frac{\mathrm{d}j}{\mathrm{d}\tau} + j = \frac{j_\mathrm{bias}}{r+1} \tag{3.9}$$

Setting $\frac{\mathrm{d}j}{\mathrm{d}\tau} = 0$, we get the steady-state equation,

$$j = \frac{j_\mathrm{bias}}{r+1} \tag{3.10}$$

Finally, the third constraint comes from the condition for superconductivity, i.e. equation (3.2), which we can approximate as a straight line for simplicity:

$$j_\mathrm{c} = \begin{cases} j_\mathrm{co}(1 - \theta/\theta_\mathrm{c}) & \text{if } 0 \le \theta \le \theta_\mathrm{c} \\ 0 & \text{otherwise} \end{cases} \tag{3.11}$$

We can then equate the temperature at $D/2$, which is at the N-S boundary, to the critical temperature at j, i.e. $\theta_\mathrm{c}(1 - j/j_\mathrm{co})$. Realizing that $D = rAZ_o/\eta\rho$, and combining equation (3.7), (3.10) and (3.11), we obtain the following equation which we can then use to numerically solve for j as a function of j_{bias}, and Z_o.

$$\frac{j^2}{2}(\theta_{\mathrm{c}} - 1)\left(1 - e^{((j_{\mathrm{bias}}/j)-1)(AZ_o/2\eta\rho)}\right) + 1 = \theta_{\mathrm{c}}(1 - j/j_{\mathrm{co}}) \tag{3.12}$$

Examples of graphical solutions to this equation is shown in Fig. 3-13 and 3-14. The left-hand side (LHS) and right-hand side (RHS) of equation (3.12) were both equal to the normalized temperature θ, hence the plots have θ on the y-axis. As seen in Fig. 3-13, where $j_{\mathrm{bias}} = 1.27 j_{\mathrm{co}}$, a solution existed where the traces for the left-hand side (LHS) and right-hand side (RHS) of equation (3.12) intersected. At the intersection point, we obtain the value of normalized current through the nanowire j and θ at the N-S boundary. On the other hand, when $j_{\mathrm{bias}} = 0.54 j_{\mathrm{co}}$ in Fig. 3-14, no solution existed as the RHS and LHS traces did not intersect.

Note that the steady-state solution is independent of the inductance of the device and depends only on Z_{o} and j_{bias}. The steady-state device currents I_{ss} and nanowire resistances R_{ss} for a range of bias currents I_{bias} and different Z_o values are plotted in Fig. 3-15A and B respectively. In these calculations, we used constant values for the thermal properties obtained from the values in Sec. 3.3.1 at T_{c}.

Fig. 3-15A shows the steady-state device current solutions I_{ss} as a function of bias current I_{bias}. The $I_{\mathrm{bias}} = I_{\mathrm{dev}}$ line, from 0 to I_{c}, corresponds to the device being superconducting. The curved solid lines denote the presence of a resistive steady-state solution. For a given Z_{o} value, resistive steady-state solutions exist beyond a minimum I_{bias} value. A device will definitely not latch when biased within the range of I_{bias} where no resistive steady-state solution exists. On the other hand, the device could possibly latch if biased above the minimum I_{bias} value.

We see that the minimum I_{bias} value also decreases with increasing Z_{o}. This decrease in minimum I_{bias} values suggests the possibility of latching at a lower I_{bias} values as Z_{o} is increased. This trend is consistent with experimental observations. For instance, a device with $Z_{\mathrm{o}} = 200\,\Omega$ cannot latch at $10\,\mu\mathrm{A}$ bias current but a device with $Z_{\mathrm{o}} = 500\,\Omega$ could.

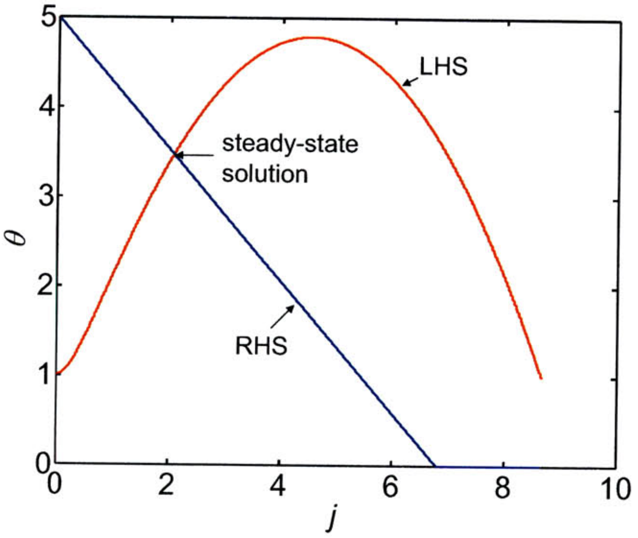

Figure 3-13: Plot of the left-hand side (LHS) and right-hand side (RHS) of equation (3.12) as a function of j for the case where $j_{\text{bias}} = 1.27 j_{\text{co}}$, and $Z_o = 50\,\Omega$. In this case, a solution existed where the LHS trace intersects the RHS trace, i.e. where LHS = RHS. The solution, given by the point of intersection, gave the current through the nanowire and the temperature at the N-S boundary.

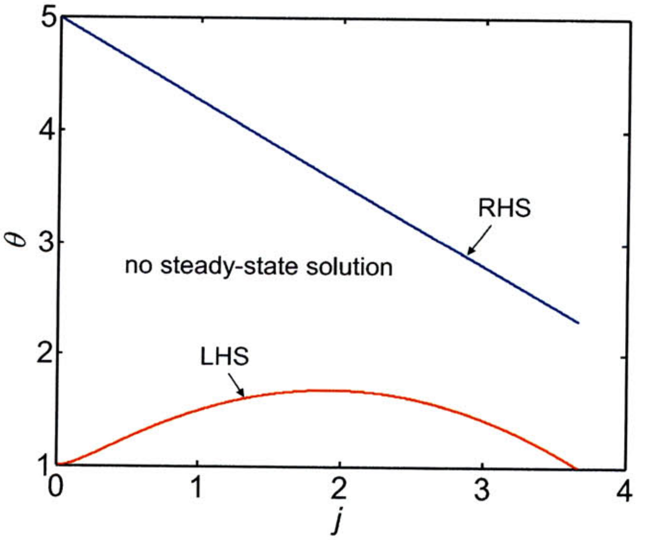

Figure 3-14: Plot of the left-hand side (LHS) and right-hand side (RHS) of equation (3.12) as a function of j for the case where $j_{\text{bias}} = 0.54 j_{\text{co}}$, and $Z_o = 50\,\Omega$. In this case, no solution existed as the LHS and RHS traces did not intersect.

Note that the steady-state solution flattens out to a constant $I_{\rm ss}$ value of $\sim 4\,\mu\rm A$ at high $I_{\rm bias}$. In this flat region, increasing $I_{\rm bias}$ simply causes the resistive segment to grow so that a constant $I_{\rm ss}$ can be maintained. Figure 3-15B shows this increase in resistance with increasing $I_{\rm bias}$.

Without doing a full numerical analysis to study the stability at every steady-state solution found above, we can get an idea of which states are more likely to be stable and which states are not by looking at the position of the states in I-T space as shown in Fig. 3-16. Here we have plotted for every $Z_{\rm o}$ value, the minimum $I_{\rm bias}$ for a resistive solution vs the calculated temperature at the center of the resistive segment. We see that smaller $Z_{\rm o}$ values have solutions that are closer to the superconducting boundary and are likely to be less stable as small fluctuations in the nanowire resistance could cause the system to switch into the superconducting state. Generally, the steady-state solutions move away from the superconducting boundary and deeper into the resistive region of the I-T space with increasing $I_{\rm bias}$, and $Z_{\rm o}$. This trend is consistent with experiment.

We mentioned before that the stability of the resistive segment depends on the feedback speed of the electric circuit. The feedback speed will determine how quickly the system brings itself back to the steady-state solution when it is perturbed away from equilibrium (by photon absorption for example). In Fig. 3-16, we see that for a given device inductance, a system with a smaller $Z_{\rm o}$ is not only slower in responding to these perturbations, but is also more likely to switch into the superconducting state. Due to the proximity of its state to the superconducting boundary, slight perturbations in the state could tip the state of the system into the superconducting state and therefore unlatch the device. This trend was also observed experimentally in Ref. [40].

We show in Fig. 3-17A and B experimental results from our recent paper for comparison with our calculations. A full description of the experiment can be found in the paper itself and will not be discussed here. In Fig. 3-17A we see that for a given $Z_{\rm o} = 333\,\Omega$ for instance, the nanowire stays superconducting at low bias currents where the device current is equal to the bias current. At a bias current of

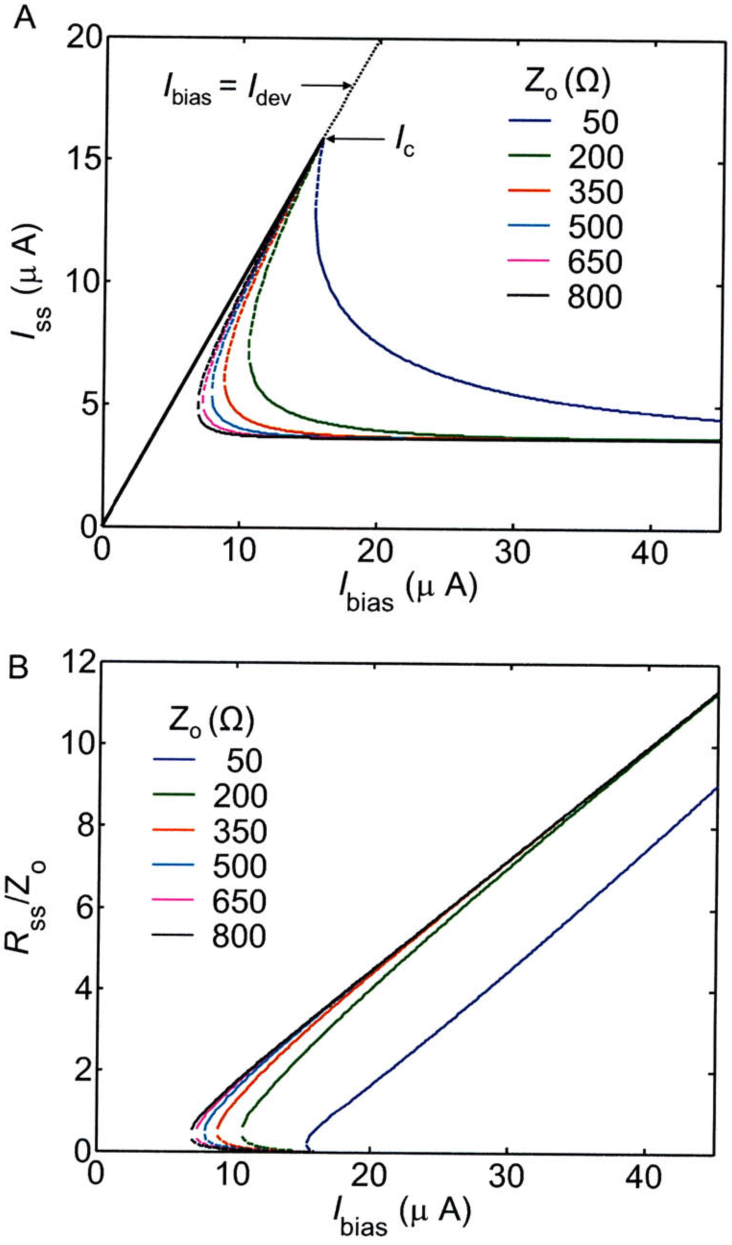

Figure 3-15: (A) Plot of calculated steady-state device current I_{ss} vs bias current I_{bias} shown as solid lines for different load resistances Z_o. (B) Plot of calculated steady-state device resistance normalized by Z_{o} vs bias current I_{bias}. The dashed lines are non-physical solutions. The solid lines show the presence of steady-state solutions. The device will definitely not latch in the range of I_{bias} where no steady-state solution exits but may latch otherwise.

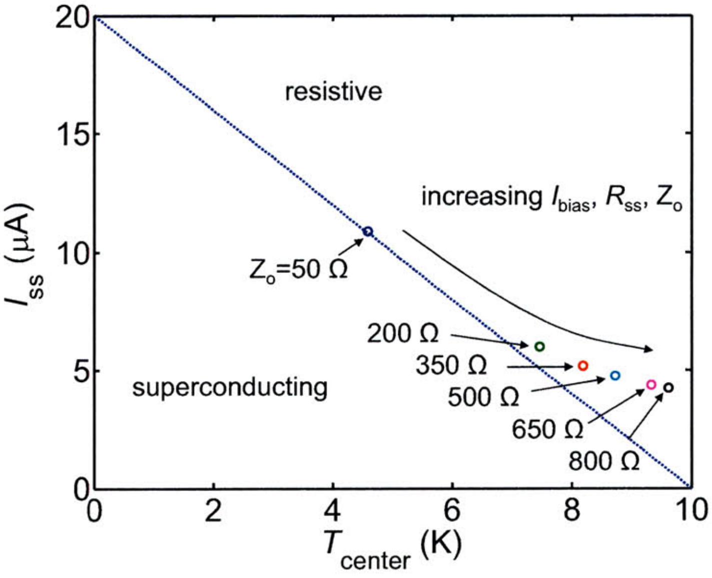

Figure 3-16: Plot of minimum I_{bias} for a given Z_{o} vs the temperature at the center of the resistive segment T_{center}. The dotted line is the critical current at a given temperature from equation 3.11 which defines the boundary between superconducting and resistive states in the $I - T$ space. Points that are closer to the superconducting state are likely to be less stable as small fluctuations in the length of the resistive segment could tip it into the superconducting state. The steady-state solutions also tend to move away from the superconducting boundary (thus becoming more stable) with increasing I_{bias} and R_{ss}.

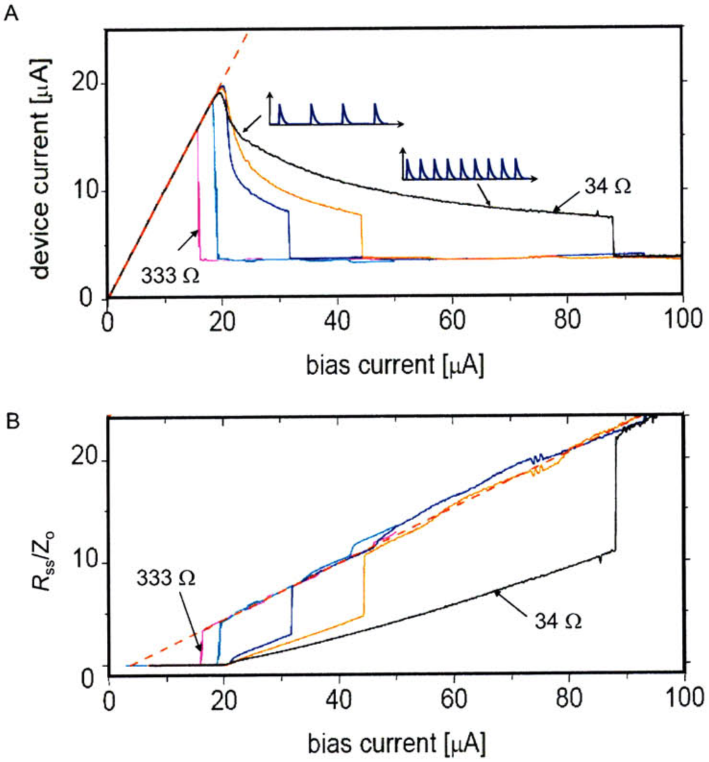

Figure 3-17: Experimental results showing steady-state device current (A) and normalized device resistance (B) vs bias current for different load resistances ranging from 34 Ω to 333 Ω.

$I_{\mathrm{latch}} \sim 18\,\mu\mathrm{A}$, the device current abruptly drops down to a constant value of $\sim 4\,\mu\mathrm{A}$ where the device stays latched. I_{latch} increases with decreasing Z_{o}.

If we compare Fig. 3-15A with the experimental results shown in Fig. 3-17A, we see that the steady-state analysis results agree well with the experimental results in several aspects. One agreement is in the flat device current regime for large bias currents. In this regime, the device resistance increases linearly with increasing bias current which maintains a constant device current. Our calculations also show that for increasing Z_{o}, the minimum bias current (for which a solution exists) decreases. This calculated minimum bias current may not be a stable solution, and experimentally, the device may not latch exactly at this minimum value but at larger bias currents I_{latch}. Nonetheless, this trend of decreasing minimum I_{bias} with increasing Z_{o} is seen as a decreasing I_{latch} with increasing Z_{o} in Fig. 3-17A.

The curved portions of I_{ss} vs I_{bias} in Fig. 3-15A were not observed experimentally as latched states. Although they look similar, the curved portions of the data in Fig. 3-17 were not steady-state solutions but were relaxation oscillations as depicted as voltage pulses in the inset of Fig. 3-17. Possibly the curved segments of the analytical plots correspond to unstable resistive states of the nanowire.

3.6 Conclusion and future work

The electro-thermal model was useful in providing an understanding of the SNSPD. It told us that Joule heating and heat dissipation account for the response of the SNSPD after a photon is absorbed. It also showed that we could speed up the SNSPD by adding a resistor in series with the nanowire. Experimental results show that a speed-up by a factor of five could be achieved for a large $15\,\mu\mathrm{m}$ by $15\,\mu\mathrm{m}$ active-area device biased through a $192\,\Omega$ resistor. However, speedup comes at the expense of device latching.

Device latching prevents proper detector operation and sets a limit to how fast we can reset the device. Electro-thermal model simulations of latching shows that a small segment of the nanowire is stabilized by negative electro-thermal feedback to stay in the resistive state.

Future efforts should be focused on improving the electro-thermal model to obtain quantitative agreement with experiments. To do this, one would need to directly measure the thermal properties of the nanowires which is a non-trivial endeavor.

More work should also be done to avoid device latching while increasing detector reset. To prevent latching while still having a short reset time, we would need to modify the thermal properties of the materials. For instance, we could reduce the thermal time constant of the nanowire by having better thermal boundary conductance with the substrate or using thinner films. However, a better thermal conductance to the substrate could be detrimental to the detection efficiency of the device. Hence, experiments with different substrates and superconducting films would be necessary.

Finally, recent progress in NbN growth has allowed us to make large-area devices with good yield. We found that the NbN films deposited at MIT Lincoln Laboratory produced higher device yields compared to films that we previously obtained from Moscow State Pedagogical University [58]. We hypothesize that these films have a lower density of defects and therefore enable large-area devices to be fabricated. As large devices are also slower, the method of adding a series resistor to reduce the reset time, as described in Section 3.4, would be invaluable.

Part II

Sub-10-nm Lithography

Chapter 4

High-Contrast Salty Development of Hydrogen Silsesquioxane

In this chapter, I will discuss a process we developed to achieve sub-5-nm-half-pitch electron-beam patterning in hydrogen silsesquioxane (HSQ) negative-tone resist. HSQ is used widely today as an electron-beam resist. Namatsu et. al. [59] first realized that HSQ has excellent properties as an electron-beam resist in 1998. However, the contrast of this negative resist was poor. Although patterning sub-10-nm wide isolated lines was not a problem [60, 61], patterning dense lines below 20-nm-pitch was not possible, although impressive demonstrations have been made [62, 63].

We found a simple solution to the problem of low contrast in HSQ by adding NaCl salt to an aqueous NaOH developer. The work of Hinsberg and Gutierrez in 1984 [64] showed that the addition of salt to an aqueous alkaline developer strongly affects the dissolution rate of novolak photoresist films. Although the salt effect is well known in photoresists, there is no agreement in the field on the underlying mechanism by which salt effects dissolution rates or the dissolution of photoresists in general. As novolak typically has high resist contrast, the effect of salt on its contrast was not investigated. Hence, although our work was inspired by the effect of salt in novolac resists, the different chemical reactions of HSQ and novolak in the developer prevents us from drawing direct parallels between the two resist systems.

4.1 Introduction

We define resolution as "the minimum-pitch (or half-pitch) structures that can be made or patterned by a lithography tool". For example, the present 32 nm node in CMOS manufacturing refers to the half-pitch of a memory cell, i.e. half the distance between memory cells in a dynamic random access memory (DRAM). In literature, resolution is commonly implied as "the smallest *isolated* structure that can be patterned by a lithography tool". This latter definition of resolution is imprecise, as one can fabricate isolated structures to as small as one wishes by controlled lateral etching of the structures (see e.g. [65]). Conversely, fabricating dense structures at the smallest dimensions is a better test of the resolution capability of a lithography tool.

There have been many impressive demonstrations of the sub-10-nm resolution capabilities of electron-beam lithography systems [66, 67, 68, 69]. However, most of the work that claim sub-10-nm resolution are for isolated or sparse structures. On the other hand, only a few groups have actually demonstrated sub-10-nm half-pitch patterning resolution. For instance, by building a new ultra-low-vacuum electron-beam system, Hiroshima et. al. demonstrated that 15-nm-pitch lines could be patterned in SiO_2 [70]. Fischbein and Drndic also recently demonstrated the fabrication of dense sub-10-nm structures using a 200 kV acceleration voltage electron-beam ablation of metals on a Si_3N_4 membrane in a transmission electron microscope [71].

HSQ was initially sold as a spin-on glass for use as a low-k dielectric in the semiconductor industry. However, in the seminal work of Namatsu et. al. [59], HSQ was found to also have excellent properties as an electron-beam resist. Namatsu et. al. demonstrated that HSQ has low line-edge roughness of 2 nm and good etch resistance. The low line edge roughness was attributed to the small molecular aggregates that form in the resist while the good etch resistance was due to the formation of SiO_2-like material during electron-beam exposure. Today, HSQ is being used widely as a negative-tone electron beam resist.

One of the main problems encountered with HSQ is its low resist contrast. Several consequences of low contrast are low patterning resolution, low process margin, loss of resist thickness, and footing between structures [72, 73]. Consequently, the fabrication of densely-packed sub-10-nm half pitch HSQ structures has not been done before. One of the most impressive results in HSQ were obtained using extremely thin resist films (10 nm) and high electron-beam acceleration voltages (100 kV) [62]. In this work, the problem of low resist contrast was circumvented by using a potassium hydroxide (KOH) developer.

Previous attepmts to improve HSQ showed that the contrast was increased by increasing developer concentration [74] and temperature [73]. These experiments were done using aqueous tetra-methyl ammonium hydroxide (TMAH) as the developer. In this chapter, we show how we increased the contrast of HSQ by adding salt (e.g. NaCl) to an alkali developer (e.g. NaOH). We came to this approach by first hypothesizing that the increased contrasts observed in Ref. [74] (from more concentrated developers) and Ref. [73] (from elevated development temperatures) were linked to increased reaction rates during resist development. Because studies on dissolution of phenolic polymers have shown that the addition of salt to an alkaline developer could also increase reaction rates [75, 76, 64], we hypothesized further that the addition of salt to an alkaline developer of HSQ may improve its contrast.

We compared HSQ contrast curves for developments in different solutions and found that the best contrast of $\sim$10 (for measurements done in a 115-nm-thick resist) was achieved by development in an aqueous mixture of 1%wt NaOH and 4%wt NaCl. This contrast value was a factor of three higher than what we measured for development in the conventional 25%wt tetramethyl ammonium hydroxide (TMAH) developer (which is the most commonly used developer for HSQ). With this result, we transformed HSQ from a low contrast resist to a resist that has sufficient contrast that the EBL resolution was no longer limited by resist performance.[1]

We demonstrated that the salty development resulted in structures with higher resolution and fidelity than development in the standard tetramethyl ammonium

---

[1] We will show in section 4.5 that the resolution was limited by the resolution of our Raith 150 tool.

hydroxide (TMAH) developer. With the standard TMAH developer, we could barely resolve 30-nm-pitch structures (see Fig. 4-10). However, with the salty developer, 9-nm-pitch nested-"L" structures and 7-nm-diameter nano-dots on a 20 nm pitch in two dimensions could be resolved. Furthermore, isolated as well as dense lines yielded with negligible loss in original resist thickness.

High-contrast and high-resolution patterning in HSQ has numerous potential applications. For instance, large-area patterning of dot structures as shown in Fig. 4-1 (a) might be used in the fabrication of high-density (~1.4 Tb/in^2) bit-patterned media. On the other hand, the boustrophredonic structure featured in Fig. 4-1 (b) might be used to make superconducting nanowire single-photon detectors with higher sensitivity to mid-IR wavelength photons. Other potential applications of this salty development include making higher resolution photo-masks, nanoimprint molds and defining quantum dots for application to classical or quantum information processing.

4.2 Resist contrast and resolution

In optical lithography, one typically uses a binary stencil or mask in which the desired pattern is defined as perfectly opaque and transparent regions. In the case of a negative resist, the goal is to transfer this pattern into a resist such that the resist is completely removed in the opaque regions and completely remaining (with perfectly vertical sidewalls) in the transparent regions. However, nature dictates that some blurring occur in the image of the mask that forms in the resist, either due to light diffraction (in an optical system) or electron scattering in the resist (in electron-beam lithography). As a result, the image is transferred into the resist as a gradual change in resist chemistry from soluble to insoluble, corresponding to the opaque-transparent transition in the mask.

Resist contrast γ is a measure of the sharpness of the transition from soluble to insoluble, as the resist chemistry is modified with increasing exposure dose. A larger γ corresponds to a higher resist contrast. Measurement of resist contrast is useful as it is an indication of how well the resist can reproduce the desired pattern, given

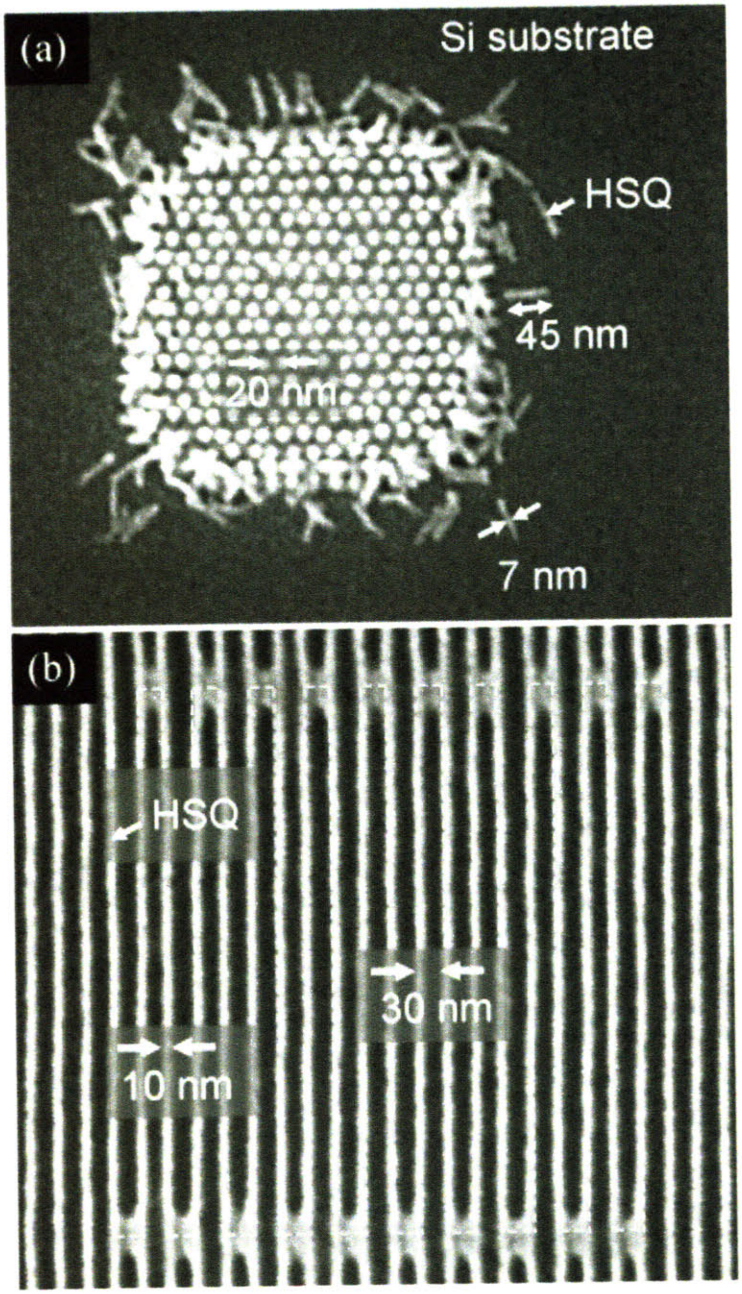

Figure 4-1: SEM images of HSQ nanostructures on Si patterned at 30 kV acceleration voltage in a Raith 150 EBL system and developed using high-contrast aqueous 1% wt NaOH and 4% wt NaCl developer. (a) HSQ nano-posts with a center-center distance of 20 nm in a hexagonal close-packed structure in 45-nm-thick resist. The aspect ratio of the structures was 6 as can be seen in the collapsed posts around the edges. (b) Boustrophedonic structure with 10-nm-wide lines on a 30-nm-pitch exposed in 45-nm-thick HSQ. The dotted lines show the deliberately connected structure.

the less-than-perfect image formed from the exposure. High contrast leads to larger process latitude, more vertical resist sidewalls, higher resolution and less footing in between lines. Resist contrast is usually measured from contrast curves which are plots of thickness of resist remaining after development vs. exposure dose, typically for large exposed areas. An ideal negative resist with infinite contrast will have a step function for its contrast curve, as shown in the red line in Fig. 4-2. However, real systems do not behave this way but exhibit a finite soluble-insoluble transition as illustrated in the green line in Fig. 4-2.

Contrast curves allow one to map a given exposure dose profile to an approximate resist profile. This mapping is based on the assumption that the resist development behavior measured in large exposed areas can be applied directly to dose modulations over small dimensions. This assumption is clearly invalid in situations where the resist development becomes diffusion limited in tightly confined resist trenches. Therefore a steep contrast curve is should be taken only as an indication of high contrast performance at small dimensions, though one still needs to perform a resolution check to verify (c.f. Section 4.4). Nonetheless, with all other things being equal, this simple model will show that a higher contrast resist results in a more vertical resist sidewall than a lower contrast resist.

The contrast curve, when presented as resist thickness remaining vs. exposure dose, is dependent on the actual experimental setup and is not a universal measure of the resist performance. Hence, we need to specify the parameters of the experiment, such as the original resist thickness, type of substrate, exposure beam energy (or electron acceleration voltage), and development conditions. A possibly more elegant method of presenting a contrast curve is as a function of dissolution rate vs. energy deposited per unit volume. However, the actual energy deposited per unit volume of resist is not directly measurable and dissolution rates may change with development time. As a result, most contrast curves are still presented as resist thickness remaining vs. exposure dose.

The connection between resist contrast and resolution is discussed next. Consider an exposure of 14-nm-pitch lines. Due to the scattering of electrons in the resist and

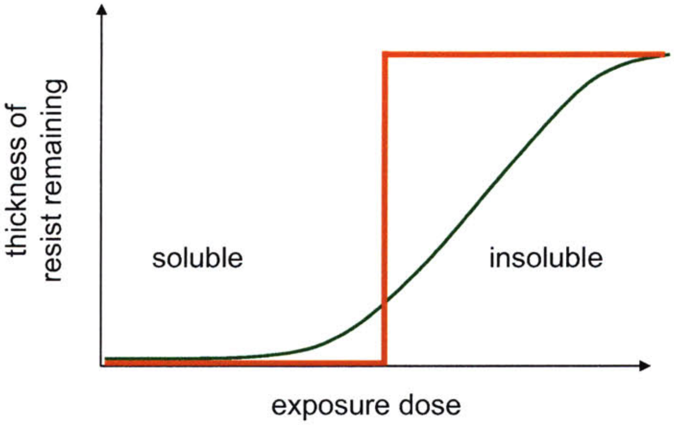

Figure 4-2: Contrast curves for an idealized negative resist (red) and a realistic resist (blue)

substrate, the exposure profile of the electron beam is broadened. As a result, when we expose the dense 14-nm-pitch structures the resultant dose profile in the resist looks like small ripples atop a larger background dose, as shown in the first column of Fig. 4-3. If we had a resist with infinite contrast, we could "clip" the dose right at the dashed lines of the dose profile and obtain a resist profile consisting of stripes with perfectly straight sidewalls and flat tops. However, let us consider two realistic resist contrasts instead, as shown as red and blue lines in the contrast curves in the second column of Fig. 4-3. The blue curve corresponds to a higher contrast process compared to the red curve. If we naïvely treat the resist development process mathematically as passing the dose profile through a transfer function (i.e. the contrast curve), we then obtain the resist profiles as shown in the right column in Fig. 4-3. We see that the 14-nm-pitch lines can be resolved in both high- and low-contrast developments. However in the low contrast development, much of the original resist thickness has been lost in the developer, thus leading to a "lower fidelity" structure. On the other hand, the higher-contrast developer results in less resist loss and thus better structures for use in subsequent pattern transfer steps.

Both contrast curves in the example above were obtained from actual measurements. The low contrast was for development in NaOH alone while the high contrast was for development in NaOH with NaCl. In the following section we will describe the experiments conducted to compare contrast curves of HSQ for different developers.

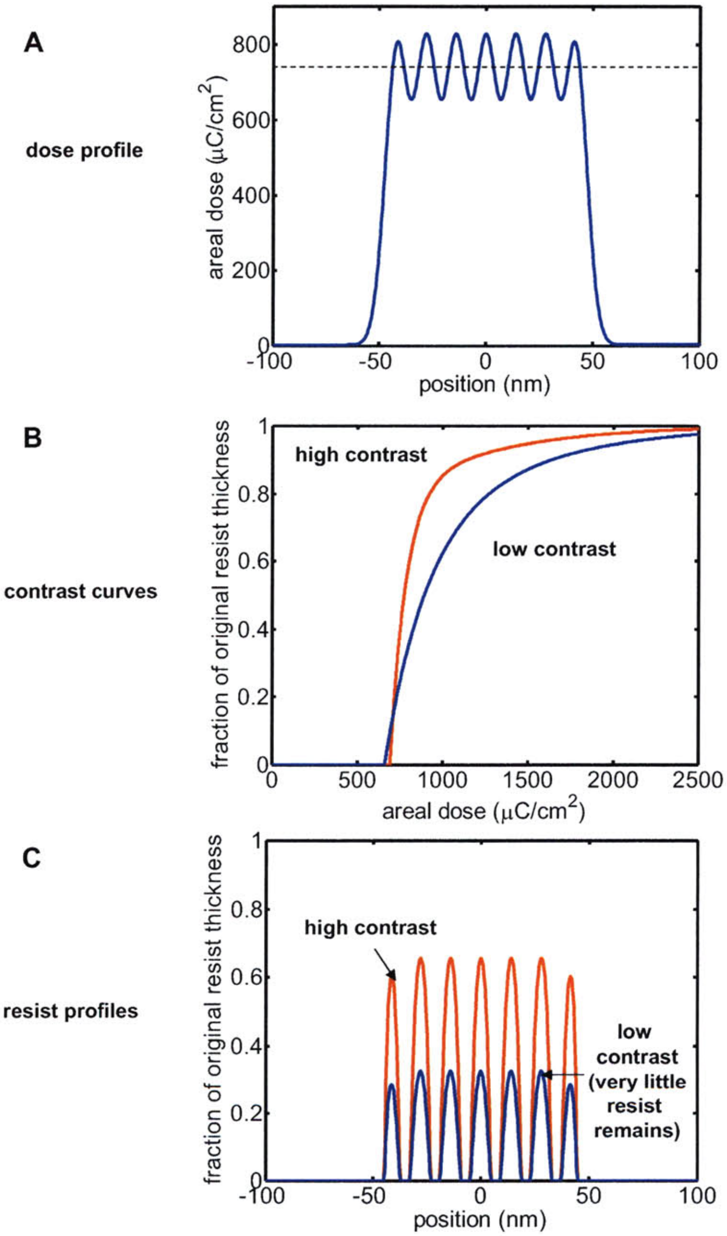

Figure 4-3: Calculations showing the resolution performances of two realistic resists with different contrasts. If we treat the contrast curves (B) as transfer functions for the dose profile in the resist (A), we can obtain the resultant resist profiles (C). In this example, both low and high contrast resists can resolve the 14-nm-pitch pattern but the lower contrast resist has lost most of its thickness thus making it less practical for subsequent pattern transfer processes.

4.3 Measuring Contrast

In literature, contrast curves are typically measured to roughly estimate the contrast performance of a resist. However, if done carefully, contrast curve measurements can also yield reproducible and accurate results. Thus, we used contrast-curve comparisons to evaluate the performances of different developer mixtures.

4.3.1 Experiment

Contrast curves were obtained by the following procedure: we first spin-coated 115 nm of HSQ (formulated as product XR-1541 6% solids in methyl iso-butyl ketone MIBK from Dow Corning) onto a Si wafer. To avoid thermally-induced contrast reduction [74], we did not bake the resist-coated wafer. We used the Raith 150 EBL system to expose a dose-matrix of 10 μm by 80 μm rectangles spanning a range of doses from 600 to 2500 $\mu C/cm^2$ at 30 kV acceleration voltage. To speed up the writes while maintaining a well-focussed and stigmated beam, we used the second to largest aperture i.e. the 60 μm aperture to get a high beam current of ~1.22 nA. The step size was set to 10 nm. Several sets of dose arrays were exposed in the same run on the same wafer to reduce variations between separate experimental runs.

We then cleaved the Si wafer to separate out different dose-array sets and developed each set in different developer solutions. First, a pure alkali developer solution was made, from which developer mixtures with different salt concentrations were derived. For instance, a pure alkali solution of 1% wt NaOH was made by dissolving 5 g of solid NaOH pellets in 500 ml of de-ionized water. This original solution was then poured into smaller containers to which different amounts of NaCl salt were added. We mixed solutions with different NaCl concentrations of 0%, 1%, 2% and 4% wt with the same 1% wt NaOH concentration. Maintaining a constant NaOH concentration allowed us to study the effect of salt while keeping all other things constant.

Developments were done by immersing the sample in the developer for 4 mins at 24°C. We maintained a constant temperature for all developments to avoid temperature dependent effects on the contrast. Finally, the thickness of each rectangle in the

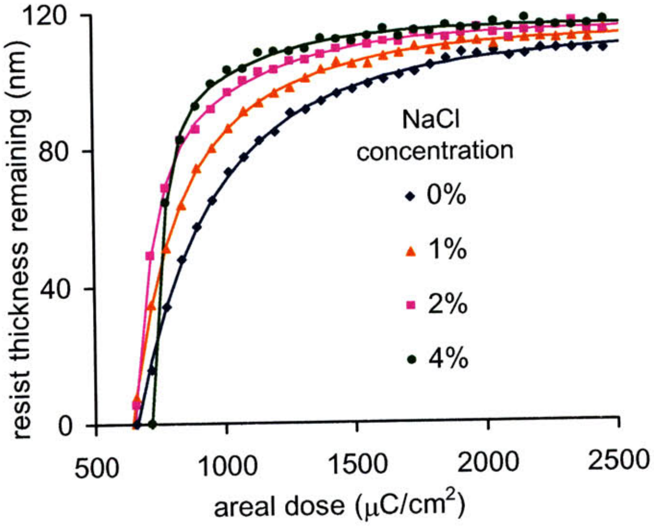

Figure 4-4: Plot of remaining HSQ thickness vs. area electron exposure dose for varying concentrations of NaCl in aqueous 1% wt NaOH developer. Filled markers are data points while solid lines are fitting curves of exponential functions.

dose arrays was measured using the Dektak 3 surface profilometer in the Nanostructures Laboratory.

Contrast measurements for development in aqueous 1% wt NaOH with varying amounts of NaCl salt is plotted in Fig. 4-4. Note that unlike the contrast enhancements achieved by increasing base concentration and development temperature, increasing the concentration of salt did not result in a significant decrease in sensitivity, i.e. the onset doses (the maximum dose at which no resist remains), were ~650 μC/cm^2 in all cases. However, the slope of the curves at the onset dose increased with increasing salt concentration, leading to the conclusion that the addition of salt to the developer increased resist contrast. Note that the effect of salt was to increase the selectivity of the development process such that doses > 1000 μC/cm^2 experienced minimal resist loss while doses < 700 μC/cm^2 were more completely removed.

4.3.2 Calculating Contrast Values

To get a consistent and non-biased measure of the contrast, we used a least-square error method to fit the measured resist-thickness remaining (RTR) to the following phenomenological function,

$$RTR = \frac{T}{1+\eta}[(1 - e^{-(D-D_0)/A}) + \eta(1 - e^{-(D-D_0)/B})] \tag{4.1}$$

where T is the original resist thickness, D is the electron areal dose, D_0 is the areal dose at the onset of incomplete development and A, B and η are fitting parameters. This phenomenological expression, which although did not have any physical meaning, was found to provide a good fit to the data over the entire dose range above D_0. We then extracted contrast values by finding the slope of a straight line connecting the point of zero resist thickness to the point of 75% of original resist thickness of the fitted curve on a semi-log plot. In symbolic form, the contrast value γ was

$$\gamma = \frac{0.75}{log_{10}(D_{0.75}/D_0)} \tag{4.2}$$

where $D_{0.75}$ was the areal dose at 75% of original resist thickness.

4.3.3 Effects of Different Alkalis and Salts

In addition to the NaOH-NaCl alkali-salt pair, we also investigated other alkali-salt pairs. This experiment studied the effect of different anions and cations on the contrast-enhancement effect of salt. We always used alkali-salt pairs of the same cation to maintain the pH of the developer. The following alkali-salt pairs were studied: (1) NaOH - NaF; (2) NaOH - NaCl; (3) NaOH - NaBr; (4) NaOH - NaI; (5) KOH - KCl; and (6) TMAH - TMACl. For every alkali-salt combination, a set of contrast curves were obtained using the same procedure as discussed above. For these experiments, the concentration of KOH was 0.4% wt (0.07 N), concentration of NaOH was 1% wt (0.25 N) and concentration of TMAH was 2.38% wt (0.26 N).

Figure 4-5 is a plot of contrast versus concentration of salt expressed in terms of normality for a set of different alkali-salt pairs. Contrast enhancement with increasing salt concentration was observed for all alkali-salt pairs except for KOH-KCl. The alkali-salt pair consisting of NaOH-NaCl exhibited the highest contrast enhancement.

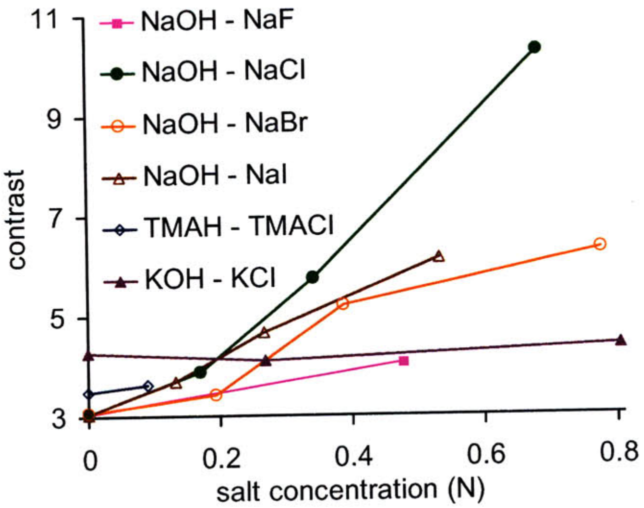

Figure 4-5: Plot of contrast versus salt concentration expressed in normality (N). This plot shows the dependence of contrast enhancement on different cationic/anionic species. The highest contrast improvement was obtained for the NaOH - NaCl alkali-salt pair.

Furthermore, changing the anion from Cl to F, Br and I, reduced the observed enhancement. The contrast values for NaOH-NaCl did not continue to increase beyond a salt concentration of 4%.

Figure 4-6 is a plot of contrast curves corresponding to the best contrast values of Fig. 3 for development in 1% wt NaOH with different sodium halides. Interestingly, the contrast curves for F, Br and I anions lie almost on the same curve above 700 μC/cm2 but that for Cl is significantly different. The data shows that contrast enhancement is highly dependent on the type of cation and anion.

4.3.4 Effect of different development time

The contrast enhancement effect of NaCl in NaOH was also observed when we repeated the above experiments with different development durations. Figure 4-7 is a plot of thickness remaining versus dose for two different development durations. In the case of development without salt, increasing the development duration from 2 to 10 minutes did not result in any change in the contrast curve. On the other hand, for development with salt, increasing the development duration further increased the

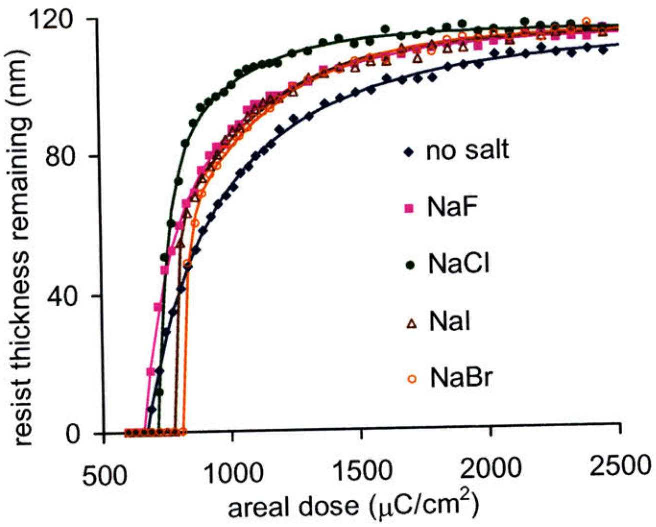

Figure 4-6: Contrast curves corresponding to the highest measured contrasts for different sodium salts in 1% wt NaOH. While similar curves were obtained for NaF, NaBr and NaI above 700 μC/cm^2, the curve for NaCl was significantly different and had a much higher contrast value.

contrast at the expense of a higher onset dose. This result suggested that the addition of salt resulted in increasing contrast enhancement with increasing development time.

Furthermore, the almost identical curves at 2 min and 10 min for the non-salty developer shows that the development process was self-limiting, i.e. development was already complete at 2 mins. However, when HSQ was developed in the salty developer, extra development, for doses around the onset dose, continued to occur after the first 2 mins.

4.3.5 Comparison with "Standard" Developer

The developer for HSQ frequently reported in literature is CD26 which is an aqueous solution of tetramethyl ammonium hydroxide (TMAH) at 0.26 N concentration. Figure 4-8 shows the contrast curve comparison between CD26 and the salty developer. When 2% wt tetramethyl ammonium chloride salt (TMACl) was added to CD26, the contrast curve shifted to the right, indicating a decrease in sensitivity accompanied by a slight increase in contrast as shown in Fig. 4-5. CD26 is 3 times more sensitive

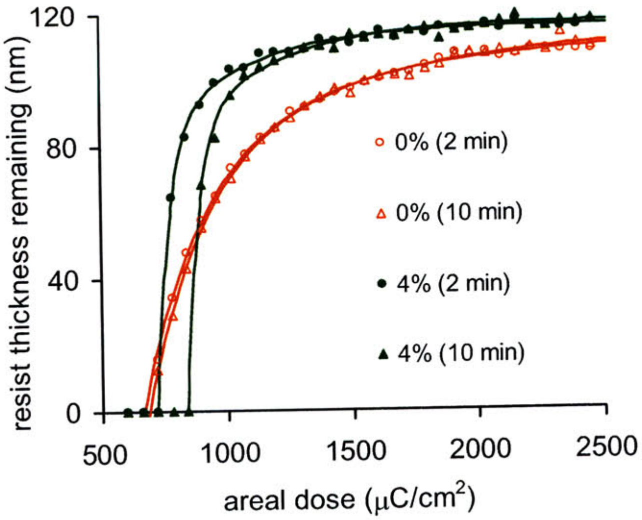

Figure 4-7: Plots of thickness remaining versus exposure dose for development of HSQ in 1% wt NaOH with two different salt concentrations and two different development times. A longer development time further improved the contrast for the salty developer, but did not affect the contrast when no salt was added.

than the salty developer.

There are several consequences of lower sensitivity. First, lower sensitivity requires higher exposure doses, and for the same beam current, requires a longer exposure time. This will not be a problem for research purposes but is a major concern in manufacturing. Secondly, higher exposure doses result in a higher degree of cross-linking in the resist and could slightly improve the structural integrity of the patterns. We have seen in our studies of shrinkage and etch resistance of HSQ [77] that the exposures need to be above ~1 mC/cm^2 to cause significant changes in the material properties.

4.4 Resolution Tests

We clearly see from Fig. 4-5 that the 1% wt NaOH with 4% wt NaCl would work best as a high contrast, high resolution developer at small dimensions. To verify this prediction, we performed resolution tests to compare the performance of this salty developer to other developers. Comparison was made with the "standard" TMAH

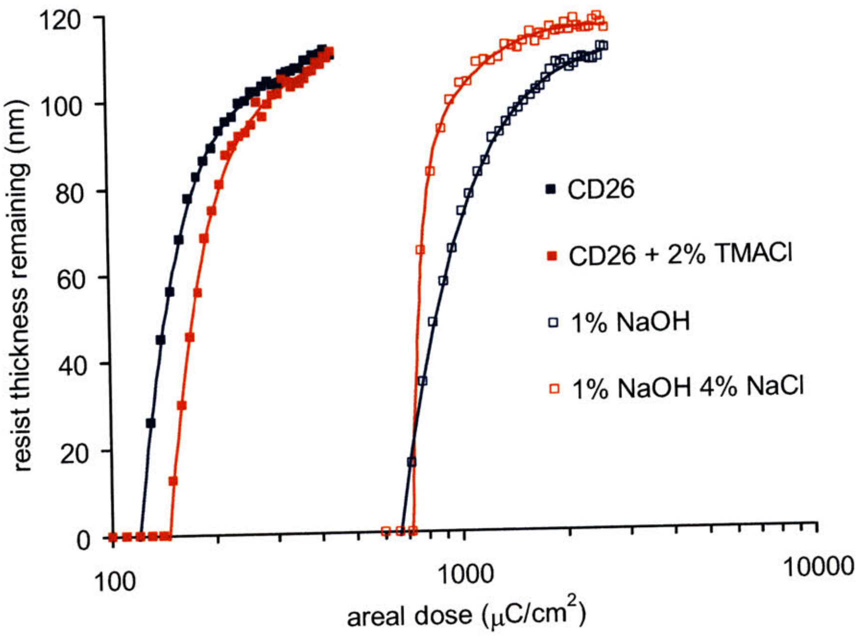

Figure 4-8: Contrast curves for standard CD26 developer and NaOH, both with and without added salts. First, notice that the NaOH developer was more aggressive than CD26 in removing/dissolving resist exposed to lower doses. Hence the sensitivity of HSQ when used with the salty developer is a factor of ~3 lower than when used with CD26. In the case of CD26, which is 0.26 N TMAH, the addition of TMACl salt resulted in a reduction in sensitivity with little change in contrast.

and the 1% wt NaOH without salt developers.

4.4.1 Comparison with low contrast developers

We studied the effect of salty development on nanostructure fabrication. We tested the highest resolution we could achieve by exposing gratings and nested-"L" test patterns in a 45 nm thick layer of HSQ on Si using a Raith 150 EBL system at 30 kV acceleration voltage, 120 pA beam current and single-pixel exposures for each line. The exposure line dose for these structures was 1 nC/cm. The samples were developed in three different developers: (1) 25% wt TMAH, (2) 1% wt NaOH without salt, and (3) 1% wt NaOH with 4% wt NaCl. Developments were all done at 24°C for 4 minutes.

Figure 4-9 shows scanning-electron micrograph (SEM) images of 16-nm-pitch nested-"L" structures developed using these three developers. Note that observing the difference in resolution between developers may require close attention. The nanostructures obtained from salty development were of higher fidelity than the corresponding structures developed in NaOH without salt or TMAH. For instance, the isolated line segments of the nested-"L" structures did not yield in Fig. 4-9B or C but yielded in D. We observe that the resolution was poor for development in TMAH. As shown in Fig. 4-9(b), the nested "L" structures at 16-nm pitch developed in TMAH were not resolved at all. Note that although the 1% wt NaOH without salt had a lower γ value than the 25% TMAH developer, the resolution tests indicate that NaOH was a better developer than TMAH. This result suggests that diffusion effects at the nano-scale, which were not present in the contrast curve measurements, may be playing a significant role in resist development. We speculate that the tetramethyl ammonium ions, with their larger size than the Na^+ ions, may diffuse more slowly and hinder development.

A clearer comparison between the salty developer and 25% TMAH developer is made in Fig. 4-10. In this comparison, we see that at 30-nm-pitch, there was no observable footing in between the lines for the salty development. Furthermore, the sparse lines at the bottom of the right image yielded, although they have fallen over.

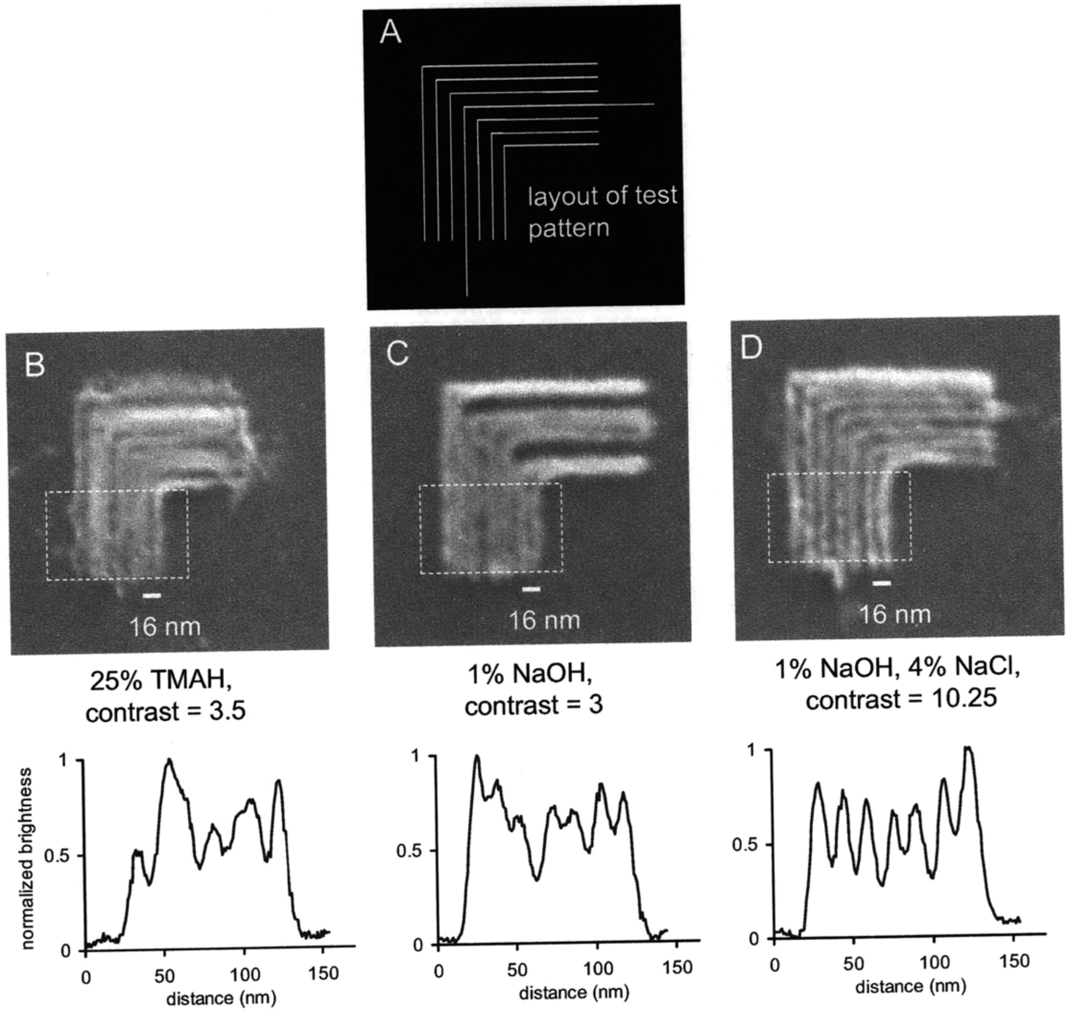

25% TMAH, contrast = 3.5

1% NaOH, contrast = 3

1% NaOH, 4% NaCl, contrast = 10.25

Figure 4-9: 16-nm-pitch nested-L structures. (A) Layout of dense and isolated lines forming the nested-L test structure. Exposure was done in 45-nm-thick HSQ at 30 kV acceleration voltage in a Raith 150 EBL system using single-pass line exposures for each line.Development was done in solutions of (B) 25% wt TMAH, (C) 1% wt NaOH without salt, and (D) 1% wt NaOH with 4% wt NaCl. Both dense and isolated lines yielded only in (D). Plots of normalized image brightness vs. distance, at the bottom of the SEMs, were obtained by averaging the brightness values of the corresponding SEM image along the length of the lines within the dashed rectangles shown in the SEMs. These plots provide a quantitative view of the resolution of the structures. We see that in (D), all seven lihes in the nested-"L" structure could be clearly resolved as well-defined peaks in the plot.

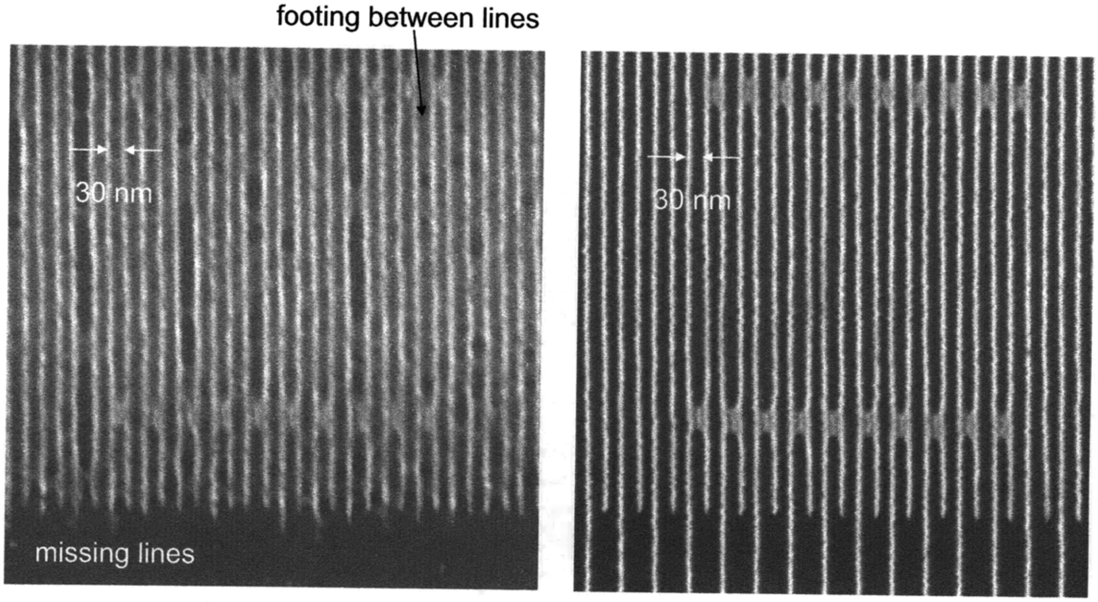

development in 25% TMAH

development in 1% NaOH + 4% NaCl

Figure 4-10: SEM of 30-nm-pitch grating structures. (Left) Resist developed in 25% TMAH. (Right) Resist developed in 1% wt NaOH with 4% wt NaCl. Notice that at the exposure dose used, the sparse line structures at the bottom of the left image were completely developed away but the regions between the lines were still not cleared out. This comparison shows that with the 25% TMAH developer, there was no process window that would yield both dense lines and sparse lines simulteneously at the 30-nm-pitch.

The width of these lines on their sides correspond to ~35 nm of resist remaining of the 45 nm original thickness. On the other hand, the 25% TMAH development resulted in footing between the lines, even when the exposure dose was low enough that the sparse lines were completely developed away and no longer yielded.

In another experiment, we used a thinner resist film, this time 35-nm thick, and exposed nested-"L" structures with longer segments for the purpose of comparison between developments in 1% wt NaOH with and without salt. As shown in Fig. 4-11, nested-"L" structures with a line-width of 7 nm in a pitch of 14 nm could be resolved using both developers. The difference, however, was that the isolated line structure was again missing for low-contrast development while both isolated and dense lines yielded for the high-contrast development. The isolated line in Fig. 4-11B had collapsed on its side. Measurement of the width of this collapsed structure gave us its height (remaining resist thickness) of $\sim 30\,\text{nm}$, which was close to the original resist thickness. Due to their higher aspect-ratio, the structures in Fig. 4-11B tended to collapse or stick together more readily than the corresponding structures in Fig. 4-11A. We can conclude here that a high-contrast development does indirectly lead to higher resolution, as the resultant resist structures are thicker/taller and therefore are more suitable for subsequent pattern transfer steps (e.g by reactive-ion etching).

4.5 Resolution Limit: Comparison between Raith 150 and Raith 150^{TWO}

With our best efforts, the resolution test structures (consisting of nested-"L"s) patterned in a Raith 150 electron-beam lithography EBL tool at MIT had a pitch of 12 nm. This result was achieved by exposure of a 20-nm-thick layer of HSQ negative-tone resist followed by a high-contrast salty development process [39]. Our attempts to improve the patterning resolution by modifying the development process were not successful. We tried developments at elevated temperatures [73], higher developer concentrations [74] and with an additional dilute hydrofluoric acid etch between salty development processes (process developed by Prof. Ki-Bum Kim et. al. from Seoul National University). These techniques have been shown to improve resist contrast and resolution by other groups, when used with TMAH developer solutions. However, improving the resist contrast beyond that achieved by the salty development process has not shown any enhancement in patterning resolution.

These experiments suggested that the resist contrast was not the limiting factor in achieving higher resolution. Instead, the resolution could be limited by (1) forward scattering range of high-energy incident, and low-energy secondary electrons in the resist, (2) finite spot size of the electron beam, (3) electrical noise and vibrations causing unwanted deflections in the beam during exposure, and/or (4) exposure shot noise.

To show that the resolution was tool-limited and not resist-limited, we patterned

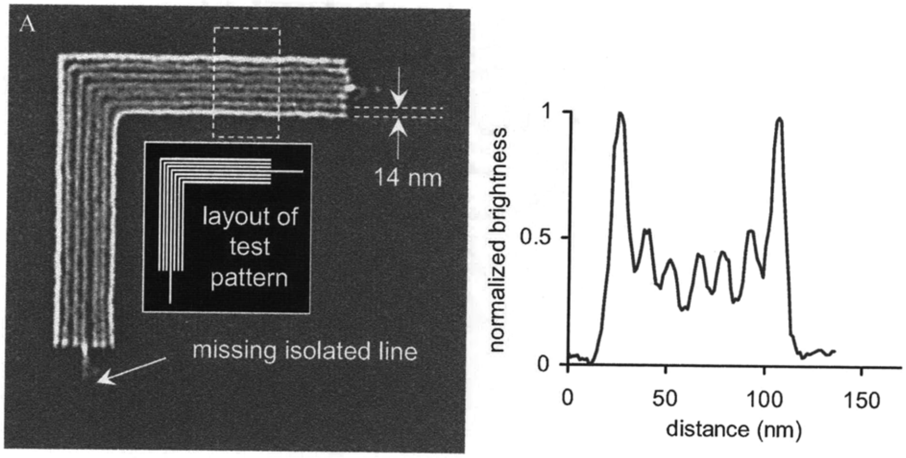

1% NaOH without salt

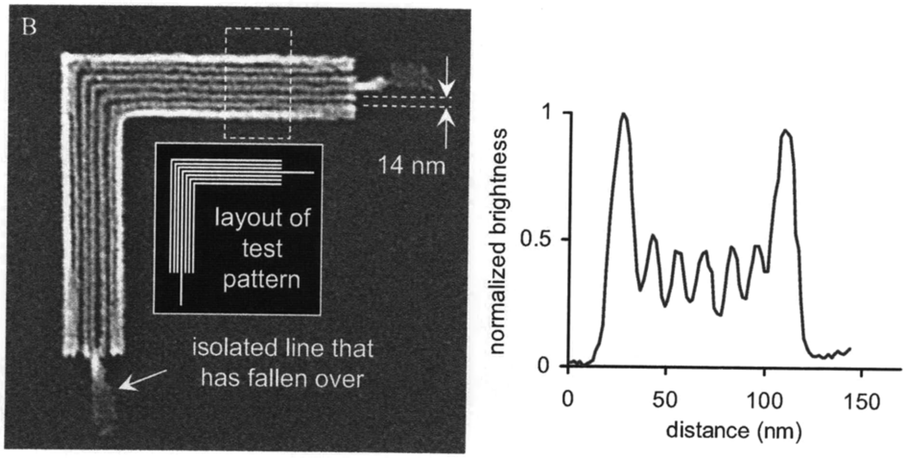

1% NaOH + 4% NaCl

Figure 4-11: SEM of 7-nm-half-pitch nested-L structures exposed in 35-nm-thick HSQ. Development was done in (A) 1% wt NaOH without salt, and (B) 1% wt NaOH with 4% wt NaCl. Both dense and isolated lines yielded in (B) while isolated lines were missing in (A). The isolated line in (B) has fallen over. The corresponding averaged brightness plots, shown to the right of the SEMs, were obtained from the dashed rectangles. These plots show that the 14-nm-pitch structures were resolved in both developers. However, the missing isolated line indicated that the addition of salt into the developer resulted in less resist loss during development.

identical resolution test structures in two EBL machines, i.e. a Raith 150^{TWO}, at Raith's headquarters in Germany, and a Raith 150 at MIT. Although these systems have very similar Zeiss columns and electron-optics, slight variations (e.g. in the gun system) may result in different beam spot sizes. In addition, the Raith 150^{TWO} has better noise isolation and stage design compared to the Raith 150. There are also other improvements that the Raith 150^{TWO} has over the Raith 150 such as better thermal stability, and the ability to translate the stage while exposing. However, beam spot size and noise isolation probably have the most effect on patterning resolution.

We successfully transferred our salty-development process to Raith and thus performed the same fabrication processes at both locations (MIT and Raith). In both experiments, the resist thickness (of 20 nm), exposure parameters and development processes were the same . Hence, if we saw any differences in the patterning resolution in these machines it would likely be due to differences in the two EBL systems.

Careful comparison between the results obtained at MIT with those achieved at Raith Germany showed that the patterning resolution in the Raith 150^{TWO} was marginally better than in the Raith 150. Using the Raith 150^{TWO}, we were able to pattern nested-"L" structures down to 9-nm pitch. The difference in minimum resolvable pitch was ~2 nm when compared to the best results achieved at MIT.

Figures 4-12 to 4-14 show one to one comparisons between the Raith 150^{TWO} and Raith 150. These patterns were exposed using a 30 kV acceleration voltage and a 20 m aperture size. They were developed at ~24 deg C in 1% wt NaOH + 4% wt NaCl aqueous developer for 4 mins followed by a DI rinse and blowdry. See captions for explanations.

4.5.1 Patterning at different acceleration voltages

Bryan Cord has shown in his experiments that the EBL resolution for the Raith 150 did not change when the acceleration voltage was varied from 10 kV to 30 kV. Here, we verify this observation in the Raith 150^{TWO} by doing exposures in 10-nm-thick resist at 10 kV. Unfortunately, due to poor beam focus and stigmation adjustment at 30 kV, we do not have a good one-to-one comparison for 10 and 30 kV exposures in

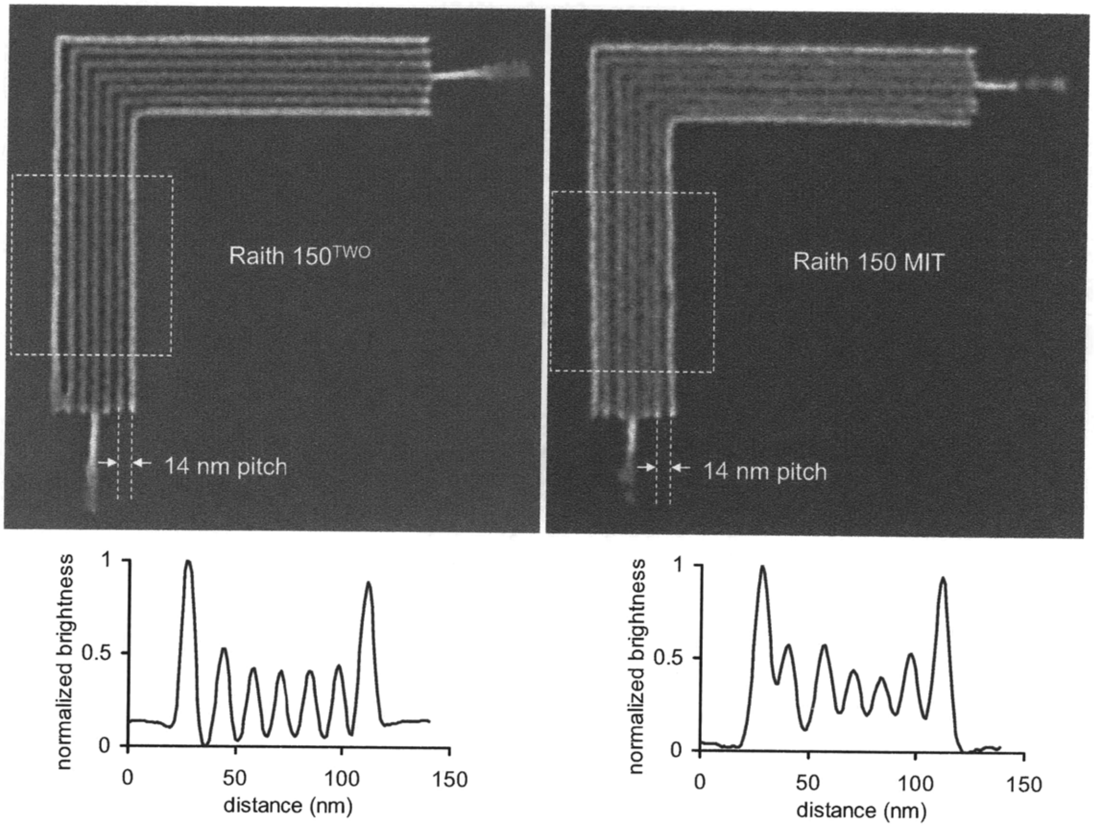

Figure 4-12: SEM of 14 nm pitch nested-“L” structures. The quality of the lines patterned in the Raith 150$^{\mathrm{TWO}}$ was better than the lines patterned in the Raith 150. Gaps between the lines also appear more cleared out. The plots of normalized brightness vs distance at the bottom of both images were obtained using ImageJ by averaging the brightness values of the SEM image along the length of the lines within the dashed rectangles shown. This plots provide a quantitative view of the resolution of the structures. For instance, we immediately see that in the Raith 150$^{\mathrm{TWO}}$ patterned structure, all 7 lines in the nested-“L” structure could be clearly resolved as separate peaks in the plot. The same plot for the right image has only 5 peaks. We could define the resolution limit as the minimum pitch at which this plot shows all 7 peaks.

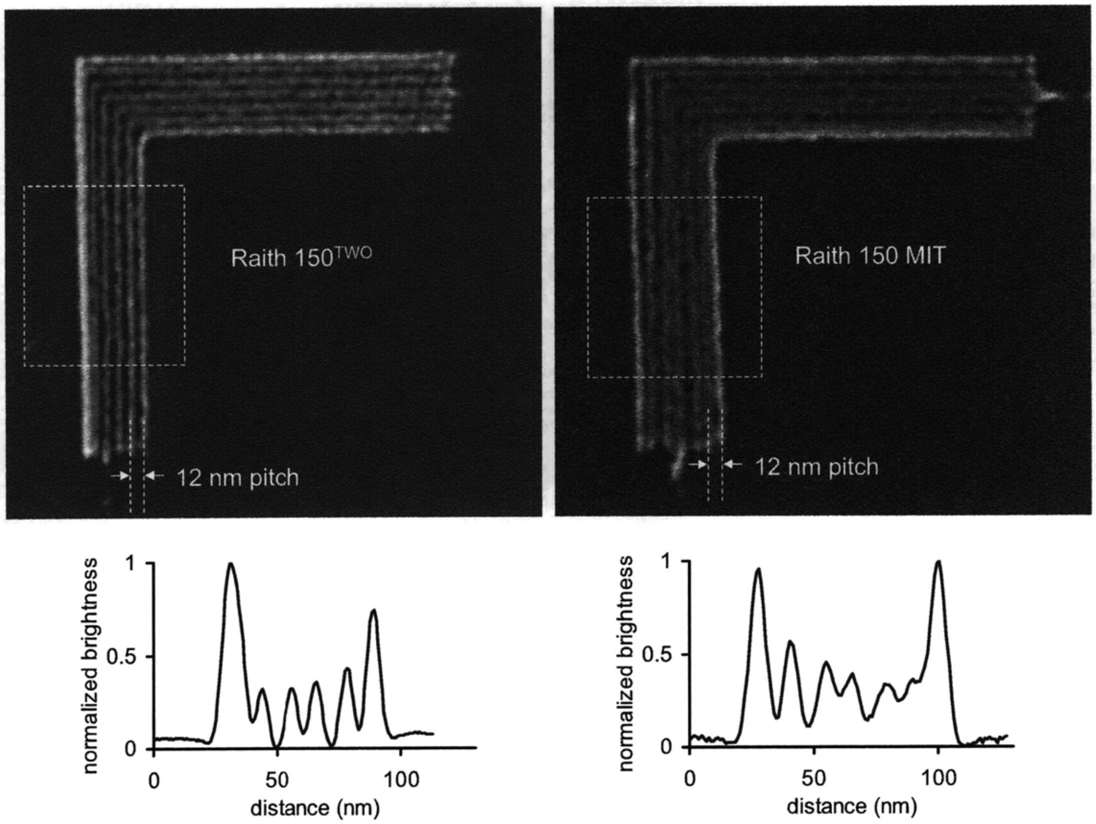

Figure 4-13: SEM of 12 nm pitch nested-"L" structures in 20 nm resist. In the left image, pattern placement problems, as mentioned above, caused the left-most line to be offset to the right of its nominal position. However, we see that in the image on the left, the spaces between the lines appear darker, indicating that the resist has been cleared out in these 6 nm gaps.

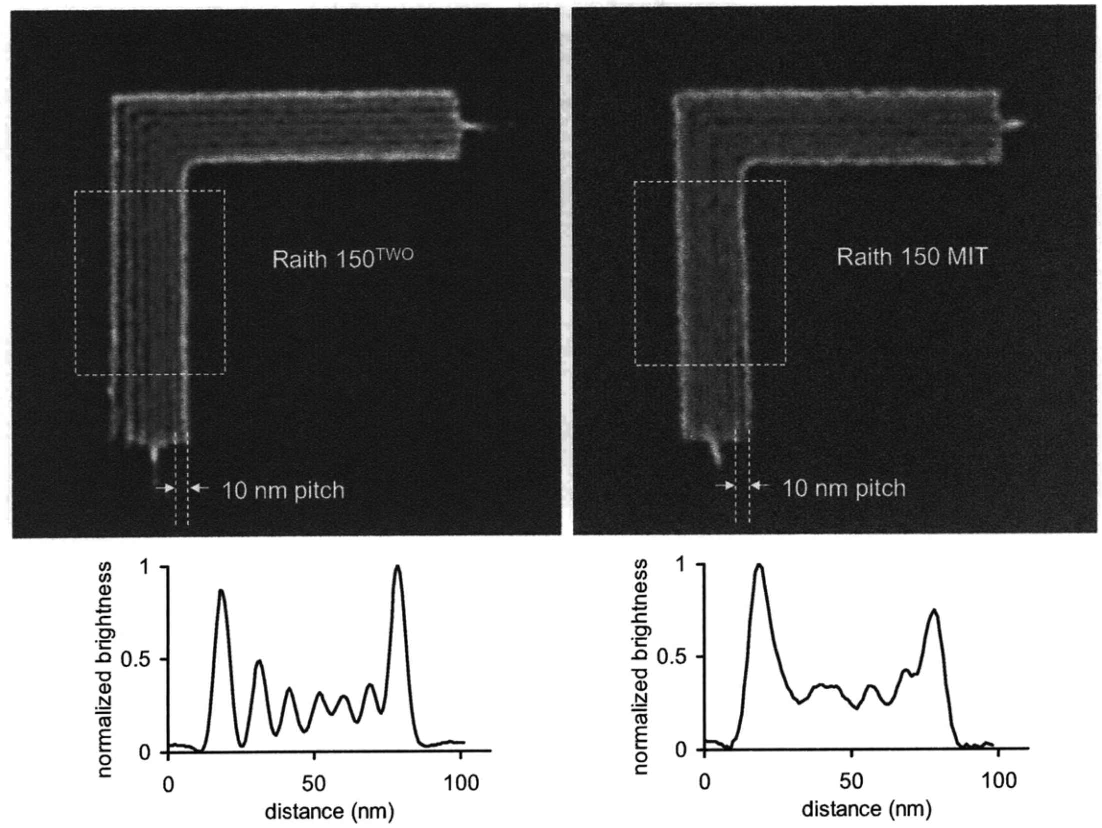

Figure 4-14: SEM of 10 nm pitch nested-“L” structures in 20-nm-thick resist. Qualitative evaluation of the SEM images show that the lines in the left image were more clearly resolved compared to the lines in the right image. Notes: There were noticeable pattern placement problems in the exposure on the Raith 150$^{\mathrm{TWO}}$. First, the settling time of 2 ms was not sufficient, causing the vertical segment of the left-most line of the nested-“L” to have an offset to the left. This was an effect of the beam blanker turning off before the magnetic deflection coils had settled into a steady state.

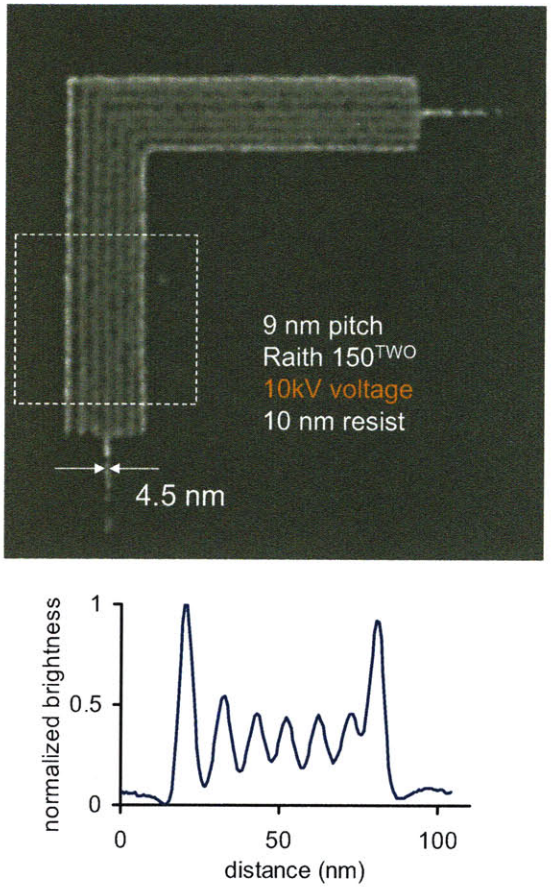

Figure 4-15: SEM of 9 nm pitch nested-"L" structures patterned 10 kV in 10 nm resist. The ability to pattern 9 nm pitch patterns even at 10 kV was a good indication that electron column maintained a constant beam spot size at 10 and 30 kV acceleration voltages.

10-nm-thick resist. We show in Fig. 4-15 9-nm-pitch patterns exposed at 30 kV in 10-nm-thick resist.

4.6 HSQ exposure and development mechanism

In this section, we provide a hypothesis of how HSQ works. Although the detailed chemical processes are unknown, this hypothesis would be a good starting point for future investigations into actual mechanisms.

This lack of understanding is not unique to HSQ systems but is true of photoresist systems too. The development mechanism of photoresists in general is not well understood although the multi-billion dollar semiconductor industry relies heavily on it. Some of the best models for novolac photoresist development are the critical ionization model by Tsiartas et. al. [75] and the percolation model by Reiser et. al.[78, 79, 80]. Although both models predict different aspects of photoresist development well, they are based on totally different physical effects. Hence there is no agreement on how photoresists actually develop.

4.6.1 Exposure mechanism

HSQ has a chemical formula of $H_8Si_8O_{12}$ with a cage structure, as shown in Fig. 4-16. This cage structure is unstable due to the strained bond angles of Si and O and weak Si-H bonds. During EBL exposure, the high energy electrons break the Si-H and Si-O-Si bonds of the cage and fragments this cage structure. New bonds are formed between nearby fragments resulting in stronger unstrained Si-O-Si bonds called network bonds[18, 59]. It is likely that hydrogen gas is released during EBL exposure as Si-H bonds are broken.

This cross-linking mechanism can be seen in fourier-transform infrared (FTIR) spectra measurements of HSQ. Fig. 4-16 shows FTIR spectra of HSQ exposed at different doses. In the FTIR spectra the breaking of Si-H and cage Si-O bonds is seen as decreasing peaks corresponding to these bonds. On the other hand, we see increasing peaks for the stronger network Si-O-Si bonds that form. With large EBL exposure doses ($> 100\,\mathrm{mC/cm^2}$ at $30\,\mathrm{kV}$ acceleration voltage), the resist loses all its H atoms and forms silicon oxide [77].

At lower exposure doses, molecules of partially cross-linked HSQ form. The random nature of cross-linking results in a distribution of sizes and shapes in these molecules. For simplicity, let us call these partially cross-linked HSQ molecules, x-HSQ. An example of an irregularly shaped x-HSQ molecule is shown schematically in Fig. 4-16. On average, lightly dosed HSQ will consist of smaller x-HSQ molecules than highly dosed HSQ.

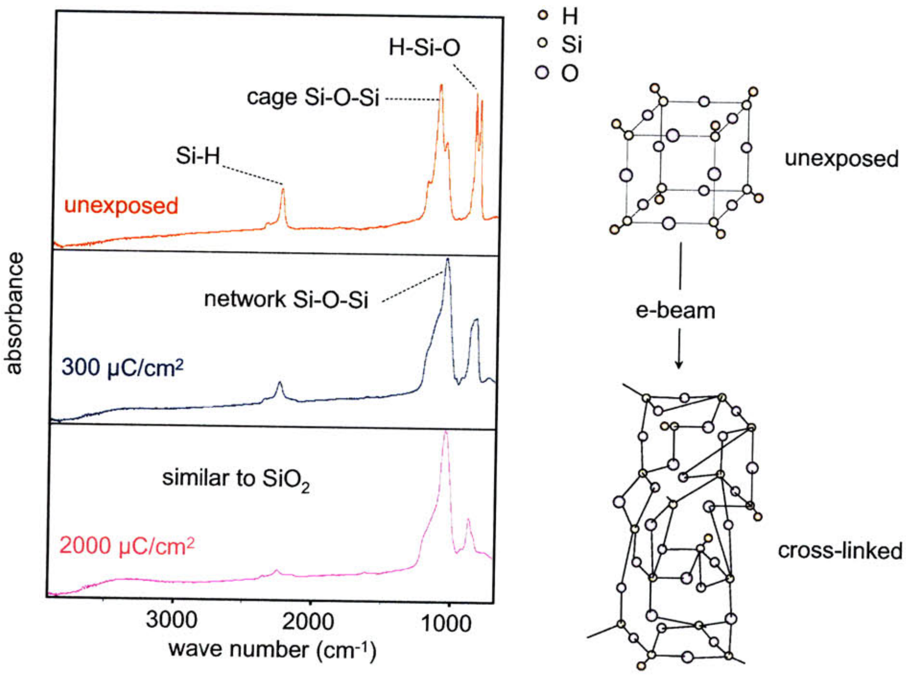

Figure 4-16: Fourier transform infrared (FTIR) spectra of HSQ at different exposure doses. Unexposed HSQ molecules consists of cage structures with a Si-H functional groups at the corners of the molecule. EBL exposure breaks Si-H and cage Si-O bonds while forming network Si-O-Si bonds. As seen in the FTIR data, the Si-H, and cage Si-O bond peaks decrease in intensity while the network Si-O-Si bond peak increases in intensity. As drawn schematically, cross-linked HSQ (x-HSQ) contains a small number if Si-H bonds, some Si· dangling bonds and lots of randomly oriented Si-O-Si network bonds.

4.6.2 Development mechanism

In our model of HSQ development below, we imagine the formation of a "crust-like" cross-linked surface that slows down or prevents further development. This phenomenon could be responsible for the self-limiting nature of the HSQ development process and has been studied (for TMAH development) by H.S. Lee *et. al.* [81].

During development, chemical reactions occur resulting in dissolution in lightly exposed areas and further cross-linking in highly dosed areas. The two main reactions that occur are ionization and cross-linking. Ionization promotes dissolution while cross-linking retards dissolution. The presence of several competing reactions occurring during development has been suggested in recent studies on the dissolution of HSQ [82, 83].

The ionization reaction occurs as follows: Hydroxy ions OH^- from the aqueous base deprotonate the Si-H functional group to form Si-O^- and release hydrogen gas.

$$\equiv \text{Si-H} + \text{OH}^- \rightarrow \equiv \text{Si-O}^- + \text{H}_2 \uparrow \tag{4.3}$$

These ionized Si-O^- groups could also react with water reversibly to form silanol Si-OH groups and OH^- ions.

$$\equiv \text{Si-O}^- + \text{H}_2\text{O} \rightleftharpoons \equiv \text{Si-OH} + \text{OH}^- \tag{4.4}$$

However, in the presence of high concentrations of hydroxy ions, the reverse process is favored. The exposed resist may also contain $\text{Si}\cdot$ dangling bonds which reacts with water to form silanol groups and H^+ ions. The silanol groups then get ionized by the reverse reaction in equation (4.4).

Dissolution occurs when the displacement of the solute by ionized x-HSQ molecules is energetically favorable. Hence, a x-HSQ molecule will dissolve if its enthalpy of solvation is negative. Since the hydration of the ionized Si-O^- groups has a negative enthalpy, a sufficient density of these hydrated sites need to form on a given x-HSQ molecule before the molecule can dissolve into the bulk aqueous solution with a negative solvation enthalpy. This concept is similar to the critical ionization model of Tsiartas et. al. [75] in which it was proposed that a critical fraction of phenol groups have to be ionized before the photoresist molecule can dissolve.

A competing reaction to dissolution is cross-linking. Cross-linking reduces the density of Si-O$^-$ groups and slows development. Cross-linking occurs when two Si-O$^-$ groups approach each other in the presence of water as shown in the following reaction:

$$\equiv \text{Si-O}^- + \equiv \text{Si-O}^- + \text{H}_2\text{O} \rightarrow \equiv \text{Si-O-Si} \equiv + 2\text{OH}^- \tag{4.5}$$

For cross-linking to occur, the Si-O$^-$ terminations from adjacent x-HSQ molecules need to collide with each other to overcome the electrostatic repulsive force between the like-charged terminations. This condition suggests that cross-linking occurs infrequently. The reverse process can also occur with a low probability as it requires the breaking of strong Si-O-Si bonds by an energetic hydroxy ion.

The relative rates of dissolution vs cross-linking is a function of exposure dose. Consider now development of HSQ of different regimes of exposure doses, i.e. (1) light, (2) heavy, and (3) intermediate doses. In lightly dosed regions, we have a high density of Si-H bonds left unbroken and small x-HSQ molecules. Upon ionization of the Si-H bonds, these x-HSQ molecules dissolve and diffuse away from the surface into the bulk solution. In this regime, development is limited by the flux of OH$^-$ ions required to ionize the high surface density of Si-H bonds.

On the other hand, in the high exposure-dose regime, we have a small density of Si-H bonds and large x-HSQ molecules. In this regime, ionization of the low surface density of Si-H bonds occurs quickly compared to the diffusion of the ionized molecules. After ionization, most of the x-HSQ molecules are too large, are unable to dissolve, and remain on the surface. The fraction of x-HSQ molecules that *can* dissolve diffuse slowly away from the surface due to their large size. Therefore development is limited by diffusion of the ionized molecules away from the surface. The slowly diffusing molecules have longer interaction times, and also have a higher probability of cross-linking with one another. Eventually dissolution slows down to a halt as the entire surface of the resist is cross-linked.

In the intermediate regime, we have medium sized x-HSQ molecules on average. In this regime, diffusion and ionization occur at similar rates. Ionization and dissolution of the smallest molecules occur first leaving behind larger molecules that diffuse slowly. These larger molecules eventually form a mesh on the surface that slows down dissolution. x-HSQ molecules under this mesh can still be ionized and pass through pores in this mesh. Eventually, larger x-HSQ molecules that try to go through the mesh will plug up these pores and development stops.

4.6.3 Hypothesis of the salt effect on HSQ

We see in Fig. 4-4 and 4-7 that the addition of salt sharpens the contrast by reducing loss of resist thickness at high exposure doses and increasing resist dissolution for low doses. To cause this effect, salt would have to increase dissolution rates for low doses and increased cross-linking rates for high doses.

One phenomenon that can explain this effect is electrostatic charge screening due to the presence of salt. In an aqueous solution, ionized particles repel or attract each other through long range Coulomb forces. However, charge screening by mobile oppositely charged particles shortens the range of these forces by an exponential factor[2]. In Fig. 4-17 we show calculations of the electric potential for negatively charged ion in different solutions of deionized water, 1% NaOH and 1% NaOH 4% NaCl. We see that electrostatic screening reduces the range of electric field generated by the ion, therefore effectively reducing its size.

We now consider the effect of charge screening for the three regimes discussed in the previous subsection. For the lightly dosed regime where a high density of Si-H bonds exists, the Si-O^- terminations that form on the surface of the resist causes a build-up in negative charge. This net negative charge repels hydroxy ions

---

[2] For instance, a negatively charged particle with charge q would exhibit a Coulomb potential $V = q/4\pi\epsilon r$ where ϵ is the permittivity of the solution and r is the distance from the center of the charge. On the other hand, this same charged particle when placed in a solution containing highly mobile oppositely-charged particles, will exhibit a screened Coulomb potential $V = (q/4\pi\epsilon r)e^{-\kappa r}$ where κ^{-1} is the Debye screening length, which decreases with increasing concentration of ions in the solutions.

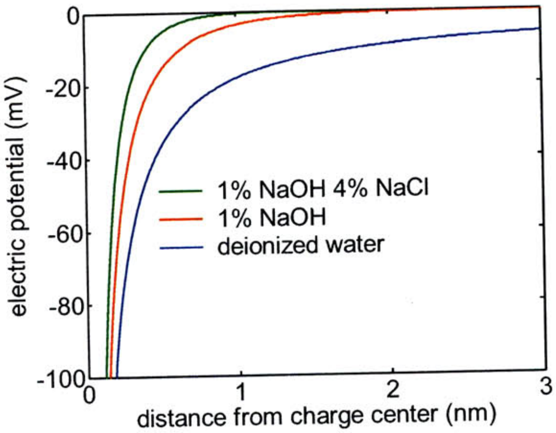

Figure 4-17: Plot of calculated electric potential vs distance from the center of a negatively charged ion in different solutions. Electrostatic charge screening due to the high concentration of mobile ions in 1% NaOH 4% NaCl effectively reduces the interaction volume of the ion.

from approaching the surface and slows down the reaction [84, 85]. However, in the presence of salt, an electrostatic bilayer forms that screens the charge from surface thus allowing hydroxy ions to continue approaching the surface to sustain a high ionization rate. Hence salt increases dissolution rates at low doses.

On the other hand, in the highly dosed regime, the resist consists of larger cross-linked HSQ molecules with a low density of Si-H bonds. Here, the reaction is not limited by the ionization of the Si-H bonds but by the diffusion of the large molecules. These large molecules that move slowly have a longer interaction time with each other and thus have a higher opportunity to cross-link with one another. In the presence of salt, more effective screening reduces the repulsion between the like-charged Si-O^- terminations. This screening allows the ionized terminations to approach more closely and promotes cross-linking. Thus, in regions of high exposure doses, the addition of salt increases cross-linking. This effect explains the smaller loss in resist thickness at doses above 700 $\mu C/cm^2$.

Finally, in intermediate doses, enhanced cross-linking due to the presence of salt causes the mesh of cross-linked x-HSQ molecules to quickly form. This mesh slows down the dissolution rate in the salty developer but does not halt it. Screening which makes the effective sizes of ions smaller, allows ionized x-HSQ and hydroxy ions to continue inter-diffusing through the pores in this mesh, therefore allowing development to proceed beyond 2 mins (see Fig. 4-7). In the non-salty developer, this mesh forms later. Hence a larger fraction of x-HSQ dissolves, leaving behind only the larger x-HSQ molecules trapped under the mesh. These larger molecules plug up the mesh quickly causing the complete cross-linking of the surface and prevents development from proceeding beyond 2 mins.

We acknowledge that we do not fully understand how salt enhances the contrast of HSQ. However, we suspect that this effect may be due to charge screening by the salt. While we do not provide a conclusive explanation at this point, these salty development effects could be a means to a better understanding of HSQ development mechanisms in future experiments.

4.7 Conclusion and future work

The high-contrast salty development process has enabled us to fabricate dense sub-10-nm-pitch structures with minimal loss in resist thickness. We have improved the resist contrast performance to the point where the resolution is no longer limited by the resist but by the EBL system.

The central result of this chapter is a new method to increase the contrast of HSQ by adding salt to an aqueous alkali developer. Contrast increased with increasing salt concentration while resist sensitivity did not change.

Future work should focus on understanding of the development mechanism of HSQ, and on the continual application of this high-resolution patterning technique as an enabling technology in other areas of research. The understanding of HSQ development mechanism should focus especially on investigating development at the nano-scale. In this regime, resolution may be limited not so much by resist contrast but by material diffusion.

Several applications that we have considered are the fabrication of molds for nanoimprint lithography [86], patterning of high-density bit-patterned media (discussed in the following chapter and in Ref. [87]), and graphene nanoribbons.

Chapter 5

Templated self-assembly of block copolymers using a 2D array of HSQ nanoposts

In the previous chapter, we showed that EBL can pattern high-resolution structures down to ~9-nm-pitch dimensions. This resolution capability is about an order of magnitude higher than the resolution of optical projection lithography OPL, which is the current workhorse of the semiconductor industry. Although EBL is used in making the reticles (photomasks) for optical projection lithography systems, it is not used in high-volume manufacturing due to its low throughput. It exposes resist in a serial fashion using a single focused electron beam thus taking a long time to cover an entire wafer. For instance, it would take more than year of exposure to pattern a 10-nm-pitch array of dots covering a full 3-inch wafer.[1] Therefore, we have a dilemma in the regime where ultra-high resolution large-area patterning is required. In this regime, we have resolutions that cannot be achieved by OPL, and large areas that take too long for EBL to pattern.

In this chapter, we show that this problem of low throughput in EBL can be addressed by combining top-down with bottom-up techniques; namely EBL with block

---

[1] This calculation assumes realistic values for beam current of 1 nA, exposure dose of 1 fC per dot and neglects beam settling times and field stitching, which would increase the write time even more.

copolymer self-assembly. Block copolymers (BCPs) are fascinating polymer materials that are capable of self assembling to form nanoscale microdomains simultaneously over large areas. By controlling the composition of the polymer, different morphologies such as spherical, cylindrical and lamellar can be achieved [88]. Although BCPs have high resolution and high throughput, they lack placement accuracy or registration because they form nanostructures with local but not global (long-range) order. An example of this disordered formation of nanostructures is shown in Fig. 5-2B for spherical morphology BCPs. However, by combining EBL with BCP, we provide a template made by EBL that the BCPs can use to form ordered lattices of BCP nanostructures. With the fabrication process described in the previous chapter, we can make well-registered structures that are small enough for interactions with the BCP microdomains. This approach simultaneously increases throughput because the EBL only needs to expose a fraction of the patterns and have the BCP "fill-in" the missing structures. The result is a method which is suitable for nanomanufacturing that achieves high-resolution, high-throughput, and accurate pattern registration.

5.1 Introduction

BCPs are composed of chemically distinct polymer chains (blocks) that are joined on their ends a covalent bond to form a single longer chain. For example, a polystyrene-b-polydimethylsiloxane (PS-b-PDMS) BCP consists of a chain of PS that is covalently bonded to a PDMS chain. BCPs have been thoroughly studied for nearly half a century and are used in industrial applications such as thermoplastic elastomers, adhesives, etc. As a result, BCPs are ubiquitous, e.g. you can find them even in the rubber soles of your shoes.

Recent interest in BCPs has been driven by the potential use of BCPs in nanotechnology. The reader is referred to the review articles of S.B. Darling [89] and C.T. Black et. al. [90] on BCP self assembly in nanofabrication applications. The self-assembly of nanometer-length-scale patterns in two dimensions (2D) is currently actively investigated as a method for improving throughput and resolution in nanolithography. Self-assembly in 2D has been studied widely in a range of other systems, including self-assembled monolayers [91], quantum dots [92], and colloidal particles [93]. Among these systems, the self assembly of BCP thin films is interesting because of the intrinsic ability of BCPs to microphase separate [94] to generate uniform and periodic nanoscale structures in parallel over large areas.

In recent years, significant scientific effort has been expended to control the morphology and ordering of BCP thin films on a surface. BCP thin films with spherical, cylindrical, or lamellar morphologies of different length scales can be created by adjusting the composition and molecular weight of the BCP [88]. These morphologies can be employed for the fabrication of nanostructures: after selectively removing one of the blocks, the remaining pattern can be transferred into a functional material [95, 96, 97, 98, 29, 99]. However, the spontaneous process of microphase separation leads to the formation of "polycrystalline" BCP microdomain arrays consisting of randomly oriented ordered regions, or grains, which limits the potential applications. This issue has sparked the development of a host of techniques that attempt to control the ordering of thin-film BCP systems, that is, to template the positions of the microdomains and to form "single-crystal" structures in which the locations and orientations of the microdomains are precisely determined [100, 101, 89]. These techniques in the past have included the use of topographically [28, 102, 103] or chemically [104, 30, 105] patterned substrates as templates for the self-assembly process. Recent work has extended the chemical patterning technique such that templates with a period of up to four times that of the BCP could be used to produce large-area defect-free lamellar or cylindrical domain patterns [106, 107].

The disadvantage of chemical patterning is that the chemical template does not lend itself to direct inspection before or after BCP processing. For instance, one cannot observe the chemical patterns directly using a SEM. Instead, one indirectly inspects the template by inspecting relief structures in photoresist used in the process step before the chemical patterns are obtained.

Another disadvantage of chemical patterning is that the BCP that self-assembles on top of the template also hides the template from subsequent inspection. This effect prevents direct observation of the relative registration between the BCP and the underlying template. On the other hand, with a physical template, we could simultaneously observe the BCP and template structures. Therefore, we could investigate the conditions for commensuration, which was important for achieving good BCP ordering.

Previous work on physical templating has used structures much larger than the microdomain of the BCP and occupied valuable substrate area. For instance, trenches [102, 108, 109] were used to guide BCPs resulting in the desired BCP nanostructures only within the trenches, leaving the rest of the template unpatterned. The use of such templating structures therefore could not achieve fully dense patterning, which is required in most applications where pattern density is of utmost importance. Furthermore, in the case of spherical BCP, the trenches did not provide pattern registration along the direction of the trench where the BCP spheres can freely strain and translate.

Here, I present a method of templating BCPs using a 2D array of nanoposts that substitute for individual BCP microdomains and do not take up valuable substrate area. Each of these posts was designed to be chemically and physically nearly indistinguishable from the BCP entity (the microdomain and its associated corona) for which it substitutes. The HSQ nanoposts effectively "blend in" as one of the BCP spheres. However, depending on the diameter of the posts and processing conditions, they could appear brighter than the BCP spheres under SEM inspection. As we could directly observe the resulting BCP structures relative to the template, we realized that there were several different commensurate conditions that could exist as the template lattice spacing was varied.

This approach differed from previous approaches, which used linear substrate steps or grooves [101, 103], in that here the discrete posts were distributed over the substrate, providing a set of periodic constraints that interact both locally and globally with the array of BCP domains. Most of the work presented here has been published in Science [87].

The process of templating, i.e. template fabrication and BCP processing atop this template will be described next.

5.2 Templating

Templating was necessary to provide order and registration to the BCP which would otherwise form random polycrystalline structures. The template consists of a 2D hexagonal array of HSQ posts made by EBL and acts as a grid for the BCP providing a set of periodic constraints that interact both locally and globally with the array of BCP domains.

To template the BCP self-assembly, we fabricated and chemically functionalized the templates, spun-on BCP, annealed and selectively etched away one of the BCP blocks before inspection in a SEM. These processes are described in the following subsections.

5.2.1 Template fabrication

The templates were fabricated using EBL patterning of HSQ. EBL was a suitable tool in our experiments because it makes HSQ nanoposts with diameters smaller than the microdomains of the BCP which were $\sim 20\,\mathrm{nm}$ in our experiments. Furthermore, EBL had the flexibility of patterning templates of different lattice spacings on the same substrate. This flexibility allowed us to perform a controlled experiment in which templates with a range of lattice spacings could be processed in a single experimental run.

The template fabrication process was as follows: HSQ (formulated as the product XR-1541 2 % solids from Dow Corning) was spun coated onto silicon wafers to a thickness of 40 nm as measured by ellipsometry. Sample sizes were typically $\sim 2\,\mathrm{cm}$ squares obtained by cleaving the silicon wafers. Single-pixel dots were exposed in a Raith 150 EBL tool at 30 kV acceleration voltage using doses of $\sim 15\,\mathrm{fC}$ per dot. The electron-beam stigmation and focus were optimized by imaging 100-nm diameter gold nanoparticles prior to exposure. Poor stigmation would occasionally result in elliptically patterned dots instead of the desired circular dots. We typically patterned several templates with different exposure doses (to achieve a range of dot diameters) and dot-to-dot spacings (to study commensurate conditions) on a single sample. A

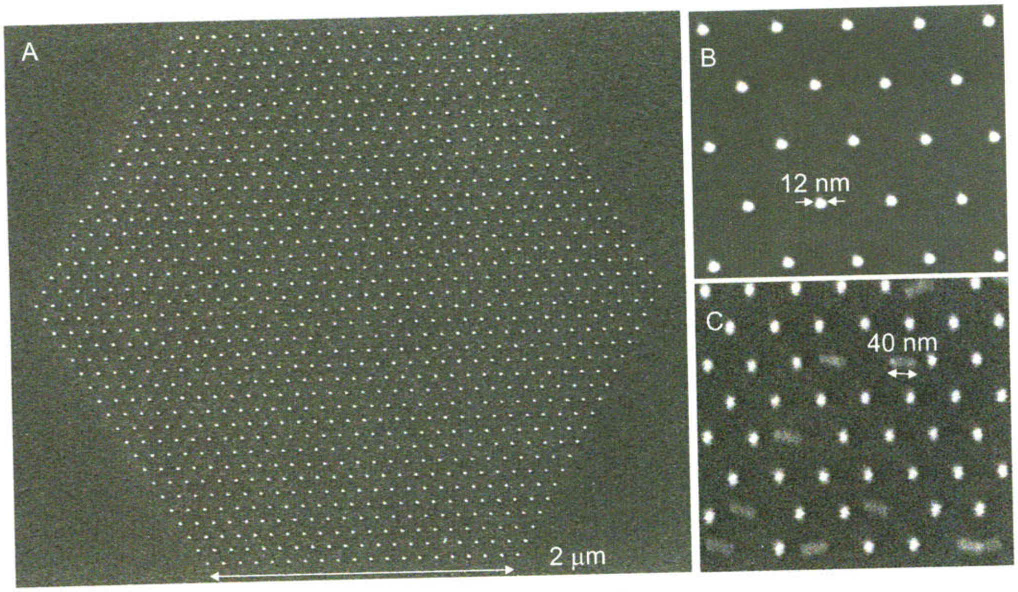

Figure 5-1: Top-view SEM images of the templates consisting of HSQ posts that appear as bright dots on a grey background. These images were taken after EBL and development. (A) SEM of the one of the templates used in our experiments. The template consists of a hexagon with 2 µm long sides that is filled in with a sparse hexagonal array of posts. (B) SEM of a small area of the template showing a larger view of the posts having diameters of ~ 12 nm. (C) The diameter of the posts was smaller in templates exposed at lower exposure doses. Some of these posts have fallen over and appear as dashes in this SEM. The length of these fallen posts were measured to be 40 nm which was consistent with the thickness of HSQ measured using an elipsometer before EBL exposure.

single template consisted of dots within a hexagonal area of 4 µm hexagonal diameter. The samples were developed in the high-contrast salty developer system, as described in Chapter 4, for 4 mins, and further treated in a Technics PlanarEtch II oxygen plasma asher (50 W power, 0.35 T pressure) for 2 min to remove possible organic residues and to convert the surface of the HSQ posts into silica.

Figure 5-1 shows SEMs of one of the templates after EBL exposure and development. As shown in Fig. 5-1A, the template size was typically 4 µm in hexagonal diameter. This size was ideal in our experiments as it allowed us to fabricate hundreds of templates on a single chip with each template having slightly different exposure doses and lattice spacings. A larger view of the nanoposts is shown in Fig. 5-1B showing posts with 12 nm diameter. In Fig. 5-1C, we show a region of the template where some posts have fallen over. These posts had smaller diameters than those in Fig. 5-1B, and due to their higher aspect ratio and the capillary forces during sample drying, they tended to collapse more readily. The height of the nanoposts can be measured by measuring the length of the posts that had fallen over. In Fig. 5-1C, the posts were measured to be 40 nm tall, matching the thickness of HSQ measured by the ellipsometer before EBL.

5.2.2 Functionalizing the template

A key requirement for the templating process to work is for the surface of the posts to exhibit preferential affinity toward one of the domains of the BCP. This requirement was achieved by chemical functionalization of the topographically defined substrates with either PS or PDMS "brushes". This functionalization was done by spin coating a 30-nm-thick layer of hydroxyl-terminated homopolymer (10 kg/mol PS-OH, or 5kg/mol PDMS-OH from Polymer Source Inc.), annealing at 170°C for 15 hours in a vacuum oven, and rinsing in toluene to remove any unreacted homopolymer. During the anneal process, the hydroxy terminations of the polymers reacted with the hydroxy terminations on the native oxide on substrate and on the HSQ posts through a condensation reaction, to form a self-assembled monolayer of the polymer with a thickness of $\sim 2\,\mathrm{nm}$.[2]

5.2.3 BCP processing

The BCP used in our experiments was spherical morphology polystyrene-b-polydimethylsiloxane (PS-b-PDMS) with molecular weight = 51.5 kg/mol, minority block volume fraction $f_{\mathrm{PDMS}} = 16.5\%$, and polydispersity (PDI) = 1.04. This BCP was chosen because it has both a high Flory-Huggins χ-parameter [110, 111], giving a large driving force for microphase segregation, and a high chemical selectivity between the two blocks for subsequent pattern transfer.

Once the template was fabricated and chemically functionalized, we spin-coated a 50-nm-thick PS-b-PDMS (51.5kg/mol, volume fraction f_{PDMS}=16.5%, polydispersity

---

[2] The thickness of this brush layer was estimated by measuring the increase in HSQ post diameters in a SEM after chemical functionalization. Note: we did not verify the height profile of these posts after chemical functionalization.

index PDI=1.04 from Polymer Source Inc.) film from a toluene solution (2.5% by weight of the PS-PDMS block copolymer) onto the template. Then, the samples were vacuum annealed at 200°C for 12 hours. Annealing of the BCP resulted in a monolayer of 20-nm-diameter PDMS spheres with a center-to-center spacing of 40 nm within a PS matrix. A surface layer of PDMS also formed at the substrate-BCP and BCP-air interfaces due to the low surface energy of PDMS [99].

The annealed film was etched in a Plasmatherm reactive-ion etcher with a 5 s, 50 W CF_4 plasma to remove the PDMS surface layer, followed by a 30 s, 90 W O_2 plasma to selectively remove the PS domains and form oxidized PDMS posts on the substrate. A thin ($\sim$2 nm) layer of Au-Pd alloy was sputter-coated on samples to avoid charging effects. The resulting surface morphology was then imaged in the Raith 150 EBL operated at an acceleration voltage of 10 kV at 6 mm working distance.

5.2.4 Results

Figure 5-2 shows a schematic of the topographic and chemical design of a single post and the BCP that surrounds it. The template was functionalized with a short PDMS homopolymer brush, and a post substituted for a PDMS sphere in the close-packed array. The template was also fabricated with an affinity toward the majority block by using a PS brush, which required larger-diameter HSQ posts. PDMS brush-coated substrates provided better ordering of PS-b-PDMS microdomain arrays than PS-coated or uncoated substrates, which we attribute to higher surface diffusivity of the PDMS brush [99]. The use of PDMS brush-coated posts, which required the ability to fabricate $\sim$ 10-nm structures lithographically, was enabled by our work [39] as described in Chapter 4.

Figure 5-2C and 5-2D, shows that appropriately sized and functionalized posts could template the assembly of a BCP lattice. For comparison, Fig. 5-2B shows the results of untemplated assembly for the same BCP. In this untemplated case, the BCP forms polycrystalline structures. The grain boundaries are shown as the drawn dashed lines. In this situation, the BCP microdomains within each grain has a natural center-to-center spacing $L \sim 40$ nm. The template in Fig. 5-2C consisted

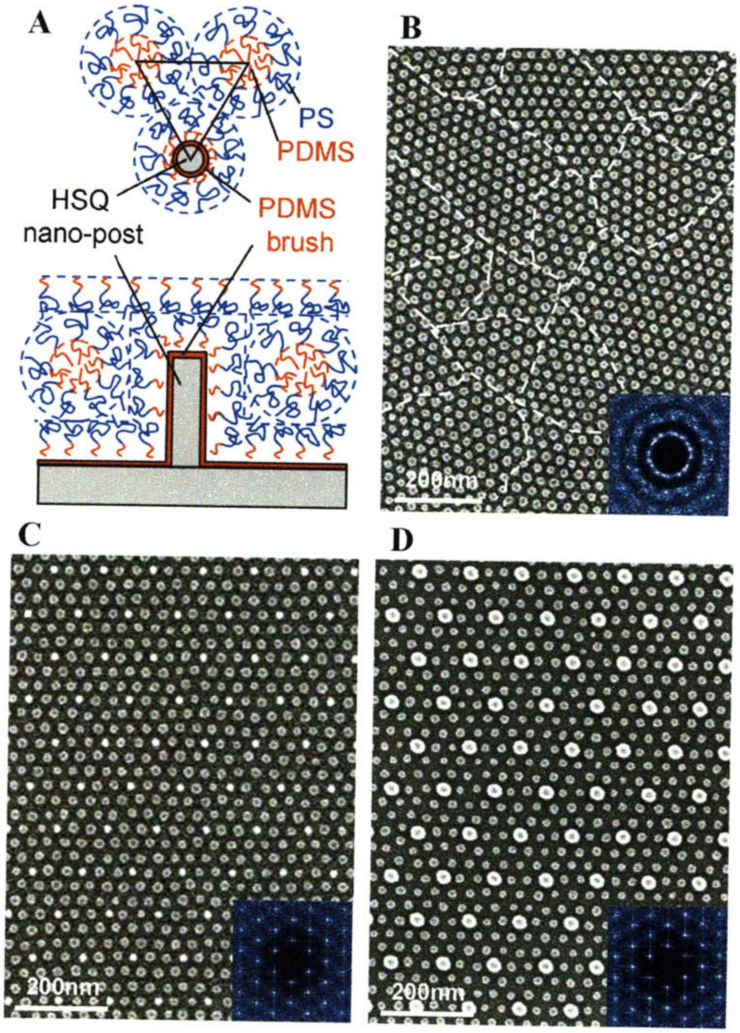

Figure 5-2: Top-down and side-view schematics showing the arrangement of PS-b-PDMS block copolymer molecules in the region surrounding a single post made from cross-linked HSQ resist. The post and substrate surfaces have been chemically functionalized by a monolayer of short-chain PDMS brush. (B) SEM images of a poorly ordered monolayer of BCP spherical domains formed on a flat surface, that is, without templating. The boundaries between different grain orientations are indicated with dashed lines. The inset is a 2D Fourier transform of the domain positions that shows the absence of long-range order. (C and D) SEM images of ordered BCP spheres formed within a sparse 2D lattice of HSQ posts (brighter dots). The substrate and post surfaces were functionalized with a PDMS brush layer in (C), which corresponds to the schematic in (A), and with a PS brush layer in (D). The insets show the 2D Fourier transforms in which the low-frequency components originate from the post lattice.

of ~12-nm-diameter HSQ posts functionalized with PDMS (5 kg/mol) of thickness ~2 nm, resulting in a post diameter of ~16 nm. Figure 5-2D shows results from 20-nm-diameter HSQ posts functionalized with PS (10 kg/mol) of ~5 nm thickness, resulting in a post diameter of ~30 nm.

5.3 Commensuration between template and BCP lattices

Commensuration occurs when we can fit an integer number of BCP spheres among the template posts without stretching or compressing the BCP. In the images shown in Fig. 5-2C and D, we showed an example where two BCP microdomains fitted in between two HSQ nanoposts. In that example, the BCP lattice was commensurate with the template lattice and the BCP lattice was minimally strained. We next considered what would happen when we increased or decreased the spacing between the nanoposts. For small changes in spacing, we would expect the BCP to stretch or compress to "fit" into the lattice. But for larger changes, there will be other orientations where the BCP is commensurate with the template such that the BCP lattice will rotate relative to the template lattice to fit without straining. In this section, we investigate the conditions for commensuration between two hexagonal lattices of different lattice spacings. Finding commensurate conditions for larger template lattice spacing is useful for investigating the feasibility of using a sparse template while still forming of a single-grain BCP lattice of controlled period and orientation.

For a hexagonal-close-packed template of period L_{post}, and a hexagonal close packed BCP microdomain array of period $L < L_{\text{post}}$, the commensurability between the BCP lattice and the template lattices depends on the ratio L_{post}/L. In the simplest case, where L_{post}/L is an integer, the lattice vectors of the template and the BCP sphere array are parallel, as seen in the SEM images of Fig. 5-2C and 5-2D, where $L_{\text{post}}/L = 3$, and θ, the angle between a post lattice basis vector and a BCP

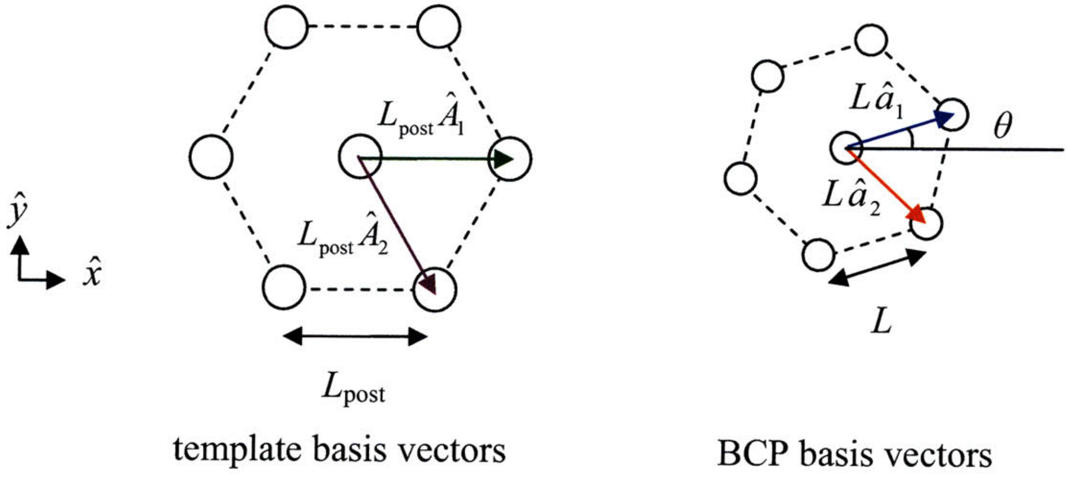

Figure 5-3: Schematic of the template lattice and BCP lattice basis vectors. For convenience, $\hat{A}_1$ was made parallel to the $\hat{x}$ vector of the cartesian coordinate. The BCP lattice vectors are allowed to be rotated relative to the template lattice by an angle θ.

microdomain lattice basis vector, is zero. For noninteger values of L_{post}/L, however, a variety of commensurate BCP lattices with orientations $\theta \neq 0$ can occur. We can calculate these orientations as follows:

Figure 5-3 shows the relative orientations of the template and the BCP lattice and the notation we use for the basis vectors. The basis vectors of the template lattice are $\vec{A}_1$ and $\vec{A}_2$ where:

$$\begin{aligned}
\vec{A}_1 &= L_{\text{post}}\hat{A}_1 && (5.1)\\
&= L_{\text{post}}\hat{x} && (5.2)\\
\vec{A}_2 &= L_{\text{post}}\hat{A}_2 && (5.3)\\
&= L_{\text{post}}\left(\frac{1}{2}\hat{x} - \frac{\sqrt{3}}{2}\hat{y}\right) && (5.4)
\end{aligned}$$

The basis vectors of the BCP lattice, $\vec{a}_1$ and $\vec{a}_2$, can be similarly expressed with the addition of a rotational operator R_θ where:

$$\begin{aligned} \vec{a}_1 &= L\hat{a}_1 && (5.5)\\ &= R_\theta \left[L\hat{x} \right] && (5.6)\\ \vec{a}_2 &= L\hat{a}_2 && (5.7)\\ &= R_\theta \left[L \left(\frac{1}{2}\hat{x} - \frac{\sqrt{3}}{2}\hat{y} \right) \right] && (5.8)\\ R_\theta &= \begin{pmatrix} \cos\theta & -\sin\theta \\ \sin\theta & \cos\theta \end{pmatrix} && (5.9) \end{aligned}$$

In general, a commensurate configuration will occur when either of the post basis vectors can be written as a linear combination of integer multiples i and j of the BCP lattice basis vectors. For instance, one can choose to represent the horizontal lattice basis vector $\hat{A}_1$ as a linear combination of $\hat{a}_1$ and $\hat{a}_2$ as follows:

$$\vec{A}_1 = i\vec{a}_1 + j\vec{a}_2 \tag{5.10}$$

Substituting equation 5.2, 5.6 and 5.8 into 5.10 gives us the following:

$$\begin{aligned} \begin{pmatrix} 1 \\ 0 \end{pmatrix} L_{\text{post}} &= R_\theta \begin{pmatrix} i + \frac{j}{2} \\ -\frac{\sqrt{3}j}{2} \end{pmatrix} L \\ &= \begin{pmatrix} \cos\theta & -\sin\theta \\ \sin\theta & \cos\theta \end{pmatrix} \begin{pmatrix} i + \frac{j}{2} \\ -\frac{\sqrt{3}j}{2} \end{pmatrix} L && (5.11)\\ L_{\text{post}}\hat{x} &= L \left(\cos\theta(i + j/2) + \sin\theta(\sqrt{3}j/2) \right) \hat{x} \\ &\quad + L \left(\sin\theta(i + j/2) - \cos\theta(\sqrt{3}j/2) \right) \hat{y} && (5.12) \end{aligned}$$

Taking the magnitude of the vectors in equation 5.12 and after some algebra, we obtain the following equation:

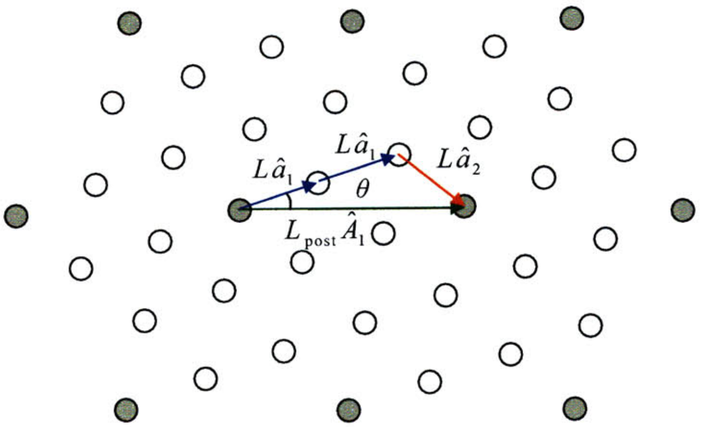

Figure 5-4: Schematic showing an example of a commensurate condition where the BCP spheres are open circles and the HSQ posts are filled-in circles. In this example, the BCP lattice was rotated at an angle of $\theta = 19.1°$ relative to the template lattice. The template basis lattice vector (green arrow) can be expressed in terms of the BCP basis lattice vectors (2 blue and 1 red arrow).

$$L_{\text{post}}/L = \sqrt{i^2 + j^2 + ij} \tag{5.13}$$

Equation 5.13 allows us to calculate the values of L_{post}/L that satisfy the commensurate condition. Typically, L is set by the natural occuring period of the BCP film. Therefore equation 5.13 gives us the values of L_{post} when the template is commensurate with the BCP lattice. We can get the corresponding orientations of the BCP lattice relative to the template by solving for θ from the $\hat{y}$ component of equation 5.12 as follows:

$$\theta = \text{atan}\left(\frac{\frac{\sqrt{3}j}{2}}{i + \frac{j}{2}}\right) \tag{5.14}$$

Figure 5-4 shows an example of a commensurate configuration where the BCP lattice is rotated by an angle θ relative to the template lattice. The filled-in circles represent the posts on the template and are coincident with the BCP lattice. In this example $\hat{A}_1 = 2\hat{a}_1 + \hat{a}_2$, and using equation 5.13, $L_{\text{post}}/L = \sqrt{2^2 + 1^2 + 2} = \sqrt{7}$. Using equation 5.14, $\theta = \text{atan}(\frac{\sqrt{3}/2}{2+1/2}) = 19.1°$.

We use a notation of the form $\langle ij \rangle$ to describe the possible commensurate BCP

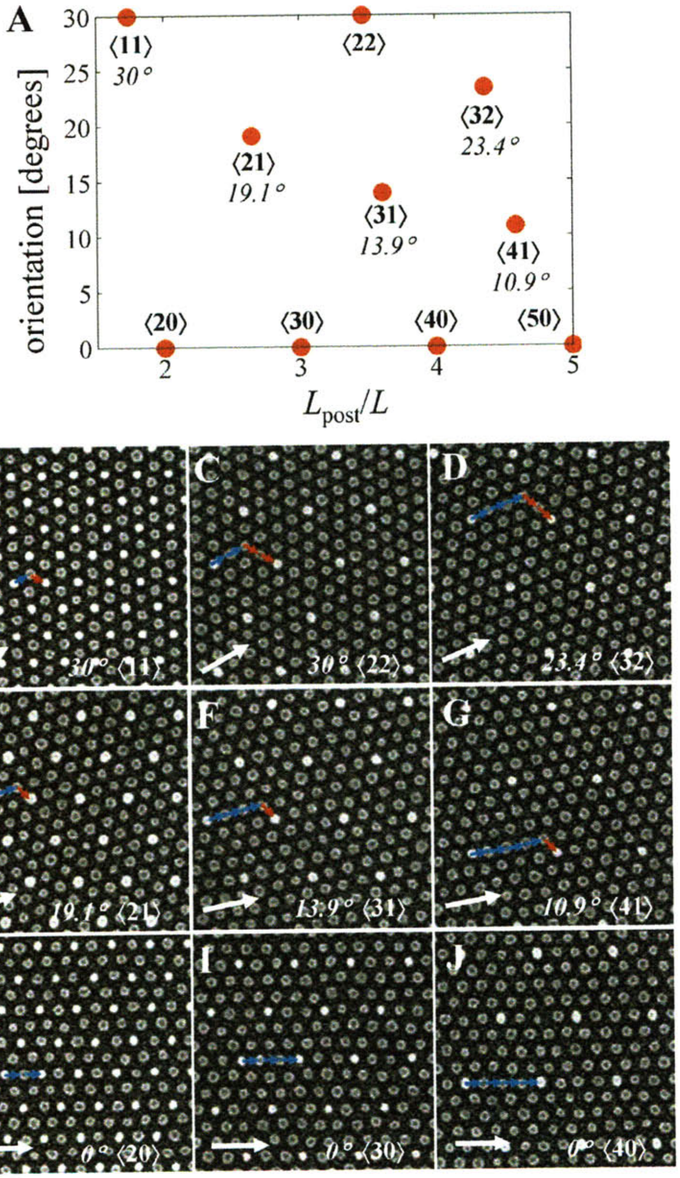

Figure 5-5: (A) Calculated orientations at which the BCP microdomain lattice is commensurate with the post lattice, as a function of L_{post}/L. The BCP lattice is commensurate with the post lattice when the post lattice basis vectors of length L_{post} can be represented as integer multiples, $\langle i\,j \rangle$, of the BCP lattice basis vectors of equilibrium length L. Because of the 6-fold symmetry of the BCP lattice, the angular span of 0°to 30°is sufficient to represent all possible nondegenerate orientations. (B to J) Plan-view SEM images of all the commensurate configurations found in (A) for the L_{post}/L ratio range of 1.65 to 4.6. The white arrows show the orientation angle between the BCP microdomain lattice and the post lattice and are 120 nm long. The brighter dots are the oxidized HSQ posts, whereas the darker dots correspond to oxidized PDMS spherical domains. The blue and red arrows indicate the basis vectors of the BCP microdomain lattice and add up to form one horizontal basis vector of the post lattice.

Lattice	*i*	*j*	L_{post}/L	θ [°]
⟨10⟩	1	0	$\sqrt{1} = 1.00$	0.0
⟨11⟩	1	1	$\sqrt{3} = 1.73$	30.0
⟨21⟩	2	1	$\sqrt{7} = 2.65$	19.1
⟨31⟩	3	1	$\sqrt{13} = 3.61$	13.9
⟨32⟩	3	2	$\sqrt{19} = 4.36$	23.4
⟨41⟩	4	1	$\sqrt{21} = 4.58$	10.9
⟨51⟩	5	1	$\sqrt{31} = 5.57$	9.0
⟨43⟩	4	3	$\sqrt{37} = 6.08$	25.3
⟨52⟩	5	2	$\sqrt{39} = 6.24$	16.1
⟨53⟩	5	3	$\sqrt{49} = 7.00$	21.8
⟨54⟩	5	4	$\sqrt{61} = 7.81$	26.3

Table 5.1: $\langle ij \rangle$ commensurate post lattice spacing and orientations corresponding to the 11 unique orientations in a 2D hexagonal BCP lattice with i, $j \leq 5$ and spacing L.

lattice configurations that can form within a post lattice. For example, the structures shown in Fig. 5-2C and 5-2D would be labeled as $\langle 3\ 0 \rangle$ under this notation, indicating that a post lattice basis vector is parallel to a BCP microdomain lattice vector and three times as long. Similarly, the configuration in Fig. 5-4 would be labeled as $\langle 2\ 1 \rangle$.

Figure 5-5A presents a map of the mathematically possible commensurate lattice $i\ j$ orientations in which the L_{post}/L ratio was varied continuously up to $L_{\text{post}}/L = 5$. For each of these orientations, the number of microdomains templated by each post is given by $i^2 + j^2 + ij - 1$. For example, 8 BCP microdomains are templated per post for the $\langle 3\ 0 \rangle$ lattice and 26 for the $\langle 3\ 3 \rangle$ lattice.

Table 5.1 lists all the possible orientation angles and L_{post}/L values for the case when i, $j \leq 5$. These values correspond to the map of Fig. 5-5A. For each angle, a family of lattices exists corresponding to multiples of i and j, e.g. at $\theta = 0$, the family is $\langle 1\ 0 \rangle$, $\langle 2\ 0 \rangle$, $\langle 3\ 0 \rangle$ ...

Figure 5-5, B to J, shows SEM images of all the commensurate orientations that we observed within the range $L_{\text{post}}/L = 1.65$ to 4.6. These orientations agree with the predictions in Fig. 5-5A. BCP arrays may develop a tensile or compressive strain to fit within a template, as observed in confined spherical, cylindrical, or lamellar arrays [30, 112]. Confined BCP arrays are capable of exhibiting strain, with tension being easier to accommodate than compression [113]. This compliance enables a greater number of configurations to be experimentally accessed at particular values of L_{post}/L than the discrete results in Fig. 5-5A would suggest. The ability of the BCP microdomain lattice to deform elastically therefore enables multiple BCP orientations to form on a given post lattice. Each orientation in this case has a different lattice spacing and orientation θ.

5.4 Free energy model

As discussed in the previous section, several BCP orientations may form on the same template. Even in the case where the template is perfectly commensurate with the BCP lattice, we could have regions where the BCP is strained in a non-commensurate orientation. To understand how energetically unfavorable it is for such a situation to occur, we considered a free energy model for the BCP. The model we developed will give us an estimate of the free-energy cost for several orientations to occur simultaneously.

5.4.1 Theory

We present a simple free energy model developed to describe a BCP lattice that is allowed to undergo in-plane strain in order to achieve commensuration on a given periodic template. The previous section and Fig. 5-5A described the case of perfect commensuration, where L_{post}/L values satisfied the commensurate condition of equation 5.13 and in most cases, there was only one possible orientation between the BCP lattice and the post lattice. However, the BCP lattice may be able to adopt multiple orientations for certain L_{post} values by slightly expanding or shrinking so that commensuration is achieved at particular values of the L_{post}/L ratio, where L, the strained BCP lattice spacing, differs from the equilibrium spacing, L, adopted in the absence of the template.

Given an i j configuration and a post spacing L_{post} such that the commensurate sublattice period L differs from the equilibrium spacing of the BCP on a flat substrate,

L, the templated BCP may either assume a strained spacing and fit inside the post lattice, or form local defects and relieve the long-range stress. The free-energy change for straining the BCP lattice can be approximated under an affine deformation model by considering the effect of strain on both the conformational entropy of a polymer chain and the interfacial energy between the BCP domains.

The following derivation of the free energy model was adapted from the free energy model for cylindrical phase BCP derived by Yeon Sik Jung [114]. To derive a free energy, ΔF, we assumed an affine deformation where the relative deformation of an individual BCP chain is the same as the macroscopic strain, λ, of the BCP lattice. For hexagonal symmetry in 2D, the elastic modulus is isotropic, justifying the use of a 1D strain model. The free energy change for an A-B diblock copolymer chain can be defined as:

$$\Delta F_{\mathsf{chain}} = \Delta H - T\Delta S = \gamma_{AB} A - T\Delta S_{conf} \tag{5.15}$$

where γ_{AB} = interfacial tension between the A and B blocks, A = interface area per chain, T = temperature, and ΔS_{conf} = change in conformational entropy per chain.

The change in conformational entropy for a strained ideal polymer network is:

$$\Delta S_{conf} = -\frac{k}{2}\left(\lambda_x^2 + \lambda_y^2 + \lambda_z^2 - 3\right) \tag{5.16}$$

where k = Boltzmann constant, and λ_i are the strains in the $i = x, y, z$ directions. Further assuming an incompressible system ($\lambda_x\lambda_y\lambda_z = 1$) and that $\lambda_x = \lambda$, the entropy term becomes:

$$\Delta S_{conf} = -\frac{k}{2}\left(\lambda^2 + \frac{2}{\lambda} - 3\right) \tag{5.17}$$

The strain is calculated with respect to a Gaussian-coil reference state:

$$\lambda = \frac{L/2}{b\sqrt{M}} \tag{5.18}$$

where b = statistical segment (Kuhn) length, and M = number of statistical steps.

In a Gaussian coil, the root mean square distance between the start and the end of a random walk chain is given by $b\sqrt{M}$. The enthalpic contribution to ΔF_{chain} is related to the change in interfacial energy upon deformation of the polymer chain. The interfacial tension between the A and B blocks of an A-B diblock copolymer can be estimated from the Helfand-Tegami expression for the interfacial energy between A and B homopolymers [115]:

$$\gamma_{AB} = \frac{kT}{b^2}\sqrt{\frac{\chi_{AB}}{6}} \tag{5.19}$$

where χ_{AB} is the Flory-Huggins interaction parameter between the A and B blocks of the diblock copolymer.

The interface area for the microphase separated chain can be estimated as:

$$A \cong \frac{V_{\text{chain}}}{L/2} = \frac{Mb^3}{L/2} \tag{5.20}$$

where half the BCP spacing is chosen to correspond to the length of one chain, and we assume that the chain is made up of M number of cubic Kuhn segments, each having a volume of b^3. Thus, by using equations 5.17, 5.18, 5.19, and 5.20, we can derive an expression for the free energy:

$$\Delta F_{\text{chain}}/kT = \frac{2Mb}{L}\sqrt{\frac{\chi_{AB}}{6}} + \frac{1}{2}\left(\frac{L^2}{4Mb^2} + \frac{4b\sqrt{M}}{L} - 3\right) \tag{5.21}$$

The equilibrium spacing L occurs at the minimum value of $\Delta F_{\text{chain}}/kT$ and can be found by differentiating $\Delta F_{\text{chain}}/kT$ in equation 5.21 with respect to L and setting it to zero. This equilibrium spacing was calculated as $L = 26.2\,\text{nm}$ by using $\chi_{AB} = 0.18$ (at 200°C, the sample anneal temperature), $M = 231$, and $b = 0.56$ nm (estimated as a weighted mean of the Kuhn steps for PS and PDMS reported elsewhere) [116, 117]. Given the simplicity of the model, this value is acceptably close to the experimental value of 40 nm.

The free-energy calculations of this model are shown in Fig. 5-5A where we have plotted $\Delta F_{\text{chain}}/kT$ as a function of L_{post}/L for all the i j combinations. The data plots in Fig. 5-5B will be described in the following subsections. The plots for all the $i\ j$ combinations, was obtained by substituting $L = L_{\text{post}}/\sqrt{i^2+j^2+ij}$ into equation 5.21. Each distinct $i\ j$ lattice has an energy well with a minimum corresponding to the value of L_{post}/L at which the post lattice is commensurate with an unstrained BCP microdomain lattice.

5.4.2 Experiment

The predictions of the free energy model above were tested using the following experiment:

We prepared on a single substrate several sets of templates with the range of L_{post} = 66 to 184 nm corresponding to $L_{\text{post}}/L \sim 1.65$ to 4.6. The fabrication process for this template preparation is described in Sec. 5.2.1. Each template region consisted of posts covering a hexagonal area with a diameter of 4 μm, as shown in Fig. 5-1A. Having multiple templates on the same substrate ensured a uniform BCP film thickness (and hence the same L) across all templates with different L_{post} values.

The different template regions on the same substrate were imaged after BCP processing. SEM images often showed more than one BCP microdomain lattice orientation within each post array. Therefore, we developed an image analysis code in Matlab to quantify the area fractions of the different lattice orientations. Having multiple templates for the same L_{post}/L allowed us to obtain an average area fraction for the various BCP orientations in a particular lattice spacing.

5.4.3 Image analysis

Image analysis was essential for any quantitative analysis of the BCP self assembly. With image analysis, we were able to determine the defect density, area fractions and orientations of different BCP lattices.

The algorithm of the image analysis code is as follows: (1) the code loads an image to be analyzed and looks for the center coordinates of circles or disks in the image (this corresponds to either HSQ posts or BCP dots in this experiment), and (2) the

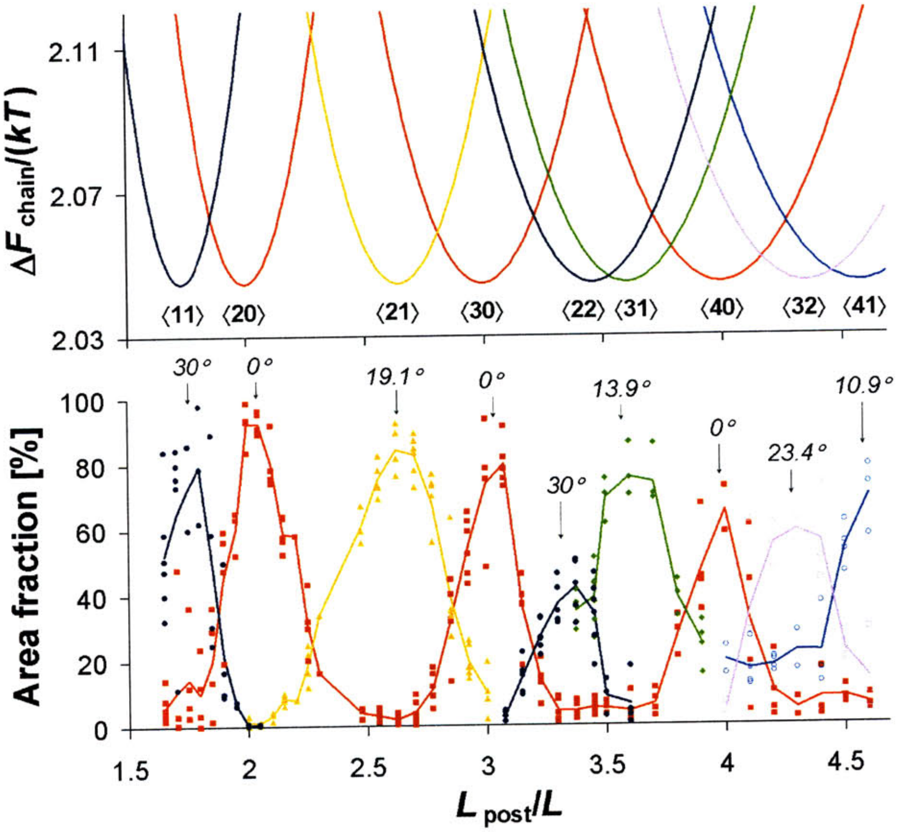

Figure 5-6: (A) Theoretical prediction of free energy per BCP chain versus L_{post}/L for each commensurate configuration. Free-energy minima occur at L_{post}/L values where the commensurate condition is satisfied without straining the BCP microdomain array. (B) Experimental results showing the area fraction of each $\langle ij \rangle$ lattice versus L_{post}/L. Each filled circle is a data point obtained by image processing of an SEM image of a 1.3 μm by 1.3 μm square area of the templated region. This plot was generated from data collected from over 200 images of different post lattices on the same substrate. The solid lines connect the average values of the data points for a given L_{post}/L.

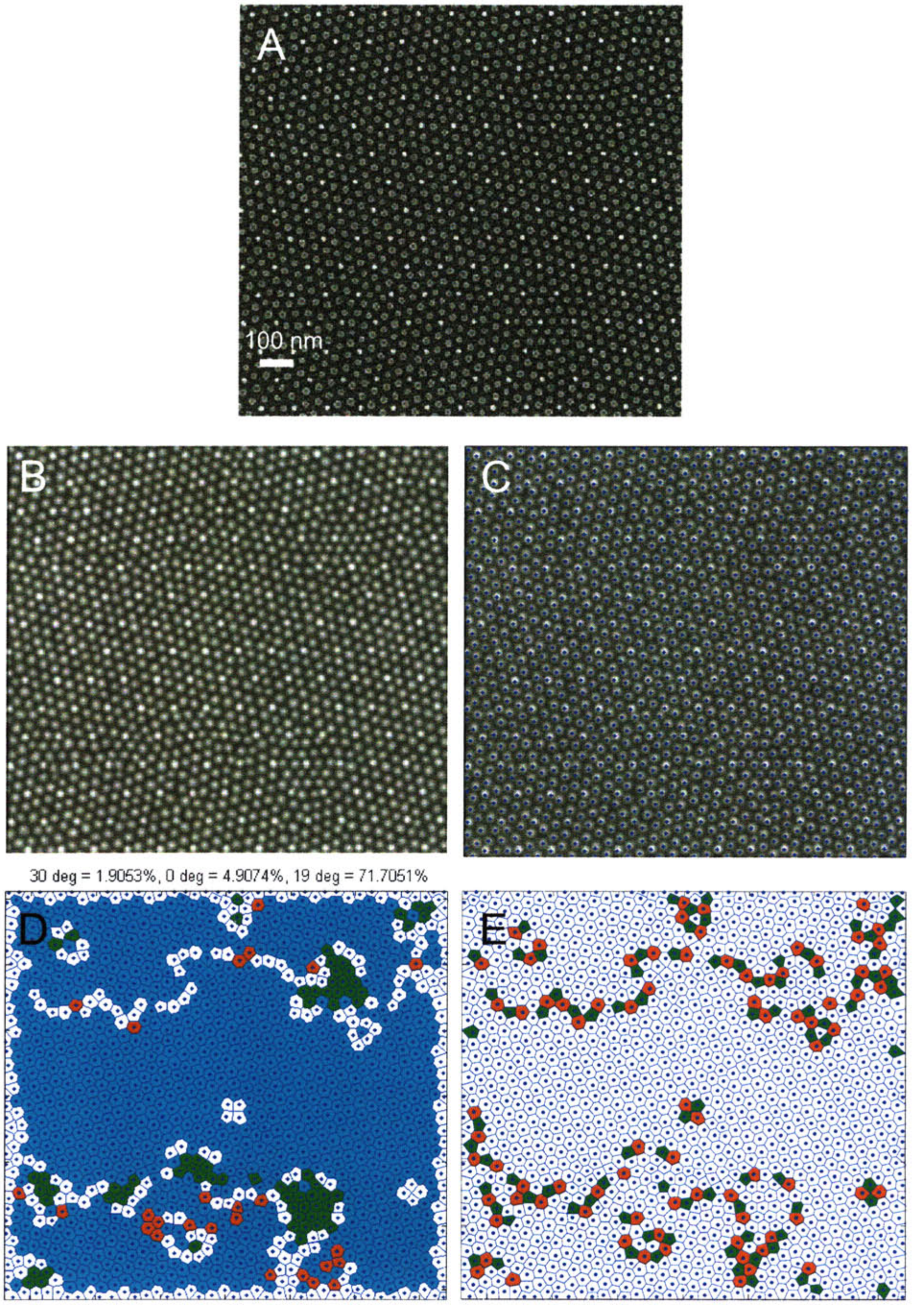

Figure 5-7: (A) SEM image of a templated region with $L_{\text{post}}/L = 2.4$ as input to the image analysis code. (B) The same image as (A) after after correlation with a filter which converts noisy SEM image into an array of "hills" with well defined maxima. (C) Plot of local maxima positions (blue dots) overlayed with the image in (B), the local maxima corresponded to the center of the BCP dots. (D) Voronoi diagram was generated, and the orientation and area of each BCP Wigner-Seitz cell was calculated. In this example, blue $= \pm 19°$, green $= 0°$and red $= 30°$. (E) Voronoi diagram showing the defect sites with five-coordinated and seven-coordinated sites as filled in pentagons (green) and heptagons (red) respectively.

center coordinates were found by first correlating the image with a filter consisting of a disk the size of a dot, then identifying the local maxima in the resultant image.

Figure 5-7A shows an example of a SEM image before analysis. After the correlation function, we obtain Fig. 5-7B in which the dots now appear as an array of well defined peaks. The center of the dots can then be easily identified using a local-maxima-seeking function. The identified dot centers are shown in Fig. 5-7C.

We then generate a Voronoi diagram using these coordinates. For each hexagonal cell in the Voronoi diagram, we calculate the orientation of the cell and its area. The orientation of the cell is not well defined when the cells are not a perfect hexagon, as is often the case. To simplify the analysis, we find the closest fit of the cell from three different orientations. These orientations were chosen based on the commensurate orientations in a given range of L_{post}/L. For instance, in the range of $L_{\text{post}}/L = 1.5$ to 2.5, the chosen orientations were 0°, 30°and 19.1°.

Figure 5-7D shows a Voronoi diagram with filled-in cells corresponding to cells with six sides. Cells without filled-in colors are either defects (i.e. with number of sides $\neq 6$) or have vertices outside the image frame. For this particular image, the majority of the cells (i.e. 72% area fraction) were in the ±19.1° orientations as shown in blue. A small fraction of the cells shown in green (5%) are in the 0° orientation. We can also look at the defects in the image, as shown in Fig. 5-7E, where the five-coordinated defects are in green and the seven-coordinated defects are in red. Note that these five-seven coordinated defects always form in pairs, and are called disclinations [118].

5.4.4 Experimental agreement with free energy model

The data extracted from image analysis of over 200 SEM images is shown in Fig. 5-6B. In this figure, we have plotted the area fraction of the various BCP lattice orientations as a function of L_{post}/L. The experimental results and theoretical predictions in Fig. 5-6 agree closely. All the predicted lattice types, $\langle 1\ 1 \rangle$, $\langle 2\ 0 \rangle$, $\langle 2\ 1 \rangle$, $\langle 3\ 0 \rangle$, $\langle 2\ 2 \rangle$, $\langle 3\ 1 \rangle$, $\langle 4\ 0 \rangle$, $\langle 3\ 2 \rangle$, and $\langle 4\ 1 \rangle$, were observed as L_{post} varied. As expected, a particular lattice type dominated (i.e. had the highest area fraction) at the L_{post}/L value for which the free-energy model predicted a minimum energy for that lattice type.

Note that for the values of L_{post}/L greater than $\sim$3.5, there was no single BCP lattice orientation that completely filled the template, and all samples showed two or more different BCP-lattice orientations. This effect can be understood as being due to the increasing width and number of the potential wells, such that the energy barriers separating different BCP orientations became smaller. A similar phenomenon was observed in previous work with BCP spheres packing in grooves, where N or $N+1$ rows of spheres were observed to occur degenerately for wider grooves [103]. For L_{post}/L less than $\sim$3.5, two lattice types also occurred simultaneously when L_{post}/L was intermediate between values corresponding to energy minima.

For the data presented in Fig. 5-6B, the approximate defect densities were estimated within a $1.5 \times 1.5\,\mu\text{m}^2$ area. In the templated samples with the lowest defect levels, in which 2D commensuration was achieved, the percentage of defects (5-fold or 7-fold coordinated spheres) was less than 2%. In these instances, the orientational and translational order of the BCP was preserved over the entire templated area despite the small number of defects. The translational and orientational order is preserved over large distances due to the pinning action of the lithographically defined posts which themselves also had excellent long range order.

In nontemplated films, the largest defect-free regions observed were on the order of $0.4 \times 0.4\,\mu\text{m}^2$. On the other hand, in the templated case, for $L_{\text{post}}/L <\sim 3$ defect-free arrays were observed over $2 \times 2\,\mu\text{m}^2$ or greater areas. In cases where only one BCP lattice orientation existed, any defects that occurred did not disrupt the long-range orientation of the array, because the self assembled structure remained in phase with the periodic boundary condition introduced by the template: any point defect that occurred affected only the coordination number and spacing of nearby spherical domains.

In our experiments, the largest L_{post}/L corresponded to the $\langle 4\ 1 \rangle$ orientation, in which one HSQ post templates 20 BCP spheres. At this large L_{post}/L value, we already see that the defect density is $\sim 20\%$. To reduce the defect densities, we could optimize the BCP annealing conditions (e.g. by using solvent instead of thermal annealing or by optimizing the annealing temperature), and use strategic designs of the template (e.g. double-dot and non-periodic templates) which we describe next.

5.5 Other templating strategies

We have so far shown templates that consisted of single posts at every lattice point of a hexagonal lattice. In this section we will show how we can control the orientation of the BCP lattice by using strategic templating schemes.

With the use of EBL, we have the capability to control the final self-assembled lattice by designing templates with different parameters. The analysis in the previous sections showed how a given BCP microdomain lattice $i\ j$ could be selected by choice of L_{post}/L and predicted what strain the BCP microdomain lattice experienced when fitting the post lattice. However, it did not address selection between degenerate lattice orientations. For example, two variants of lattice $\langle 2\ 1\rangle$ could be formed when L_{post}/L ~2.6, with orientations of $\theta = +19°$or -19°, as shown in Fig. 5-8A. For a 6-fold symmetric post lattice, no preference for either orientation was observed. However, a preference could be established by adding posts that occupied microdomain lattice sites of only one of the possible variants.

Figure 5-8B shows a defect free BCP microdomain lattice that was formed using a sparse post arrangement that selected for a unique BCP orientation even in the presence of degeneracy. The template was formed by removing posts from the original periodic post lattice and adding posts that matched only the desired BCP $\langle 2\ 1\rangle$ lattice variant, while maintaining the overall post areal density. Templates were also designed to reduce the incidence of one lattice type, for example $\langle 2\ 1\rangle$, compared with a competing orientation such as $\langle 3\ 0\rangle$, by changing the motif present at each post lattice site. Figure 5-8, C and D, shows how this was accomplished by a template whose motif consisted of pairs of posts. A template of single posts showed a gradual transition between $\langle 2\ 1\rangle$ and $\langle 3\ 0\rangle$ lattices as L_{post}/L increases from 2.8 to 3.0. However, with the post pair motif, the $\langle 2\ 1\rangle$ orientation was frustrated and occupied a smaller area fraction of the substrate, even at $L_{\text{post}}/L = 2.6$, where $\langle 2\ 1\rangle$ gave the optimum lattice match with the template.

We found also that the quality of the BCP microdomain lattice is relatively insensitive to the exact shape and size of the posts. Figure 5-8, E to G, shows well-ordered ⟨3 0⟩ lattices formed on three templates with identical period but differing post size and shape: 15-nm diameter, 25-nm diameter, and 45-nm x 25-nm ellipses. This tolerance is useful because it lowers the precision requirements on the template fabrication process.

5.6 Conclusion and future work

We have shown that long range order in BCP can be achieved using an array of HSQ posts that act as pinning centers for the BCP lattice. Although this work was performed using a spherical morphology PS-b-PDMS diblock copolymer, we expect the technique also to be appropriate for block copolymers with perpendicular cylindrical morphology, or lamellar structures. Indeed, the perpendicular cylinder morphology, which lacks the ability to adjust the positions of its domains along the direction normal to the surface, may produce arrays with better placement accuracy than the accuracy demonstrated here, as well as higher aspect ratio features. Well ordered block copolymer arrays may be useful as etch masks in a range of applications, such as patterned recording media, that require periodic nanoscale features covering large areas. This templating approach thus provides a method of combining top-down and bottom-up nanopatterning techniques, where information is placed on the substrate by writing a sparse lattice of posts, and the self-assembling material spontaneously populates the empty spaces on the template with a seamless nanostructured array of determined orientation and lattice spacing.

While forming a BCP lattice with long range order is useful, using BCPs to make controlled arbitrary structures would be even more useful. An example of this implementation in the case of spherical phase BCPs is the local control of BCP orientations and accurate positioning of grain boundaries. Doing so would allow us to come full circle with the control of BCPs: starting from a naturally occurring

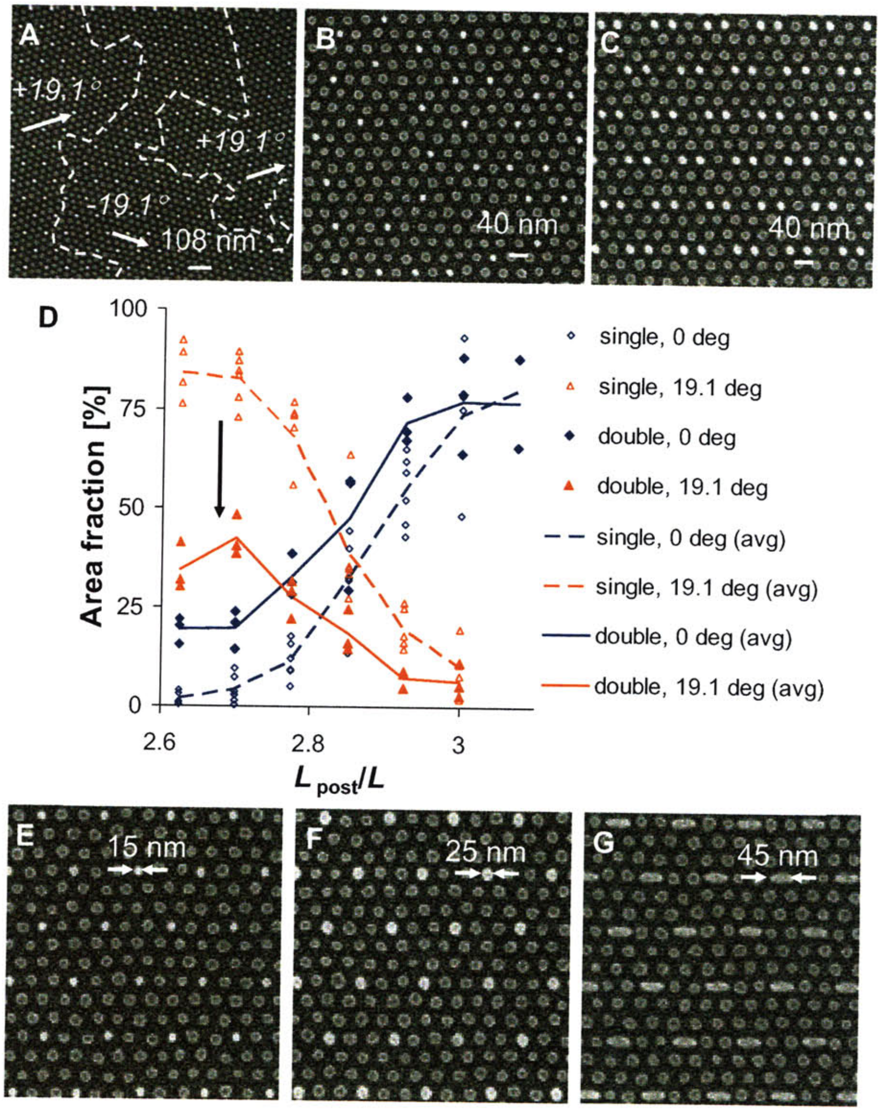

Figure 5-8: (A) SEM image showing two degenerate $\langle 21\rangle$ BCP microdomain lattice orientations (i.e., $+19.1^\circ$and -19.1°) forming on one post lattice. The white dashed lines represent grain boundaries, and the arrows show the grain orientations. The periodic post lattice is commensurate with both orientations. (B) SEM image of a unique BCP microdomain lattice orientation obtained by breaking the periodicity of the post template. (C) A motif consisting of a pair of posts frustrates the formation of BCP lattice orientations other than the $0^\circ\langle 30\rangle$ lattice. (D) A plot of area fraction versus L_{post}/L for two template designs, single-post and double-post lattices. The double-post lattice template frustrates the $19.1^\circ\langle 2\ 1\rangle$ orientation. (E to G) SEM images showing well-ordered BCP $\langle 30\rangle$ arrays guided by pillars of different sizes [(E) and (F)] and shape (G) but with equal center-to-center spacing of 120 nm.

random polycrystalline BCP arrangement, going to a templated single-crystal BCP lattice and finally achieving an engineered polycrystalline structure. We already have some initial results where the template lattice has been locally distorted to achieve locally-varying BCP orientations. In our example, we had circular regions of 30° BCP orientations forming a rectangular array in a background of 0° orientations. By locally varying the template design parameters, either by changing the spacing or rotating the lattice, we can guide the BCP to form polycrystalline structures with grain boundaries exactly where we design them to go. This technology may be useful in designing metamaterials with extremely high grain-boundary density which may be useful in enhancing its mechanical strengths.

Finally, we do not need to be restricted to templating BCPs that only form dot structures. Extending this work to in-plane cylinders or out-of-plane lamellar morphology BCPs will allow us to make line structures that are more versatile than dots. We have recently worked on templating in-plane cylindrical phase PS-PDMS BCP using an array of posts. Using the general idea of commensuration, we show that the orientation and order of the cylinders can be controlled using only an array of posts with varying lattice spacings. The resulting structures form lines instead of dots and have potential for use as interconnects in integrated circuits or high density grating structures.

Chapter 6

Summary and future directions

We have discussed a broad range of topics in this thesis, which started off with the topic of superconducting nanowire single-photon detectors (SNSPDs) and ended with block-copolymer self-assembly. Although a section on conclusion and future directions has been written for each chapter, here we will summarize our work in its entirety and provide an idea of the exciting research that awaits us.

In this thesis, we demonstrated a fabrication process for an integrated optical cavity and anti-reflection coating for the SNSPDs [19, 18]. This optical cavity afforded an increased photon absorption at the detector and, in doing so, increased the detection efficiency by a factor of ~3 to current record values of 57 % (~70 %, unpublished) at 1550 nm wavelengths [21]. From an applications perspective, this drastic improvement in detection efficiency makes SNSPDs suitable for implementation in actual systems, such as in the receiver units in the present Lunar Laser Communications Demonstration program at MIT Lincoln Laboratory.

We are currently working on further improvements in the detection efficiency of the SNSPD. One approach that we have tried is to further enhance the absorptance by increasing the fill-factor of the devices. Increasing the device fill factor from the current value of 45 % to 90 % would allow close to 90 % absorptance. We have recently developed a fabrication process using positive-tone polymethyl methacrylate (PMMA) resist, instead of the negative-tone HSQ, to achieve high fill-factor devices of 90 % while maintaining a nanowire width of 90 nm [119]. However, we found that these high fill-factor devices had unexpectedly suppressed critical currents, and thus did not achieve the high detection efficiency that we hoped for. Nonetheless, this surprising result indicated an interesting unexplored phenomenon in the SNSPDs, i.e. the effect of closely spaced nanowires and tight bends device critical current. Future work will focus on understanding the source of this critical-current suppression, which could potentially be rich in physics.

Another approach to improve the absorptance of the device is by fabricating an optical cavity with a higher Q-factor. This method is currently being pursued at MIT Lincoln Lab where a cavity stack made of Si/SiO_2/NbN/SiO_2/Au promises to have absorptances close to unity with devices with fill-factors of only 50 %. As the substrate material in this case has been switched from sapphire to SiO_2, device performances may be different and the results of this effort will be interesting.

In this thesis, we also presented an electro-thermal model for the SNSPDs [41]. This model was useful in, (1) confirming that Joule heating occurred during each photodetection event, (2) showing that the SNSPD reset time can be shortened by using a resistor in series with the nanowire, and (3) describing the phenomenon of device latching. We also provided analytical solutions to a simplified electro-thermal model which could be valuable in designing SNSPDs that will not latch. Finally, due to availability of better NbN films [58], we now have the ability to fabricate devices with larger active areas with good yield. These large-area detectors are attractive as they are easier to couple light to, but they are also slower due to their larger kinetic inductance. Hence, the method of adding the series resistors to increase the speed of these slower devices will be valuable.

In the second part of the thesis, we showed that high-resolution, sub-10-nm pitch, structures could be made using a robust resist-based electron-beam lithography (EBL) process. This resolution capability was achieved by increasing the contrast of the hydrogen silsesquioxane (HSQ) resist used in our investigations. The contrast was improved by adding salt to an aqueous base developer. The fact that the resist performance could be drastically improved by this a simple modification suggests that there may be potential to further improve on this process once we fully understand the resist mechanism.

Understanding the development mechanism of HSQ will be a major challenge due to the possibly complex chemical reactions that occur during development. However, we will continue to pursue experiments to study the behavior of HSQ. One possible approach is to study the development process in-situ by using a quartz-crystal microbalance (QCM). Such a technique will give us information of development rates as a function of time, which would be useful in developing a model for HSQ behavior.

The ability to reliably pattern structures at sub-10-nm dimensions opens up several exciting possibilities. For instance, in the race for device miniaturization, our high-resolution capability will be useful especially for device prototyping in the research-and-development stage of product development. One such implementation has been done where we fabricated a dense 30-nm-pitch array of suspended strained Si-nanowires as prototype devices for application in gate-all-around n-MOSFETs [120]. Another application for sub-10-nm lithography is in the fabrication of nanoimprint lithography (NIL) molds. While NIL is a high-resolution, high-throughput technique, it has to rely on other lithography techniques for making its imprint mold. Until recently, techniques such as molecular-beam epitaxy (MBE) has been the only approach for achieving sub-10-nm half pitch structures for making molds for NIL [121, 122]. However, these structures were limited to fabricating periodic grating or mesh patterns. With the advent of the high-resolution EBL process, we have now the capability to make arbitrary structures that are well suited for NIL [86]. Several other applications currently being pursued are in the fabrication of (1) test structures for testing graphene nanoribbons, and (2) bit-patterned media for high-density magnetic storage media.

This thesis also presented an example of structures made using the high-resolution process to control the self-assembly of spherical-phase block copolymers [87]. In Chapter 5, we showed that with the EBL-made structures, not only could we achieve ordered periodic dot structures in an otherwise-disordered BCP self-assembled structures, we also achieved an increase in throughput. By patterning only a sparse template with the slow EBL process and relying on the high-throughput BCP process to fill-in the missing structures, we can simultaneously achieve high resolution, throughput, and registration.

One of the remaining challenges in templated self-assembly is in patterning arbitrary structures. Unlike EBL patterning which can pattern arbitrary geometries, BCP self-assembly is limited to patterning only one type of motif depending on its morphology. For instance, with a spherical-morphology BCP, we can only pattern an array of dots, while for a cylindrical morphology, we can only pattern dense lines. We are currently working to achieve near-arbitrary patterning within a certain morphology. For instance, with a cylindrical morphology BCP, short of making the BCP form dots or filled in polygons, we are working to template the BCP into line structures such as nested-Ls, zig-zags, meanders, etc. While similar structures have been demonstrated with BCPs [30], our approach is to achieve these structures with the minimum possible density of guiding structures to significantly increase throughput.

Appendix A

Recipe for SNSPD fabrication

In this appendix, we will provide recipes for making SNSPDs, SNSPDs with integrated cavity, and series Ti resistors with SNSPDs.

A.1 Making SNSPDs

We start with a recipe for making the basic SNSPD.

A.1.1 Getting wafer diced

We have been making SNSPDs on a per-chip basis. Therefore, we typically diced the substrate (NbN on sapphire) into multiple chips each measuring 1 cm square. However, if a large quantities of devices are needed, e.g. if you need to fabricate 10 chips at once, then it probably makes sense to dice the wafer only at the very end to save processing time.

1. Figure out which side of chip has NbN (or other superconducting film you may be working with). This may be tricky as the sapphire substrate is. Two ways to check:
    (a) Measure the resistance of the surface using a multimeter. The NbN film is conductive while the bare sapphire surface is not.

   (b) Compare surface reflectivity of the top and bottom surfaces. The NbN surface is shinier/more reflective.

2. Spin photoresist (Shipley S1813) at 3 krpm on NbN surface to protect film during dicing.

3. Bake wafer on hot plate at 90°Cfor 3 mins.

4. Contact Dan Adams of MTL to get wafer diced in-house email: dan@MTL.MIT.EDU ph: (617) 253-6239, or dice it yourself in the MTL. Use Ultron Systems 1020R UV-sensitive dicing tape with photoresist-coated NbN surface against the adhesive side of the tape. Dice wafer into 1 cm squares.

5. Expose UV-sensitive tape in Tamarack for 1 minute.

6. Label chips according to standard convention (see previously diced wafers or Ref [58] for example) with a lab marker on the dicing tape (not on chip itself).

A.1.2 Making contact pads

Contact pads are needed for making electrical connection to the nanowires.

1. Only when a specific chip is needed: cut the dicing tape around the desired chip using a razor blade to remove the desired chip(s).

2. Remove dicing tape from desired chip by firmly holding chip with tweezers and peeling back tape slowly with a second set of tweezers.

3. Rinse chip with acetone, methanol, isopropyl alcohol and dry with N_2.

4. Inspect chip in microscope to ensure samples are clean (ideally no more than 1 or 2 specks of particles). If samples still appear dirty, repeat previous step.

5. Spin on photoresist S1813 (dispense 3 drops on sample) at 6 krpm for 1 minute. Thickness of resist $\sim 1\,\mu\text{m}$.

6. Bake at 90°C for 3 minutes on hotplate.

7. Clean photomask using acetone, methanol, isopropanol, DI and blow dry.
8. Expose contact pads in Tamarack. For intensities of 3.3 mW/cm^2, expose for 20 s.
9. Dip chips in chlorobenzene for 15 mins. This creates an overhang structure in the resist profile that aids liftoff (not necessary if resist sidewalls are perfectly vertical but since we don't check this everytime, this step is valuable).
10. Remove chlorobenzene from surface of the chip by blowdrying using N_2 gun.
11. Develop in Microposit 352 NaOH developer for 3 mins.
12. Rinse in DI and blow dry.
13. Inspect chip in optical microscope.
14. Mount samples for evaporation of 10 nm Ti followed by 50 nm Au.
15. After evaporation, dip chips in hot N-methyl pyrolidinone (NMP) kept at 90C. **Warning**: NMP is a flamable solvent. Follow safety precautions when handling this. e.g. Heat it in a hot water bath.
16. Observe liftoff to see if completed. This may take about 30 s to 1 min if liftoff is successful.
17. Remove chip from hot NMP and squirt acetone on sample surface over another glassware. Observe the flow of acetone on chip surface. If acetone flows smoothly in a radial direction from the squirt stream, then liftoff was good. If acetone flow appears obstructed, i.e. if it appears to flow around a particle, then there is residual metal that was not completely lifted off. Remove this residual metal by repeatedly squirting short streams of acetone directly at the speck. The initial impact of acetone stream is more effective at removing the speck than a continuous flow.
18. Rinse in running DI water (i.e. under tap) for half a minute and blow dry with N_2 gun.

19. Inspect sample in optical microscope.
20. Use Dektak surface profiler to measure total Ti/Au thickness.

A.1.3 Making meanders

Once contact pads are made, the nanowire meanders can be patterned using electron-beam lithography and HSQ.

1. Take bottle of HSQ from fridge to warm up to room temperature. Usually leave it out for 1 hr before spin.
2. Dip chip in 25 % TMAH for 4 mins, rinse in DI and blowdry to remove contamination left over from photoresist liftoff. This step has helped avoid adhesion problems with HSQ in all cases except one.
3. Use plastic pipettes to dispense HSQ. Spin on HSQ (at at 4.5 krpm for 1:1 FOx-14:MiBK dilution; at 5.5 krpm for XR-1541 6 % solids) on dummy silicon wafer and measure thickness in ellipsometer. Thickness should be close to 100 nm.
4. Spin HSQ on chips. Avoid long delays (2 days max) between spin and exposure. Remember to keep HSQ in fridge after use.
5. Expose meanders on Raith at 30 kV using appropriate dose. (Run a dose matrix for new patterns or if new bottle of HSQ is used or if it's been more than two months since last dose matrix was done.)
6. Develop sample in 25 % TMAH for 4 mins.
7. Rinse by dipping in DI for a minute with manual agitation and under running DI for another minute. Blowdry with N_2 gun.
8. Inspect meander structures in SEM.

A.1.4 Etching

Once patterns are defined in HSQ, they can be transferred into the underlying NbN by the following etching step.

1. Prior to etching, do a trial run, without the chip, using HSQ_Sld.PRC process to ensure power and voltage levels are 100 W and 110 V respectively. If voltage is too low (i.e. < 80 V), do a cleaning step.
2. Repeat previous step until etching parameters are where you want it to be.
3. Insert actual chip into chamber and run etch for 1 minute and 40 seconds.
4. Inspect chip after RIE to check that etch is complete by looking for clear (transparent) areas where NbN was unmasked or by measuring the resistance of detector structures.
5. Inspect devices in SEM.

A.2 Making integrated optical cavity and anti-reflection coating

Here is the recipe for making an integrated optical cavity on top of the detectors and an anti-reflection coating on the bottom surface of the substrate.

A.2.1 Integrated optical cavity

1. Calculate the required HSQ dielectric thickness for the cavity. For 1.55 μm wavelength photons, a total cavity thickness of 205 nm is required.
2. Measure remaining HSQ thickness on the nanowires using a Dektak or AFM. Thickness should be $\sim$45 nm. For this remaining HSQ thickness, an additional 160 nm (205 - 45 nm) of HSQ is required. Add an extra $\sim$20 nm to this thickness to compensate for resist shrinkage during exposure, systematic variation caused

by spin-coating over the remaining HSQ topography, and the slight resist loss during development. So instead of targeting for 160 nm, target for 180 nm.

3. Use HSQ formulated as Fox-14 dilution from Dow Corning for the cavity dielectric. Warm bottle up from its storage in the fridge to room temperature before use.
4. Spin on Fox-14 HSQ on a test Si wafer and adjust spin speed to achieve this target thickness. Typically 7.5 krpm spin speed results in ~180 nm thickness.
5. Spin on Fox-14 HSQ on actual chip.
6. Soft-bake resist at 90°C for 5 mins to drive out excess solvents.
7. Spin on aquaSAVE (Mitsubishi Rayon America Inc.) a conductive spin-on polymer at 3.5 krpm to prevent charging during the subsequent electron-beam patterning.
8. Use the Raith 150 at 10 kV to define the cavity dielectric by exposing large 40 μm×40 μm square areas centered on the detector active areas at a dose of 600 μC/cm^2. Use a large aperture size (e.g. 60 μm or 120 μm) to decrease exposure times.
9. Develop sample in 25 % TMAH for 4 mins followed by rinse in DI water and blowdry.
10. Measure the height of the dielectric in Dektak surface profilometer.
11. Trim the dielectric thickness, if necessary, using the etch process in subsection A.1.4. Etch rate of HSQ is ~15 nm/min with this process.
12. Spin on photoresist S1813 at 6 krpm for 1 minute. Thickness of resist ~1 μm.
13. Bake at 90°C for 3 minutes on hotplate.
14. Mount sample onto the unpolished back of a Si handle wafer using the following process. Spin on photoresist S1813 at 1.5 krpm on the backside of the Si wafer

for 10 s. Place chip onto the photoresist coated handle wafer and bake both together at 90°C for 10 mins.

15. Expose photoresist in a Karl Suss MJB3 contact aligner high resolution model in the Experimental Materials Laboratory (EML) at MIT. Remove UV filter. For the typical UV power-source setting of 3.5 (possibly in mW/cm^2), expose for 20 s.
16. Follow procedure from subsection A.1.2 from item 9 to 13.
17. Mount samples for evaporation 1 nm Ti 120 nm Au.
18. Follow procedure from subsection A.1.2 from item 15 to perform liftoff.

A.2.2 Anti-reflection coating (ARC)

This is the process for coating the bottom surface of the substrate with a HSQ ARC. For 1.55 µm wavelength, the optimal ARC thickness is ~277 nm.

1. To prevent damage to devices on the top surface, mount sample face down onto a handle Si wafer with a drop of S1813 photoresist.
2. Spin on Fox-14 HSQ on a test Si wafer to target a thickness of 277 nm. Target spin speed = 2.8 krpm.
3. Spin Fox-14 HSQ on actual sample.
4. Bake on hot plate for 20 min at 90°C.
5. Place sample and mount in a Technics PlanarEtch II oxygen plasma asher and ash for 10 mins at 100 W power, and 0.4 Torr pressure with 80 % He/ 20 % O_2 gas.
6. Release sample from handle wafer by soaking in acetone.

A.3 Fabricating on-chip series resistors

This section contains the recipe for fabricating Ti on-chip resistors in series with the NbN meanders.

1. To prevent the underlying NbN from shorting out the series resistors, NbN in areas where the series resistors will be patterned need to be etched out. A photomask needs to be specially designed for this purpose. An example of a photomask made for this is the mask designed for the latching experiment (dated 070925 labeled NbN etch on under the photomask pattern on the mask itself). Then follow procedures from subsection A.1.2 from item 1 to 8.

2. No chlorobenzene soak is necessary as we do not need to do liftoff. Develop in Microposit 352 NaOH developer for 3 mins.

3. Rinse in DI and blow dry.

4. Inspect chip in optical microscope.

5. Etch sample using the procedure from subsection A.1.4 from item 1 to 4.

6. Inspect that etched regions are completely cleared out. You can also measure that the completely removed NbN areas in the frame around the chip is no longer conductive.

7. Remove the photoresist etch mask by soaking sample in NMP at room temperature in a beaker placed in an ultrasonic agitator bath. Agitate for 5 mins and inspect in optical microscope. If some photoresist remains, scrub the surface of the sample with a q-tip soaked in acetone. Then rinse in DI water and blowdry.

8. Follow procedures from subsection A.2.1 from item 12 to 15 to spin on and expose regions in the photoresist for the Ti resistor deposition.

9. Follow procedure from subsection A.1.2 from item 9 to 13 for photoresist development.

10. Mount samples for evaporation 90 nm Ti. This thickness of Ti results in a sheet resistance of about 50 Ω per square for the resistors. **Note:** This is only a rough estimate as the resistance of the deposited Ti may also vary from run to run.
11. Follow procedure from subsection A.1.2 from item 15 to perform liftoff.
12. Proceed to put on the metal contact pads following procedure from subsection A.1.2 and pattern the meanders following procedure from subsection A.1.3.

Appendix B

Kinetic inductance dependence on device current

This is an appendix to Section 3.3.2 where we discussed the voltage developed across the nanowire due to the non-constant kinetic inductance L_{k} of the nanowire. The kinetic inductance was not constant because it depended on the density of superconducting charge carriers, i.e. Cooper pairs, which decreased with increasing current through the nanowire. Due to this non-constant kinetic inductance L_{k}, the voltage V developed is given by the following:

$$V = L_{\mathrm{k}}\frac{\mathrm{d}I}{\mathrm{d}t} + I\frac{\mathrm{d}L_{\mathrm{k}}}{\mathrm{d}t} \tag{B.1}$$

For the sake of simplicity, we neglected the second term in our calculations. Here, we will investigate if this simplification is ok. It turns out that this second term becomes prominent for device currents close to I_{c}.

To investigate the significance of the second term, we compare the magnitudes of both terms by taking the ratio of the second term to the first term. This ratio, which we shall denote as $\Re$, is given by the following equation:

$$\Re = \frac{L_\mathrm{k}\mathrm{d}I/\mathrm{d}t}{I\mathrm{d}L_\mathrm{k}/\mathrm{d}t} \tag{B.2}$$

$$= \frac{L_\mathrm{k}}{I}\frac{\mathrm{d}I}{\mathrm{d}L_\mathrm{k}} \tag{B.3}$$

We will come back to equation B.8 later. For now, we will explain the kinetic inductance dependence on device current. The kinetic inductance of a nanowire of length l, and cross-sectional area A is

$$L_\mathrm{k} = \frac{m^*}{n^* q^2}\frac{l}{A} \tag{B.4}$$

where m^* is the effective mass of the superconducting charge carrier, i.e. the Cooper pair, which has twice the mass of an electron, n^* is the number density of Cooper pairs, i.e. the number of Cooper pairs per unit volume, and q is the charge of the Cooper pair, which is also twice that of an electron [123].

To relate L_k to device current, we start with the Ginzburg-Landau calculation of the critical current of the nanowire, which is given by

$$I_\mathrm{c} = \frac{\Phi_o A}{3\sqrt{3}\pi\mu_o\lambda^2\xi} \tag{B.5}$$

where Φ_o is the magnetic flux quantum, μ_o is the permeability of free space, λ is the material-dependent magnetic penetration depth and ξ is the Ginzburg-Landau material-dependent superconducting coherence length. A superconducting device current $\leq I_\mathrm{c}$ is given by

$$I = \frac{\Phi_o A}{2\pi\mu_o\lambda^2\xi}|f|^2\sqrt{1-|f|^2} \tag{B.6}$$

where $|f|^2 = n^*/n_o^*$ is the square magnitude of the superconducting order parameter in which n_o^* is the Cooper pair density at zero current flow. Combining this expression with equation B.4, we obtain

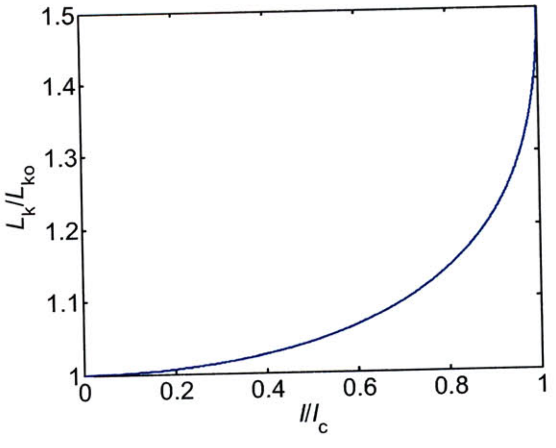

Figure B-1: Plot of the kinetic inductance L_k dependence on the current through the nanowire I.

$$|f|^2 = n^*/n_o^* = L_\mathrm{ko}/L_\mathrm{k} = 1/l_\mathrm{k} \tag{B.7}$$

where L_ko is the kinetic inductance of the nanowire at zero current flow and l_k is the ratio of the the kinetic inductance, at current I, to L_ko.

Taking the ratio of equation B.6 to equation B.5 results in

$$i = I/I_\mathrm{c} = \sqrt{\frac{27}{4}(|f|^4 - |f|^6)} \tag{B.8}$$

Finally, substituting equation (B.7) into equation (B.8) results in an equation that relates the kinetic inductance to the nanowire current in the following expression:

$$i = \sqrt{\frac{27}{4}(\frac{1}{l_\mathrm{k}^2} - \frac{1}{l_\mathrm{k}^3})} \tag{B.9}$$

We see from solving equation (B.9) that when $i = 1$, i.e. when $I = I_\mathrm{c}$, $L_\mathrm{k} = 1.5L_\mathrm{ko}$ which means that the kinetic inductance can increase by 50 % of its value at zero current. A plot of L_k vs I/I_c is shown in Fig. B-1.

Now back to equation (B.8),

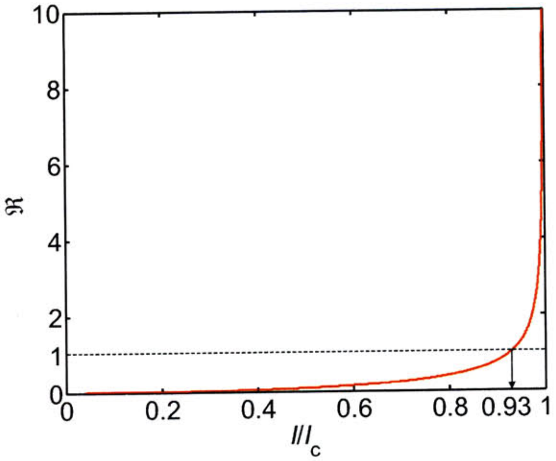

Figure B-2: Plot of $\Re$, the ratio of $L_\mathrm{k}\mathrm{d}I/\mathrm{d}t$ to $I\mathrm{d}L_\mathrm{k}/\mathrm{d}t$ as a function of current through the nanowire I. For values of $I < I_\mathrm{c}$, the $L_\mathrm{k}\mathrm{d}I/\mathrm{d}t$ term dominates, though the $I\mathrm{d}L_\mathrm{k}/\mathrm{d}t$ is also not negligible until $I < 0.5I_\mathrm{c}$ where it decreases to less than 10% of $L_\mathrm{k}\mathrm{d}I/\mathrm{d}t$.

$$\Re = \frac{L_\mathrm{k}}{I}\frac{\mathrm{d}I}{\mathrm{d}L_\mathrm{k}} \tag{B.10}$$

$$= \frac{l_\mathrm{k}}{i}\frac{\mathrm{d}i}{\mathrm{d}l_\mathrm{k}} \tag{B.11}$$

Differentiating equation (B.9) with respect to l_k and substituting into equation (B.11) results in the following equation:

$$\Re = \frac{l_\mathrm{k}}{i}\frac{\mathrm{d}i}{\mathrm{d}l_\mathrm{k}} = \frac{\sqrt{27}}{4i}\frac{3-2l_\mathrm{k}}{l_\mathrm{k}\sqrt{l_\mathrm{k}^2 - l_\mathrm{k}}} \tag{B.12}$$

A plot of $\Re$ in equation (B.12) as a function of I/I_c is shown in Fig. B-2. In this plot we see that the $I\mathrm{d}L_\mathrm{k}/\mathrm{d}t$ term can be significantly larger than the $L_\mathrm{k}\mathrm{d}I/\mathrm{d}t$ term, for currents very close to the critical current. For $I/I_\mathrm{c} < 0.9$, $\Re$ becomes less than unity. However the $I\mathrm{d}L_\mathrm{k}/\mathrm{d}t$ becomes negligibly (less than 10%) small when $I/I_\mathrm{c} < 0.5$. Hence, this term should be included in future calculations to improve the accuracy of the electro-thermal model.

Bibliography

[1] G. Gol'tsman, O. Okunev, G. Chulkova, A. Lipatov, A. Dzardanov, K. Smirnov, A. Semenov, B. Voronov, C. Williams, and R. Sobolewski. Fabrication and properties of an ultrafast nbn hot-electron single-photon detector. *IEEE Transactions on Applied Superconductivity*, 11(1):574–577, 2001.

[2] G. N. Gol'tsman, O. Okunev, G. Chulkova, A. Lipatov, A. Semenov, K. Smirnov, B. Voronov, A. Dzardanov, C. Williams, and R. Sobolewski. Picosecond superconducting single-photon optical detector. *Applied Physics Letters*, 79(6):705–707, 2001.

[3] A. M. Kadin and M. W. Johnson. Nonequilibrium photon-induced hotspot: A new mechanism for photodetection in ultrathin metallic films. *Applied Physics Letters*, 69(25):3938–3940, 1996.

[4] M. A. Albota and E. Dauler. Single photon detection of degenerate photon pairs at 1.55 mu m from a periodically poled lithium niobate parametric downconverter. *Journal of Modern Optics*, 51(9-10):1417–1432, 2004.

[5] W. G. Mcmullan, S. Charbonneau, and M. L. W. Thewalt. Simultaneous subnanosecond timing information and 2d spatial information from imaging photomultiplier tubes. *Review of Scientific Instruments*, 58(9):1626–1628, 1987.

[6] D. Rosenberg, A. E. Lita, A. J. Miller, S. Nam, and R. E. Schwall. Performance of photon-number resolving transition-edge sensors with integrated 1550 nm resonant cavities. *IEEE Transactions on Applied Superconductivity*, 15(2):575–578, 2005.

[7] D. Rosenberg, A. E. Lita, A. J. Miller, and S. W. Nam. Noise-free high-efficiency photon-number-resolving detectors. *Physical Review A*, 71(6):–, 2005.

[8] P. K. Day, H. G. LeDuc, B. A. Mazin, A. Vayonakis, and J. Zmuidzinas. A broadband superconducting detector suitable for use in large arrays. *Nature*, 425(6960):817–821, 2003.

[9] F. Stellari and P. L. Song. Testing of ultra low voltage vlsi chips using the superconducting single-photon detector (sspd). *Microelectronics Reliability*, 44(9-11):1663–1668, 2004.

[10] F. Stellari, P. L. Song, J. C. Tsang, M. K. McManus, and M. B. Ketchen. Testing and diagnostics of cmos circuits using light emission from off-state leakage current. *IEEE Transactions on Electron Devices*, 51(9):1455–1462, 2004.

[11] J. Zhang, N. Boiadjieva, G. Chulkova, H. Deslandes, G. N. Gol'tsman, A. Korneev, P. Kouminov, A. Leibowitz, W. Lo, R. Malinsky, O. Okunev, A. Pearlman, W. Slysz, K. Smirnov, C. Tsao, A. Verevkin, B. Voronov, K. Wilsher, and R. Sobolewski. Noninvasive cmos circuit testing with nbn superconducting single-photon detectors. *Electronics Letters*, 39(14):1086–1088, 2003.

[12] G. Brassard and C. H. Bennett. Quantum cryptography. *Lecture Notes in Computer Science*, 325:79–90, 1988.

[13] H. Takesue, S. W. Nam, Q. Zhang, R. H. Hadfield, T. Honjo, K. Tamaki, and Y. Yamamoto. Quantum key distribution over a 40-db channel loss using superconducting single-photon detectors. *Nature Photonics*, 1(6):343–348, 2007.

[14] R. H. Hadfield, M. J. Stevens, R. P. Mirin, and S. W. Nam. Single-photon source characterization with twin infrared-sensitive superconducting single-photon detectors. *Journal of Applied Physics*, 101(10):–, 2007.

[15] D. M. Boroson, R. S. Bondurant, and J. J. Scozzafava. Overview of high-rate deep-space laser communications options. *in Free-Space Laser Communication Technologies XVI, Proc. SPIE*, 5338:37–49, 2004.

[16] B. S. Robinson, A. J. Kerman, E. A. Dauler, R. O. Barron, D. O. Caplan, M. L. Stevens, J. J. Carney, S. A. Hamilton, J. K. W. Yang, and K. K. Berggren. 781 mbit/s photon-counting optical communications using a superconducting nanowire detector. *Optics Letters*, 31(4):444–446, 2006.

[17] G. N. Gol'tsman, K. Smirnov, P. Kouminov, B. Voronov, N. Kaurova, V. Drakinsky, J. Zhang, A. Verevkin, and R. Sobolewski. Fabrication, of nanostructured superconducting single-photon detectors. *IEEE Transactions on Applied Superconductivity*, 13(2):192–195, 2003.

[18] J. K. W. Yang. *Fabrication of Superconducting Nanowire Single Photon Detectors.* S.m. thesis, Massachusetts Institute of Technology, 2005.

[19] J. K. W. Yang, E. Dauler, A. Ferri, A. Pearlman, A. Verevkin, G. Goltsman, B. Voronov, R. Sobolewski, W.E. Keicher, and K.K. Berggren. Fabrication development for nanowire ghz-counting-rate, single photon detectors. *IEEE Transactions on Applied Superconductivity*, 15(2):626–630, 2005.

[20] A. Korneev, V. Matvienko, O. Minaeva, I. Milostnaya, I. Rubtsova, G. Chulkova, K. Smirnov, V. Voronov, G. Gol'tsman, W. Slysz, A. Pearlman, A. Verevkin, and R. Sobolewski. Quantum efficiency and noise equivalent power of nanostructured, nbn, single-photon detectors in the wavelength range from visible to infrared. *Ieee Transactions on Applied Superconductivity*, 15(2):571–574, 2005.

[21] K. M. Rosfjord, J. K. W. Yang, E. A. Dauler, A. J. Kerman, V. Anant, B. M. Voronov, G. N. Gol'tsman, and K. K. Berggren. Nanowire single-photon detector with an integrated optical cavity and anti- reflection coating. *Optics Express*, 14(2):527–534, 2006.

[22] E. A. Dauler, B. S. Robinson, A. J. Kerman, J. K. W. Yang, K. M. Rosfjord, V. Anant, B. Voronov, G. Gol'tsman, and K. K. Berggren. Multi-element superconducting nanowire single-photon detector. *IEEE Transactions on Applied Superconductivity*, 17(2):279–284, 2007.

[23] A. J. Kerman, E. A. Dauler, J. K. W. Yang, K. M. Rosfjord, V. Anant, K. K. Berggren, G. N. Gol'tsman, and B. M. Voronov. Constriction-limited detection efficiency of superconducting nanowire single-photon detectors. *Applied Physics Letters*, 90(10):101110, 2007.

[24] T. H. P. Chang, M. Mankos, K. Y. Lee, and L. P. Muray. Multiple electron-beam lithography. *Microelectronic Engineering*, 57-8:117–135, 2001.

[25] P. Kruit, S. Steenbrink, R. Jager, and M. Wieland. Optimum dose for shot noise limited cd uniformity in electron-beam lithography. *Journal of Vacuum Science & Technology B*, 22(6):2948–2955, 2004.

[26] T. Thurn-Albrecht, J. DeRouchey, T. P. Russell, and H. M. Jaeger. Overcoming interfacial interactions with electric fields. *Macromolecules*, 33(9):3250–3253, 2000.

[27] C. De Rosa, C. Park, E. L. Thomas, and B. Lotz. Microdomain patterns from directional eutectic solidification and epitaxy. *Nature*, 405(6785):433–437, 2000.

[28] R. A. Segalman, H. Yokoyama, and E. J. Kramer. Graphoepitaxy of spherical domain block copolymer films. *Advanced Materials*, 13(15):1152–+, 2001.

[29] J. Y. Cheng, C. A. Ross, V. Z. H. Chan, E. L. Thomas, R. G. H. Lammertink, and G. J. Vancso. Formation of a cobalt magnetic dot array via block copolymer lithography. *Advanced Materials*, 13(15):1174, 2001.

[30] S. O. Kim, H. H. Solak, M. P. Stoykovich, N. J. Ferrier, J. J. de Pablo, and P. F. Nealey. Epitaxial self-assembly of block copolymers on lithographically defined nanopatterned substrates. *Nature*, 424(6947):411–414, 2003.

[31] J. Zhang, W. Slysz, A. Verevkin, O. Okunev, G. Chulkova, A. Korneev, A. Lipatov, G. N. Gol'tsman, and R. Sobolewski. Response time characterization of nbn superconducting single-photon detectors. *IEEE Transactions on Applied Superconductivity*, 13(2):180–183, 2003.

[32] A. J. Kerman, E. A. Dauler, W. E. Keicher, J. K. W. Yang, K. K. Berggren, G. Gol'tsman, and B. Voronov. Kinetic-inductance-limited reset time of superconducting nanowire photon counters. *Applied Physics Letters*, 88(11):111116, 2006.

[33] J. Kitaygorsky, J. Zhang, A. Verevkin, A. Sergeev, A. Korneev, V. Matvienko, P. Kouminov, K. Smirnov, B. Voronov, G. Gol'tsman, and R. Sobolewski. Origin of dark counts in nanostructured nbn single-photon detectors. *IEEE Transactions on Applied Superconductivity*, 15(2):545–548, 2005.

[34] I. Milostnaya, A. Korneev, I. Rubtsova, V. Seleznev, O. Minaeva, G. Chulkova, O. Okunev, B. Voronov, K. Smirnov, G. Gol'tsman, W. Sysz, M. Wegrzecki, M. Guziewicz, J. Bar, M. Gorska, A. Pearlman, J. Kitaygorsky, A. Cross, and R. Sobolewski. Superconducting single-photon detectors designed for operation at 1.55-μm telecommunication wavelength. In Journal of Physics: Conference Series, editor, *7th European Conference on Applied Superconductivity*, volume 43, pages 1334–1337. Institute of Physics Publishing, 2006.

[35] V. Anant, A. J. Kerman, E. A. Dauler, J. K. W. Yang, K. M. Rosfjord, and K. K. Berggren. Optical properties of superconducting nanowire single-photon detectors. *Optics Express*, 16(14):10750–10761, 2008.

[36] *Handbook of optical constants of solids.* Academic Press, 1985.

[37] W. Slysz, M. W. Grzecki, J. Bar, P. Grabiec, M. Gorska, V. Zwiller, C. Latta, P. Bohi, A. J. Pearlman, A. S. Cross, D. Pan, J. Kitaygorsky, I. Komissarov, A. Verevkin, I. Milostnaya, A. Korneev, O. Minayeva, G. Chulkova, K. Smirnov, B. Voronov, G. N. Gol'tsman, and R. Sobolewski. Fibre-coupled, single photon detector based on nbn superconducting nanostructures for quantum communications. *Journal of Modern Optics*, 54(2-3):315–326, 2007.

[38] R. Sobolewski, A. Verevkin, G. N. Gol'tsman, A. Lipatov, and K. Wilsher. Ultrafast superconducting single-photon optical detectors and their applications. *IEEE Transactions on Applied Superconductivity*, 13(2):1151–1157, 2003.

[39] Joel K. W. Yang and Karl K. Berggren. Using high-contrast salty development of hydrogen silsesquioxane for sub-10-nm half-pitch lithography. *Journal of Vacuum Science & Technology*, 25(6):2025–2029, 2007.

[40] A.J. Kerman, J.K.W. Yang, R.J. Molnar, E. A. Dauler, and K.K. Berggren. Electrothermal feedback in superconducting nanowire single-photon detectors, 2008.

[41] J. K. W. Yang, A. J. Kerman, E. A. Dauler, V. Anant, K. M. Rosfjord, and K. K. Berggren. Modeling the electrical and thermal response of superconducting nanowire single-photon detectors. *Applied Superconductivity, IEEE Transactions on*, 17(2):581, 2007.

[42] W. J. Skocpol, M. R. Beasley, and M. Tinkham. Self-heating hotspots in superconducting thin-film microbridges. *Journal of Applied Physics*, 45(9):4054–4066, 1974.

[43] A. D. Semenov, G. N. Gol'tsman, and A. A. Korneev. Quantum detection by current carrying superconducting film. *Physica C*, 351(4):349–356, 2001.

[44] A. V. Gurevich and R. G. Mints. Self-heating in normal metals and superconductors. *Reviews of Modern Physics*, 59(4):941–999, 1987.

[45] S. I. Anisimov, Kapeliov.Bl, and T. L. Perelman. Electron-emission from surface of metals induced by ultrashort laser pulses. *Zhurnal Eksperimentalnoi I Teoreticheskoi Fiziki*, 66(2):776–781, 1974.

[46] K. S. Il'in, M. Lindgren, M. Currie, A. D. Semenov, G. N. Gol'tsman, R. Sobolewski, S. I. Cherednichenko, and E. M. Gershenzon. Picosecond hot-electron energy relaxation in nbn superconducting photodetectors. *Applied Physics Letters*, 76(19):2752–2754, 2000.

[47] T. Q. Qiu and C. L. Tien. Heat-transfer mechanisms during short-pulse laser-heating of metals. *Journal of Heat Transfer-Transactions of the Asme*, 115(4):835–841, 1993.

[48] P. M. Norris, A. P. Caffrey, R. J. Stevens, J. M. Klopf, J. T. McLeskey, and A. N. Smith. Femtosecond pump-probe nondestructive examination of materials (invited). *Review of Scientific Instruments*, 74(1):400–406, 2003.

[49] Allen Rothwarf and B. N. Taylor. Measurement of recombination lifetimes in superconductors. *Physical Review Letters*, 19(1):27, 1967.

[50] Y. P. Gousev, G. N. Goltsman, A. D. Semenov, E. M. Gershenzon, R. S. Nebosis, M. A. Heusinger, and K. F. Renk. Broad-band ultrafast superconducting nbn detector for electromagnetic-radiation. *Journal of Applied Physics*, 75(7):3695–3697, 1994.

[51] Michael Tinkham. *Introduction to superconductivity.* International series in pure and applied physics. McGraw Hill, New York, 2nd edition, 1996.

[52] J. Bardeen, L. N. Cooper, and J. R. Schrieffer. Theory of superconductivity. *Physical Review*, 108(5):1175, 1957.

[53] E. T. Swartz and R. O. Pohl. Thermal-boundary resistance. *Reviews of Modern Physics*, 61(3):605–668, 1989.

[54] S. Sahling, J. Engert, A. Gladun, and R. Knoner. The thermal-boundary resistance between sapphire and aluminum mono-crystals at low-temperature. *Journal of Low Temperature Physics*, 45(5-6):457–469, 1981.

[55] M. Tinkham, J. U. Free, C. N. Lau, and N. Markovic. Hysteretic i-v curves of superconducting nanowires. *Physical Review B*, 68(13):134515, 2003.

[56] Allan W. Bjerkaas, D. M. Ginsberg, and B. J. Mrstik. Electronic thermal conductivity of superconducting thin films of indium-manganese alloys. *Physical Review B*, 5(3):854, 1972.

[57] R. H. Hadfield, A. J. Miller, S. W. Nam, R. L. Kautz, and R. E. Schwall. Low-frequency phase locking in high-inductance superconducting nanowires. *Applied Physics Letters*, 87(20):–, 2005.

[58] E. A. Dauler. *Multi-element Superconducting Nanowire Single Photon Detectors.* Phd, Massachusetts Institute of Technology, 2008.

[59] H. Namatsu, Y. Takahashi, K. Yamazaki, T. Yamaguchi, M. Nagase, and K. Kurihara. Three-dimensional siloxane resist for the formation of nanopatterns with minimum linewidth fluctuations. *Journal of Vacuum Science & Technology B*, 16(1):69–76, 1998.

[60] H. Namatsu. Supercritical resist drying for isolated nanoline formation. *Journal of Vacuum Science & Technology B*, 19(6):2709–2712, 2001.

[61] B. E. Maile, W. Henschel, H. Kurz, B. Rienks, R. Polman, and P. Kaars. Sub-10 nm linewidth and overlay performance achieved with a fine-tuned ebpg-5000 tfe electron beam lithography system. *Japanese Journal of Applied Physics Part 1-Regular Papers Short Notes & Review Papers*, 39(12B):6836–6842, 2000.

[62] A. E. Grigorescu, M. C. van der Krogt, C. W. Hagen, and P. Kruit. 10 nm lines and spaces written in hsq, using electron beam lithography. *Microelectronic Engineering*, 84(5-8):822, 2007.

[63] M. J. Word, I. Adesida, and P. R. Berger. Nanometer-period gratings in hydrogen silsesquioxane fabricated by electron beam lithography. *Journal of Vacuum Science & Technology B*, 21(6):L12–L15, 2003.

[64] W. D. Hinsberg and M. L. Gutierrez. Effect of developer composition on photoresist performance. *Proceedings of the Society of Photo-Optical Instrumentation Engineers*, 469:57–64, 1984.

[65] I. B. Baek, J. H. Yang, W. J. Cho, C. G. Ahn, K. Im, and S. Lee. Electron beam lithography patterning of sub-10 nm line using hydrogen silsesquioxane for nanoscale device applications. *Journal of Vacuum Science & Technology B*, 23(6):3120–3123, 2005.

[66] W. Chen and H. Ahmed. Fabrication of 5-7 nm wide etched lines in silicon using 100 kev electron-beam lithography and polymethylmethacrylate resist. *Applied Physics Letters*, 62(13):1499–1501, 1993.

[67] A. N. Broers, W. W. Molzen, J. J. Cuomo, and N. D. Wittels. Electron-beam fabrication of 80-aa metal structures. *Applied Physics Letters*, 29(9):596, 1976.

[68] S. Yasin, D. G. Hasko, and H. Ahmed. Fabrication of ¡ 5 nm width lines in poly(methylmethacrylate) resist using a water: isopropyl alcohol developer and ultrasonically-assisted development. *Applied Physics Letters*, 78(18):2760–2762, 2001.

[69] M. Ishida, J. I. Fujita, T. Ogura, Y. Ochiai, E. Ohshima, and J. Momoda. Sub-10-nm-scale lithography using p-chloromethyl-methoxy-calix[4]arene resist. *Japanese Journal of Applied Physics Part 1-Regular Papers Short Notes & Review Papers*, 42(6B):3913–3916, 2003.

[70] H. Hiroshima, S. Okayama, M. Ogura, M. Komuro, H. Nakazawa, Y. Nakagawa, K. Ohi, and K. Tanaka. Nanobeam process system: An ultrahigh vacuum electron beam lithography system with 3 nm probe size. *Journal of Vacuum Science & Technology B*, 13(6):2514–2517, 1995.

[71] M. D. Fischbein and M. Drndi. Sub-10 nm device fabrication in a transmission electron microscope. *Nano Lett.*, 7(5):1329–1337, 2007.

[72] D. Lauvernier, Jean-Pierre Vilcot, Marc Francois, and Didier Decoster. Optimization of hsq resist e-beam processing technique on gaas material. *Microelectronic Engineering*, 75(2):177, 2004.

[73] Y. F. Chen, H. F. Yang, and Z. Cui. Effects of developing conditions on the contrast and sensitivity of hydrogen silsesquioxane. *Microelectronic Engineering*, 83(4-9):1119–1123, 2006.

[74] W. Henschel, Y. M. Georgiev, and H. Kurz. Study of a high contrast process for hydrogen silsesquioxane as a negative tone electron beam resist. *Journal of Vacuum Science & Technology B*, 21(5):2018–2025, 2003.

[75] P. C. Tsiartas, L. W. Flanagin, C. L. Henderson, W. D. Hinsberg, I. C. Sanchez, R. T. Bonnecaze, and C. G. Willson. The mechanism of phenolic polymer dissolution: A new perspective. *Macromolecules*, 30(16):4656–4664, 1997.

[76] M. S. Kim and A. Reiser. Percolation view of novolak dissolution.7. the effect of salts. *Macromolecules*, 30(13):3860–3866, 1997.

[77] J. K. W. Yang, V. Anant, and K. K. Berggren. Enhancing etch resistance of hydrogen slisesquioxane via postdevelop electron curing. *Journal of Vacuum Science & Technology B*, 24(6):3157–3161, 2006.

[78] A. Reiser, J. P. Huang, X. He, T. F. Yeh, S. Jha, H. Y. Shih, M. S. Kim, Y. K. Han, and K. Yan. The molecular mechanism of novolak-diazonaphthoquinone resists. *European Polymer Journal*, 38(4):619–629, 2002.

[79] A. Reiser, Z. L. Yan, Y. K. Han, and M. S. Kim. Navolak-diazonaphthoquinone resists: The central role of phenolic strings. *Journal of Vacuum Science & Technology B*, 18(3):1288–1293, 2000.

[80] A. Reiser. The molecular mechanism of novolak resists. *Journal of Imaging Science and Technology*, 42(1):15–22, 1998.

[81] H. S. Lee, J. S. Wi, S. W. Nam, H. M. Kim, and K. B. Kim. *Journal of Vacuum Science & Technology B*, to be published 2009.

[82] T. M. Bloomstein, P. W. Juodawlkis, R. B. Swint, S. G. Cann, S. J. Deneault, N. N. Efremow, D. E. Hardy, M. F. Marchant, A. Napoleone, D. C. Oakley, and M. Rothschild. Direct patterning of spin-on glass with 157 nm lithography: Application to nanoscale crystal growth. *Journal of Vacuum Science & Technology B*, 23(6):2617–2623, 2005.

[83] G. M. Schmid, L. E. Carpenter, and J. A. Liddle. Nonaqueous development of silsesquioxane electron beam resist. *Journal of Vacuum Science & Technology B*, 22(6):3497–3502, 2004.

[84] G. M. Schmid, S. D. Burns, P. C. Tsiartas, and C. G. Willson. Electrostatic effects during dissolution of positive tone photoresists. *Journal of Vacuum Science & Technology B*, 20(6):2913–2919, 2002.

[85] S. D. Burns, G. M. Schmid, P. C. Tsiartas, C. G. Willson, and L. Flanagin. Advancements to the critical ionization dissolution model. *Journal of Vacuum Science & Technology B*, 20(2):537–543, 2002.

[86] W. Wu, W. M. Tong, J. Bartman, Y. F. Chen, R. Walmsley, Z. N. Yu, Q. F. Xia, I. Park, C. Picciotto, J. Gao, S. Y. Wang, D. Morecroft, J. Yang, K. K. Berggren, and R. S. Williams. Sub-10 nm nanoimprint lithography by wafer bowing. *Nano Letters*, 8(11):3865–3869, 2008.

[87] I. Bita, J. K. W. Yang, Y. S. Jung, C. A. Ross, E. L. Thomas, and K. K. Berggren. Graphoepitaxy of self-assembled block copolymers on two-dimensional periodic patterned templates. *Science*, 321(5891):939–943, 2008.

[88] F. S. Bates and G. H. Fredrickson. Block copolymer thermodynamics - theory and experiment. *Annual Review of Physical Chemistry*, 41:525–557, 1990.

[89] S. B. Darling. Directing the self-assembly of block copolymers. *Progress in Polymer Science*, 32(10):1152–1204, 2007.

[90] C. T. Black, R. Ruiz, G. Breyta, J. Y. Cheng, M. E. Colburn, K. W. Guarini, H. C. Kim, and Y. Zhang. Polymer self assembly in semiconductor microelectronics. *IBM Journal of Research and Development*, 51(5):605–633, 2007.

[91] C. D. Bain, E. B. Troughton, Y. T. Tao, J. Evall, G. M. Whitesides, and R. G. Nuzzo. Formation of monolayer films by the spontaneous assembly of organic thiols from solution onto gold. *Journal of the American Chemical Society*, 111(1):321–335, 1989.

[92] B. O. Dabbousi, C. B. Murray, M. F. Rubner, and M. G. Bawendi. Langmuir-blodgett manipulation of size-selected cdse nanocrystallites. *Chemistry of Materials*, 6(2):216–219, 1994.

[93] Y. Xia Y. Yin. Self-assembly of monodispersed spherical colloids into complex aggregates with well-defined sizes, shapes, and structures. *Advanced Materials*, 13(4):267–271, 2001.

[94] M. J. Fasolka and A. M. Mayes. Block copolymer thin films: Physics and applications. *Annual Review of Materials Research*, 31:323–355, 2001.

[95] P. Mansky, P. Chaikin, and E. L. Thomas. Monolayer films of diblock copolymer microdomains for nanolithographic applications. *Journal of Materials Science*, 30(8):1987–1992, 1995.

[96] M. Park, C. Harrison, P. M. Chaikin, R. A. Register, and D. H. Adamson. Block copolymer lithography: Periodic arrays of similar to 10(11) holes in 1 square centimeter. *Science*, 276(5317):1401–1404, 1997.

[97] R. G. H. Lammertink, M. A. Hempenius, J. E. van den Enk, V. Z. H. Chan, E. L. Thomas, and G. J. Vancso. Nanostructured thin films of organic-organometallic block copolymers: One-step lithography with poly(ferrocenylsilanes) by reactive ion etching. *Advanced Materials*, 12(2):98–103, 2000.

[98] T. Thurn-Albrecht, J. Schotter, C. A. Kastle, N. Emley, T. Shibauchi, L. Krusin-Elbaum, K. Guarini, C. T. Black, M. T. Tuominen, and T. P. Russell. Ultrahigh-density nanowire arrays grown in self-assembled diblock copolymer templates. *Science*, 290(5499):2126–2129, 2000.

[99] Y. S. Jung and C. A. Ross. Orientation-controlled self-assembled nanolithography using a polystyrene-polydimethylsiloxane block copolymer. *Nano Letters*, 7(7):2046–2050, 2007.

[100] C. Park, J. Yoon, and E. L. Thomas. Enabling nanotechnology with self assembled block copolymer patterns (vol 44, pg 6725, 2003). *Polymer*, 44(25):7779–7779, 2003.

[101] R. A. Segalman. Patterning with block copolymer thin films. *Materials Science & Engineering R-Reports*, 48(6):191–226, 2005.

[102] J. Y. Cheng, C. A. Ross, E. L. Thomas, H. I. Smith, and G. J. Vancso. Fabrication of nanostructures with long-range order using block copolymer lithography. *Applied Physics Letters*, 81(19):3657–3659, 2002.

[103] J. Y. Cheng, A. M. Mayes, and C. A. Ross. Nanostructure engineering by templated self-assembly of block copolymers. *Nature Materials*, 3(11):823–828, 2004.

[104] L. Rockford, Y. Liu, P. Mansky, T. P. Russell, M. Yoon, and S. G. J. Mochrie. Polymers on nanoperiodic, heterogeneous surfaces. *Physical Review Letters*, 82(12):2602–2605, 1999.

[105] E. W. Edwards, M. F. Montague, H. H. Solak, C. J. Hawker, and P. F. Nealey. Precise control over molecular dimensions of block-copolymer domains using the interfacial energy of chemically nanopatterned substrates. *Advanced Materials*, 16(15):1315, 2004.

[106] J. Y. Cheng, C. T. Rettner, D. P. Sanders, H. C. Kim, and W. D. Hinsberg. Dense self-assembly on sparse chemical patterns: Rectifying and multiplying lithographic patterns using block copolymers. *Advanced Materials*, 20(16):3155–3158, 2008.

[107] R. Ruiz, H. M. Kang, F. A. Detcheverry, E. Dobisz, D. S. Kercher, T. R. Albrecht, J. J. de Pablo, and P. F. Nealey. Density multiplication and improved lithography by directed block copolymer assembly. *Science*, 321(5891):936–939, 2008.

[108] D. Sundrani, S. B. Darling, and S. J. Sibener. Hierarchical assembly and compliance of aligned nanoscale polymer cylinders in confinement. *Langmuir*, 20(12):5091–5099, 2004.

[109] C. T. Black. Self-aligned self assembly of multi-nanowire silicon field effect transistors. *Applied Physics Letters*, 87(16):163116–3, 2005.

[110] P. J. Flory and W. R. Krigbaum. Thermodynamics of high polymer solutions. *Annual Review of Physical Chemistry*, 2(1):383–402, 1941.

[111] Maurice L. Huggins. Solutions of long chain compounds. *The Journal of Chemical Physics*, 9(5):440, 1941.

[112] G. J. Kellogg, D. G. Walton, A. M. Mayes, P. Lambooy, T. P. Russell, P. D. Gallagher, and S. K. Satija. Observed surface energy effects in confined diblock copolymers. *Physical Review Letters*, 76(14):2503–2506, 1996.

[113] D. J. Kinning and E. L. Thomas. Hard-sphere interactions between spherical domains in diblock copolymers. *Macromolecules*, 17(9):1712–1718, 1984.

[114] Y. S. Jung, W. Jung, and C. A. Ross. Nanofabricated concentric ring structures by templated self-assembly of a diblock copolymer. *Nano Letters*, 8(9):2975–2981, 2008.

[115] E. Helfand. Block copolymers, polymer-polymer interfaces, and theory of inhomogeneous polymers. *Accounts of Chemical Research*, 8(9):295–299, 1975.

[116] R. Matsuno, H. Otsuka, and A. Takahara. Polystyrene-grafted titanium oxide nanoparticles prepared through surface-initiated nitroxide-mediated radical polymerization and their application to polymer hybrid thin films. *Soft Matter*, 2(5):415–421, 2006.

[117] T. J. Senden, J. M. di Meglio, and P. Auroy. Anomalous adhesion in adsorbed polymer layers. *European Physical Journal B*, 3(2):211–216, 1998.

[118] E. J. Kramer. Condensed-matter physics - melted by mistakes. *Nature*, 437(7060):824–825, 2005.

[119] Joel K. W. Yang, Andrew J. Kerman, Eric A. Dauler, Cord Bryan, Vikas Anant, Richard J. Molnar, and K. Berggren Karl. Suppressed critical current in superconducting nanowire single-photon detectors with high fill-factors. *IEEE Transactions on Applied Superconductivity*, submitted 2008.

[120] P. Hashemi, M. Canonico, J.K.W. Yang, L. Gomez, K.K. Berggren, and J. L. Hoyt. Fabrication and characterization of suspended uniaxial tensile strained-si nanowires for gate-all-around n-mosfets. *ECS (Electrochemical Society) Transactions*, 16(10):57–68, 2008.

[121] M. D. Austin, H. X. Ge, W. Wu, M. T. Li, Z. N. Yu, D. Wasserman, S. A. Lyon, and S. Y. Chou. Fabrication of 5 nm linewidth and 14 nm pitch features by nanoimprint lithography. *Applied Physics Letters*, 84(26):5299–5301, 2004.

[122] M. D. Austin, W. Zhang, H. X. Ge, D. Wasserman, S. A. Lyon, and S. Y. Chou. 6 nm half-pitch lines and 0.04 mu m(2) static random access memory patterns by nanoimprint lithography. *Nanotechnology*, 16(8):1058–1061, 2005.

[123] T.P. Orlando and K.A. Delin. *Foundations of Applied Superconductivity.* Prentice Hall, 1991.